Flow Simulation of the Self-compacting Concrete by the Unresolved CFD-DEM Approach: Bingham Fluid and Multiphase Flow

Swansea University
Prifysgol Abertawe

Sizeng You

College of Engineering
Swansea University

Submitted to Swansea University in fulfilment of the requirements for the Degree of
Doctor of Philosophy

March 2022

To my beloved family, girlfriend and all friends…

Abstract

The self-compacting concrete (SCC) is a material that has great flowability in fresh but sustains a high bearing capacity in the hardened state. It is widely used in projects where manual compaction is inconvenient such as high-rise buildings, deep foundations, and highly reinforced structures. However, contrary to its rapid growth in popularity, the study on the flow behaviour of fresh SCC is limited. Consequently, controlling the common defects in practices such as segregation, bleeding, and exclusion of rebars remains a great challenge. To provide a numerical technique for this problem, this thesis aims to establish a framework for the SCC flow simulation.

Preliminarily, the fresh concrete is regarded as a homogeneous Bingham fluid and the software Fluent is used to investigate the flow behaviour of fresh SCC. Firstly, a parametric study is designed to correlate the performance of robust workability tests and the two-parameter Bingham model. It provides a convenient indirect method to obtain concrete rheology for numerical modeling. At the same time, it fills up the gap caused by the lack of reliable and consistent direct solutions. To demonstrate its the performance, a case of diaphragm wall is chosen as an example to show its application in real practice. According to the on-site test record, commercial concrete transported by different trucks varies greatly in the rheology. The simulation of construction process is configured referring to the on-site placement arrangement. Meanwhile, to show a comparison, the same construction process is repeated but uses only one type of concrete. This case study not only shows the distribution of concretes in the diaphragm wall but also indicates the influence of material homogeneity on concrete distribution.

In practice, the size of coarse aggregate in concrete is usually close to the rebar. To study the interaction between fresh SCC and the reinforcement, the existence of aggregate cannot be ignored. The unresolved CFD-DEM approach is a powerful two-way coupled technique to study the particulate flow, which solves the fluid flow by the CFD, tracks the particle trajectory by the DEM, and couples the two by exchanging momentum. In the further study, the goal is to develop our in-house code based on this approach to realize the SCC flow simulation at the scale of aggregate size. On the initial step, an in-house code is developed for the basic CFD-DEM scenario: the coupling of a single Newtonian fluid and a discrete phase. Every part of our in-house including CFD solver, DEM solver and their coupling is validated by comparing with sophisticated software like *OpenFOAM*, *LIGGGHTS* and *CFDEM*. In the next step, the difficulties to accomplish the simulation of SCC flow are to be discussed: a general VOF-DEM method and acceptable computation cost.

The complexity of SCC flow simulation lies in 3 aspects: 3 phases are involved including air, mortar, and aggregate; the geometry of flow domain could be very complicated; the comparable size of aggregate, rebar, and CFD cell. To overcome the first difficulty, the VOF method is implemented to solve the multiphase flow in the CFD domain which gives the so-called VOF-DEM method. While the latter two facts bring the challenge to the mapping between CFD and DEM domains. What's more, the discontinuity nature of the interface between two fluids worsens the situation. Improper mapping methods will generate unsmooth CFD fields in the coupling stage and lead to numerical instability. To address this issue, the mapping of involved variables is grouped and different schemes are proposed for them.

For example, the volume fraction is a variable in the space domain which is uniform in all directions. An improved *statistic kernel* method is developed to obtain a smooth volume fraction field because it could handle a wide range of cell/particle size ratio. Besides, the mapping of fluid velocity, drag force, torque, and so on are discussed. The performance of the VOF-DEM method with the general coupling scheme is demonstrated by 3 cases: a group of small particles fall into water from the air, a big particle falls into the water from the air and a big particle rotates on the interface.

Due to the exchange of drag force between CFD and DEM, one extra time step criterion is introduced to each of the CFD and DEM solvers. In the case of concrete material, it becomes the bottleneck of computation efficiency. For Bingham fluid, when the shear rate is small, the fluid will show an extremely high apparent viscosity which results in a very small critical time step. In the case of fresh mortar, it can be as small as $1 \times 10^{-7}\ s$ for both CFD and DEM, which makes the computation very expensive. To solve this problem, a relaxing scheme is proposed to release the drag-induced step criteria. It gives explicit time-step-independent solutions for drag force computing in both CFD and DEM solvers. The performance of each solution and their combination are validated step by step. The result proves that the relaxing scheme could release the drag-induced time step without sacrificing accuracy. At last, a case of SCC flow shows that it increases the CFD time step by 100 times which is dominant in simulation.

Once the above two major challenges are settled, our in-house code was used to simulate the workability tests. According to the previously obtained relation chart between the indices of workability tests and Bingham parameters, the apparent properties of the mortar and aggregate mixture were obtained from the simulation results of the slump flow test and V funnel test. What's more, using the L box test, the influence of aggregate gradation, the existence of rebars and aggregate were discussed one by one.

As a conclusion, we have proposed a feasible numerical technique to simulate the fresh SCC flow: to study the feature of bulk flow, the concrete can be modelled by pure CFD; to study it at the scale of aggregate size, the proposed VOF-DEM method and the relaxing scheme should be used to enable the desired simulation with acceptable efficiency.

Declarations

This work has not previously been accepted in substance for any degree and is not being concurrently submitted in candidature for any degree.

Signed............... [redacted] ....

Date... 30/02/2022

This thesis is the result of my own investigations, except where otherwise stated. Other sources are acknowledged by footnotes giving explicit references. A bibliography is appended.

Signed................ [redacted] ....

Date... 30/02/2022

I hereby give consent for my thesis, if accepted, to be available for photocopying and for inter-library loan, and for the title and summary to be made available to outside organisations.

Signed............ [redacted] ....

Date... 30/02/2022

The University's ethical procedures have been followed and, where appropriate, that ethical approval has been granted.

Signed................ [redacted] ....

Date... 30/02/2022

Table of contents

Acknowledgements

In the marathon of PhD study, I have received support and help from many people, without which I would not have the opportunity to accomplish this thesis. First and foremost, I would like to express my sincere appreciation to my supervisor Prof. Chenfeng Li, for his systematic guidance, support and inspiration at all the stages of my PhD. Every time I was trapped, he was open to providing technical suggestions and inspiring ideas. His dedication to the research is also my spiritual strength to challenge the various difficulties in the long run. In addition, there are sincere thanks to his emotional caring and encouragement in my tough times.

In the past years, I was working with a group of great colleagues whose experience is precious to me. Many thanks to the Shaoqing Cui, Bin Chen, Beatriz Ramos Barboza, Muhannad Adolsary, Muhammad Zakaria, Jinlong Fu, Ashutosh Bhokare, Matthew Hall, Conleth Unaeze, Yanan Sun, Bingbing Chen, Kazuya Yamamoto, Shan Zhong, Shuai Shu, Xiangyun Ge, Tom Mitchell, Megan Wiggins. Specially thanks are given to Ashtosh Bhokare for the inspiring cooperation. In addition, I also met many friends in Zienkiewicz Centre for Computational Engineering (ZCCE). Thanks to them all for the memorable time we had together.

I would like to thank Swansea University and the ZCCE for offering the PhD scholarship for my tuition fee and providing a great environment and facilities for my learning and research. At the same time, I'm grateful for the three-year consistent financial support from the China Scholarship Council (CSC) without which I would not have the chance to study at Swansea University.

I would like to thank my family for their support, encouragement and accompany with which I could focus on my work. At last, the special appreciation is for my girlfriend. Although we are apart physically in pursuing our PhD, we have been accompanying each other all the long way and she is always my strong support.

List of figures

List of tables

Chapter 1

Introduction

1.1 Background and motivation

Concrete is a mixture of 5 components: cement, aggregate, water, additions and chemical admixtures. With a proper design, concrete showing unique features have been invented to meet specific requirements in different fields. For example, self-compacting concrete (SCC) was developed to obtain better workability in its fresh state without weakening the hardened concrete strength. Adding a small amount of admixture, the SCC can flow under its weight without any extra compaction. As the water/cement ratio is unchanged, the concrete strength will not be affected. It can be seen that the SCC has great advantages in projects where manual compaction is barely available. Hence, since its invention in the 1980s in Japan, SCC has been gaining popularity rapidly worldwide. Meanwhile, as reported by the EFFC/DFI guide[87], various imperfections were observed frequently in the deep foundation applications such as the grooves on the pile surface, the inclusion of rebar cage, the bleed channels and mattressing on the surface (as listed in Fig. 1.1). If their extent and appearing frequency are limited, they are thought to be acceptable. Otherwise, they will be called defects which would threaten the bearing capacity and durability so that extra maintenance is necessary. The EFFC/DFI guide analyzes the possible sources of these imperfections. However, since the mechanism of fresh concrete flow is unclear, it's still a challenging task to control the occurrences of defects.

This thesis aims to provide a framework of numerical techniques to study the flow behaviour of fresh SCC. Compared with the experimental approach, the numerical method costs less but outputs much faster with full details, which is a great assistant to the practice. However, to achieve our goal, there are two key questions to be answered: what is the rheology of SCC and how to choose the right numerical approach to use. They will be the focus of the following literature review.

(a) Groove (b) Mattressing

(c) Exclusion of rebar cage (d) Bleed channel

Fig. 1.1 Imperfections of deep foundations[87]

1.2 Challenges in SCC flow simulation

For better understanding, cement-based materials such as cement paste, mortar and concrete will be covered in the literature review. The first part is about the research of material rheology while the second details the numerical study on concrete flow. Based on this review, two core challenges in realizing the fresh concrete flow are summarized.

1.2.1 Rheology of SCC

For the cement-based mixture [16, 9, 20], the Bingham fluid model, which contains two parameters plastic viscosity μ and yield stress τ_0 as shown in Figure 1.2, is the most widely used constitutive model. A Bingham fluid can retain its shape if the shear stress is below the yield stress τ_0. When the shear stress is above τ_0, the fluid will begin to flow, and the shear rate is linearly proportional to the exceeded value of shear stress. Despite the simplicity of the Bingham model, it is not trivial to measure the viscosity and yield stress in construction practice. Using analytical, experimental and numerical approaches, researchers have tried different ways to obtain these two rheological parameters for practical concrete mixes, but up to now, it remains an outstanding challenge.

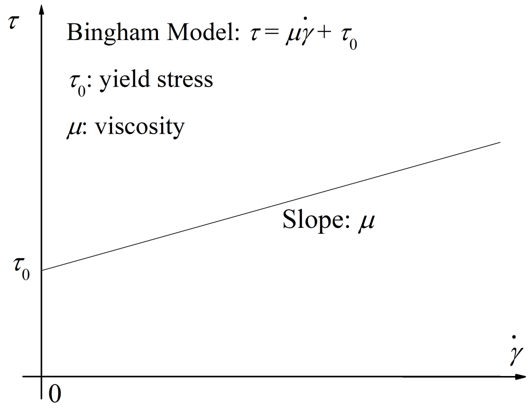

Fig. 1.2 The Bingham fluid model

In the construction industry, the fluidity of fresh concrete is typically evaluated through workability tests, which are easy to perform and well documented in industrial guides, e.g. [39]. The most widely used workability tests include the slump flow test, the V-funnel test and the L-box test etc., each of which is designed to evaluate a specific aspect of fresh concrete. But, these tests can only provide qualitative measures to the rheological behaviour of concrete, and cannot detect such physical properties as viscosity and yield stress. It is generally believed that a close correlation between the workability tests and the concrete rheology exists, but the quantitative relation is yet to be discovered.

Many different rheometers have also been developed in order to directly measure the rheological properties of concrete mix, including BML viscometer [85], BTRHEOM [22], RSNS rheometer [56] and ICAR rheometer [49] etc., to name a few. But the adoption of rheometers in construction practice has been much limited due to several major disadvantages [12, 9, 36]: 1) the readings from different rheometers vary hugely, making it difficult to reach an agreement; 2) the rheometers are expensive and inconvenient to use in construction sites.

Quality control of concrete placement during construction work requires simple and reliable tests to ensure the right concrete is placed through the right process. The workability tests provide the most common monitoring approaches for the construction industry. It is recognized that the slump flow has a close relationship with the yield stress of concrete mix [62, 18, 30], and there have been many attempts to quantify this relation. [50] first established a relation between the yield stress and the spread diameter of slump flow test:

$$\tau_0 = \frac{225\rho g V_c^2}{4\pi^2 D_f^5} \tag{1.1}$$

where D_f denotes the concrete spread diameter of the slump flow test, ρ the concrete density, g the gravity, and V_c the total volume of slump cone. Eqn. (1.1) takes the total volume of concrete into consideration but neglecting the influence of viscosity. [75] summarized the flow behaviour of the slump flow test into three regimes: the pure shear flow (large flow diameter) regime, the pure elongational flow (low slump height) regime, and the intermediate regime. They proposed empirical solutions for each regime, and the solution for the pure shear flow regime remains the same as [50]. Later, [77] improved the estimation in Eqn. (1.1) by incorporating the influence of surface tension effects:

$$\tau_0 = \frac{D_f^2}{4V_c}\left(\frac{225\rho g V_c^3}{\pi^2 D_f^7} - \lambda\right) \tag{1.2}$$

where λ is a coefficient representing the influence of surface tension and contact angle. Besides the concrete spread diameter D_f, the total flow time when the concrete spread reaches the final diameter and the time when it reaches 500 mm (T_{500}) have also been evaluated. [90] proposed a simple linear relation between the total flow time and the ratio of viscosity to yield stress. Later, based on experimental tests, [36] presented an empirical equation for this relationship. Also through experiments, [34] studied the relationship between T_{500} and rheological properties, and suggested that T_{500} is sensitive to both yield stress and viscosity. A similar conclusion was also presented by [64].

For the Marsh cone test of cement paste, [76] proposed an equation linking the flow time with the yield stress, the viscosity and the Marsh cone geometry. It was suggested that viscosity and yield stress could be solved directly if flow times were measured for Marsh cones of two different shapes. This analysis assumes the flow rate at the nozzle remains constant and the free surface of cement paste is always level in the cone. Later, [65] improved the flow rate evaluation of [76] by considering the Reynolds number in the nozzle and applying Herschel-Bulkley model in place of Bingham model. The improvement was validated by comparisons with experiment and numerical simulation. But, when applying this solution to the V-funnel test, the assumptions of level surface and constant flow rate are both questionable [53].

Besides these analytical models derived from workability tests, the viscosity of concrete mix was also studied by treating it as a homogeneous particle-fluid suspension. [35] predicted the viscosity for multimodal suspensions from unimodal viscosity data. The viscosity of a unimodal suspension was represented as

$$\mu = \mu_0 H(\phi) \tag{1.3}$$

where μ_0 denotes the viscosity of fluid, ϕ the volume concentration of particles and $H(\phi)$ the stiffening coefficient. It was further assumed that smaller particles in a bimodal suspension behave like a fluid medium surrounding larger particles if the size ratio (small to large) is below 0.1. Extending this assumption to multimodal suspensions, the overall viscosity was estimated as

$$\mu = \mu_0 \prod_{i=1}^{n} H(\phi_i) \tag{1.4}$$

where i is the index of particle classes, n the total number of particle classes, ϕ_i the volume concentration of particle class i, and $H(\phi_i)$ the stiffening coefficient of particle class i. Considering size and shape variations in different particle classes, [63] proposed different $H(\phi_i)$ for different classes. [43] modified ϕ_i in Eqn. (1.4) as ϕ_i/α_i, where α_i is the maximum volume concentration of particle class i. Later, [37] proposed a semi-empirical equation with the same pattern for yield stress prediction.

The aforementioned research works are mainly based on analytical or experimental studies. Recently, with the rapid growth of computing power, numerical simulation also became an effective tool for the study of concrete rheology. By simulating the mini-conical slump flow test, [9] found that the viscosity's influence on the spread diameter cannot be neglected when the yield stress is small. Moreover, the following equation was proposed as an improvement to Eqn. (1.2):

$$\frac{D_f}{D_f^{ref}} = 1 - 0.13 \ln\left(\frac{\mu_{equ}}{\mu_0}\right) \tag{1.5}$$

where μ_{equ} is the equivalent viscosity and D_f^{ref} the reference spread diameter. Later, using a remeshing finite element strategy, [23] simulated the mini-cone slump flow test and EN445 cone test. They found the discharge time was closely related to the ratio of viscosity to yield stress. By assuming the viscosity from the concentrated suspension theory, [4] estimated the yield stress by matching the Smoothed-Particle Hydrodynamic (SPH) simulation result of slump flow test with measured experimental data. Using the SPH method, [53] conducted 2D simulation for the V-funnel test to study the discharge time.

Despite the various research works summarized above, no general agreement has been reached on how to determine viscosity and yield stress for fresh concrete. The analytical approaches are based on various assumptions and simplifications, limiting their applicability to specific conditions. Moreover, the analytic predictions provide only rough approximations to the concrete rheology, and not suitable for accurate quantification. The experimental approaches using dedicated rheometers are not only costly, but they also lack the necessary consistency and repeatability for practical use. There have been some interesting numerical works, but they are mainly feasibility studies focusing on modelling methodology instead of the quantification of concrete rheology. To address this outstanding issue, we systematically investigate in a quantified manner the relationship between commonly adopted workability tests and the rheological parameters of fresh concrete. Numerical simulations are conducted for various concrete mixes covering the full spectrum of concrete rheology, and the simulation results form a comprehensive database to infer rheological parameters. The finding from this study enables concrete rheology to be accurately determined from the routinely performed workability tests without any additional effort.

1.2.2 Numerical methods

The research work on the flow simulation of fresh concrete is rare compared with other topics in the concrete area. So, in this chapter, the cement-based materials are all covered including concrete, mortar, cement paste, etc. On different conditions, the cement-based materials can be treated as either continuous or discontinuous materials. For example, some researchers treat the cement mixture as discrete material, which actually assumes that the flow behavior is dominated by the coarse aggregate. While, for the mixture with high mobility or for the simulation of a large volume flow, the material will be assumed as homogeneous Bingham fluid. Covering a wide range of literature, 5 well established numerical techniques are found: Discrete Element Method (DEM), the Finite Volume Method (FVM), Finite Difference Method (FDM), Finite Element Method (FEM), Smoothed-Particle Hydrodynamics (SPH). These methods are used by researchers for specific purposes which will be detailed in the following.

The DEM is also known as the Distinct Element Method. This method was first proposed to model the motion of granular material by Cundall and Strack [21]. Particles are modeled individually, and their motion is governed by Newton's Law. The contact between particles can be given by different predetermined constitutive models. In each time step, the contacting relationship will be updated and then the new particle state will be computed accordingly. In the simulation of concrete, the material is discretized into particles and the partition is based on the coarse aggregate. The nature of Bingham fluid is implemented by defining the various contact models. Puri and Uomoto [70, 71] proposed a two-phase model to simulate the slump test of shotcrete and its flow performance in a pressured silo. The fluid phase mortar is treated as a soft layer of the coarse aggregate. A similar concept was applied by many other researchers [61, 82, 40, 74, 32, 105]: calibrate the DEM parameters, use non-spherical particles or model the coupled flow with steel fibers. Most of the work was validated by the slump or slump flow test. Wei Cui etc. [20] proposed a more complex system, where the polyhedron aggregate was used and mortar was modeled by small spheres. Slump flow test and L box test were used for validation.

The FVM, FDM and FEM are all mesh-based methods, which are developed for continuous material. They all discretize the space domain into a certain of finite sub-domains and assume different field approximations in every single sub-domain. Besides, they also discretize the Navier-Stokes equations differently. In the FVM, the volume integrals are converted into surface integrals. The FEM uses a polynomial approximation for the fluid field in the sub-domains. For FDM, the derivatives are approximated by the Taylor series. Among them, the FVM is the most popular method in terms of commercial CFD software. Using the FVM-based software Fluent, V.H. Nguyen etc. [65] evaluated the influence of Bingham parameters on cement paste flow by simulating the Marsh cone test. S. Tichko etc. [89] simulated the concrete filling process of real size formworks and compared it with the experiment result. K. Vasilic [95] proposed a porous medium analogy to revolve the influence of reinforcement and Fluent was used to carry out the validation work. H. D. Le etc. [54] presented the simulation of MK-II type rheometer to approve a better way to obtain concrete rheological properties. Many researchers also used the FDM-based software Flow-3D to model the concrete flow. For example, M. Hosseinpoor and his group [42, 41] used this software to simulate the L box test and the GMO method was applied to model the coarse aggregate. Using this technique, the influence of rheological properties, reinforcing rebars and aggregate content was discussed. But, the GMO method is limited to 500 objects. This software was also used by N. Roussel and his group [23, 75] to study the concrete flow in slump flow test and slipform machine. Due to the large deformation in fluid flow, the FEM is less developed compared with the other 2 methods in the CFD field. This difficulty was addressed by either the remeshing technique or the Eulerian FEM approach coupled with the VOF model. In the literature, the former was used to simulate the paste flow in the Marsh cone test, the mini slump flow test [19, 36]. The latter includes many different methods such as Galerkin FEM approach [88], the FEMLIP [31], the DLM/FD method [96]. All the two groups were used for similar purposes with others such as simulation of workability tests, fiber orientation and porous medium analogy of reinforced area.

The SPH is a mesh-free CFD approach, which discretizes the material domain into a finite number of particles associated with mass and other fluid fields. This makes the SPH a Lagrangian method that captures the free surface naturally. What’s more, the aggregate can also be easily modeled. H. Lashkarbolouk etc. [52, 53] used the SPH method to study the proper range of rheological properties of SCC by simulating the L box test and V funnel test. B.L. Karihaloo and his group [4, 25–28, 1, 2] also carried out the various workability tests and studied the distribution of coarse aggregate, the fiber orientation, the blockage due to rebars. Thanh et al. [86] modelled the self-consolidating engineered cementitious composites by the weakly compressible SPH. In the same framework, they realized the modelling of flexible synthetic fibre.

Besides the 5 methods, there are also other methods that were used to simulate the concrete flow such as the DPD method [60], MPS method [103], the LBM [72, 102, 14] method. However, the majority of all the mentioned research work concerned only the simulation of workability tests, and the concrete or paste was treated as either continuous or discrete material.

1.3 Layout of the thesis

The defects in concrete casting have different sources of mechanisms. For example, the blockage of coarse aggregate due to the dense reinforcement can show the defects in the form of filtration and local inclusion; a bad design of aggregate gradation may result in segregation. All the phenomena can be concluded as the inappropriate interaction between fluid, particle, rebar and boundary. Concrete is a mixture of different components. But depending on the scale of observation, there are many different ways to look into it. As shown in Fig.1.3: (1) at a relatively large Scale 0, the concrete can be regarded as pure fluid; (2) at a lower Scale 1 where aggregate is concerned, the concrete is the mixture of mortar and aggregate; (3) while, if the sand in the mortar is the key which comes to the Scale 2, the mortar should be treated as the mixture of paste and sand; (4) at last, if the cement particle is of interest which is the Scale 3, the paste should be considered as a mixture of the cement and water. In the first row of the figure, besides the water, the other 3 are regarded as the fluid phase at their scales. While the constituents in the second row are all particles.

This thesis focuses on the Scale 0 and Scale 1. The former requires a CFD solver, while the latter needs a numerical technique for CFD-DEM modeling. In all numerical methods presented in chapter 1.2.2, the FVM is the most popular because of its maturity, accuracy and computational cost. So, this method is used for CFD cases. As a preliminary study, the FVM-based commercial software Fluent is used for the study on Scale 0 to investigate the flow behaviour of fresh concrete. While, for the Scale 1, the powerful unresolved CFD-DEM approach is coded and developed to realize its application on the SCC flow. Similarly, the FVM is the method for CFD. Meanwhile, the soft-sphere approach of DEM [21] will be used to model the aggregate. It is advantageous in the case involving a large number of collisions with multiple contacts between particles. The details of the study on the two scales will be presented in the following chapters. The layout is given below.

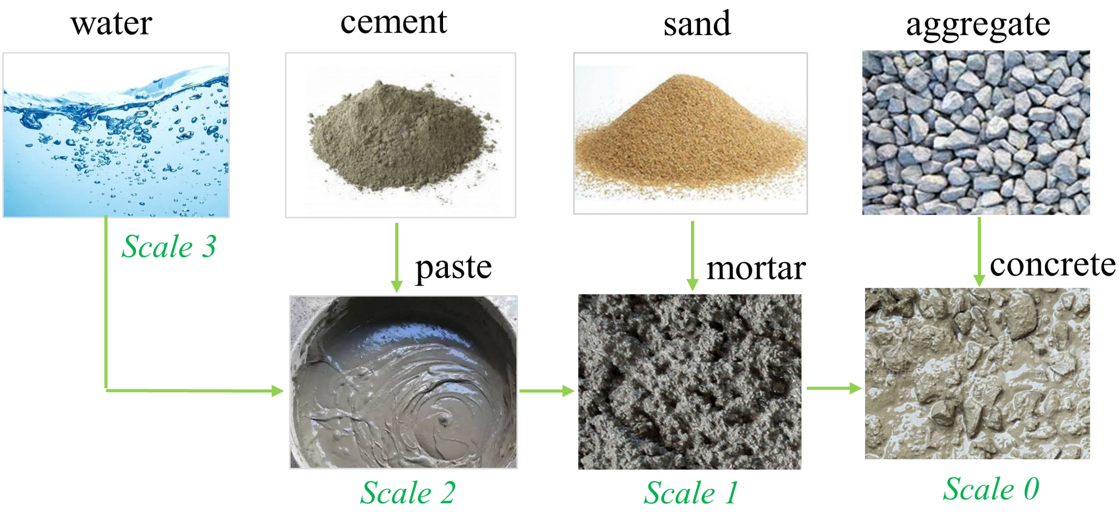

Fig. 1.3 The composition of fresh concrete at different scales

In Chapter 2.1, a systematic parametric study was carried out which tried to correlate the concrete rheological properties with the robust workability tests including slump flow test, V Funnel test, extended cone test and inverted cone test. Then, in the simulation of a diaphragm wall casting, this quantitative relation was used to determine the concrete rheology according to the on-site workability tests. The comparison in this case study showed the influence of inhomogeneity on the flow pattern in the diaphragm wall.

In Chapter 3.1, the formulation of the unresolved CFD-DEM approach will be introduced in detail. In this framework, the fluid flow is governed by the volume-averaged Navier-Stokes Equations and the particle trajectory is modeled by Newton's Law. The coupling between the two is realized by exchanging the analytically computed momentum. Based on a detailed formulation of this approach, we developed an in-house CFD-DEM code. Before any further discussion, all parts of this code were validated by comparing with the sophisticated software including *OpenFOAM*, *LIGGGHTS* or *CFDEM*.

Chapter 4 expatiates the major challenges to applying the unresolved CFD-DEM approach in the SCC flow simulation: a multiphase model and smooth mapping schemes for variables. As an Eulerian approach, the air is also involved in the fluid domain which requires a multiphase model to solve the two-phase flow in the CFD. For this purpose, the VOF model is chosen and introduced in this chapter. However, implementing the VOF method solely is not enough to promise a stable so-called VOF-DEM method. Many other factors could add to the complication in SCC flow simulation, including the severe discontinuity on the interface of air and mortar, the complex geometry and the large range of size ratio of mesh cell to aggregate. In the mapping between CFD and DEM, these factors should be reasonably evaluated to achieve fields as smooth as possible, which is essential for a stable simulation. To this end, the mapping schemes for all exchanged variables were discussed and classified in this chapter. The overall performance of the VOF method and the proposed mapping schemes were demonstrated by 3 cases.

In Chapter 5, it is pointed out that the momentum exchanging between CFD and DEM introduces one extra time step criterion for each solver. In the case of mortar, it can lead to a time step as small as $1 \times 10^{-7}\ s$ for both solvers due to the huge apparent viscosity at a low shear rate, which therefore makes the computation extreme expensive. This chapter took the drag force as an example. The expression of the drag-induced critical time step was derived for each solver and was then verified by the *CFDEM*. After that, to achieve greater efficiency, the relaxing scheme was proposed to enlarge the drag-induced critical time step. It gave analytical solutions for both CFD and DEM in computing the drag force. Each solution would converge to a terminal state as the time went infinite, which meant a large time step will not lead to an inflation in computing drag force. The accuracy of the relaxing scheme was validated step by step in the case study, and an increase of 100 times was achieved for concrete simulation.

Chapter 6 focuses on the simulation of SCC workability tests by our in-house code. Firstly, the slump test and the V funnel test were carried out, and a pair of indices were obtained from them. Referring to the relation chart in Chapter 2, the rheological properties were obtained. After that, the L box test was used to study the influence of different factors on the SCC flow behaviour such as the aggregate gradation, the existence of rebars and aggregate. These cases show that our in-house is eligible to study the concrete at the Scale 1.

The last Chapter 7 is the conclusion of the whole thesis and gives my outlook for further research.

Chapter 2

Homogeneous perspective: rheological properties and flow behaviour

2.1 Introduction

Despite the variety of research work on the fresh concrete rheology introduced in Chapter 1, no general agreement has been reached on how to determine the viscosity and yield stress of the fresh concrete. For the group of analytical solutions, they are based on various assumptions and simplifications which is limited on a general application. Moreover, the analytic predictions provide only rough approximations to the concrete rheology and are not suitable for accurate quantification. The experimental approaches using dedicated rheometers are not only costly but also lack the necessary consistency and repeatability for practical use. There have been some interesting numerical works, but they are mainly feasibility studies focusing on modelling methodology instead of the quantification of concrete rheology. So, in the preliminary study, it is the main focus to address this outstanding issue. By using the software Fluent, a systematical parametric study is carried out to investigate the relationship between the robust workability tests and the rheological parameters of the fresh SCC. Numerical simulations are conducted for various concrete mixes covering the full spectrum of concrete rheology, and the simulation results form a comprehensive database to infer rheological parameters. The finding from this study enables concrete rheology to be accurately determined from the routinely performed workability tests without any additional effort. To demonstrate the advantage, this indirect method is used in a diaphragm wall case to obtain the properties of fresh SCC from all transporting trucks according to the on-site record of the workability tests. The placement arrangement shows that these batches of concrete are placed into the wall through two tremies simultaneously. In the simulation, 9 representative concretes are determined to cover the variation in concrete rheology and a multiphase model is used to model the random placement of the 9 concretes. This setup tracks the distribution of all concrete phases in the wall. Furtherly, to provide a comparison, the same configuration is used to run a parallel case but with 9 identical concretes. The difference between the two cases shows the influence of material homogeneity on the concrete flow.

2.2 Parametric study on workability tests

2.2.1 Workability tests and numerical models

Previous numerical studies on fresh concrete mainly focused on the modelling methodology, i.e. to examine the feasibility of different numerical methods in the simulation of fresh concrete flow. These simulation methods mainly include the Finite Volume Method (FVM) [23, 42], the Finite Element Method (FEM) [36, 15], the Smoothed-Particle Hydrodynamics (SPH) method [53, 1] and the Discrete Element Method (DEM) [20, 32].

Considering the accuracy and stability of simulation, we adopted the FVM approach for the simulation of various workability tests including the slump flow test, the V-funnel test, the modified cone outflow test and the inverted cone outflow test. As shown in Fig. 1.2, the yield stress in the Bingham model increases from 0 to τ_0 while the shear rate $\dot{\gamma}$ remains 0. The jump in yield stress can cause stability issues to numerical simulation, and one way to overcome this problem is to describe the concrete rheology using the more general Herschel-Bulkley model which contains two stages: a linear stage with a high slope of η_0 and a non-linear stage described by a power-law index n. The Bingham model can be seen as a special case of the Herschel-Bulkley model, where the slope of the linear stage is infinity and the power-law index for the non-linear stage is 1. Using the Herschel-Bulkley model with a sufficiently large but finite slope for the linear stage can avoid stability issues in numerical simulation.

Geometry and meshes

The apparatuses of the slump flow, V-funnel, modified cone outflow and inverted cone outflow tests are shown in Fig. 2.1, Fig. 2.2, Fig. 2.3 and Fig. 2.4 respectively, as well as their dimensions. The slump flow test apparatus consists of two parts (Fig. 2.1), including a truncated cone and a square plate. The top diameter, bottom diameter and height of the cone are 100 mm, 200 mm and 300 mm respectively, and the side length of the square plate is 900 mm. The shape of the V-funnel is an extrusion of a V-shape geometry (Fig. 2.2), which is a combination of a rectangle and an isosceles trapezoid. The side lengths of the rectangle are 65 mm and 150 mm respectively. The top and bottom side lengths of the isosceles trapezoid are 65 mm and 490 mm, and its height is 425 mm. The thickness of the V-funnel is 75 mm. The apparatus of the modified cone outflow test (Fig. 2.3) contains two parts: the top part is a cylinder of height 465 mm and diameter 200 mm, and the bottom part is an inverted slump flow cone. The apparatus of the inverted cone outflow test (Fig. 2.4), as its name suggests, is only an inverted slump test cone.

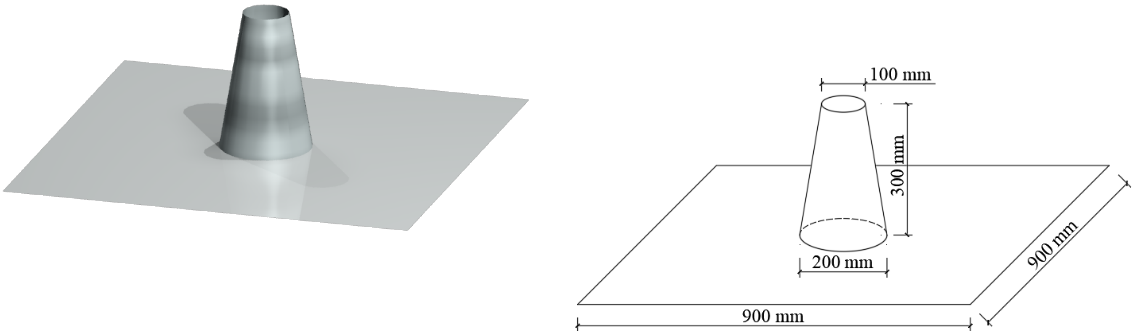

(a) Apparatus (b) Geometry

Fig. 2.1 Slump flow test

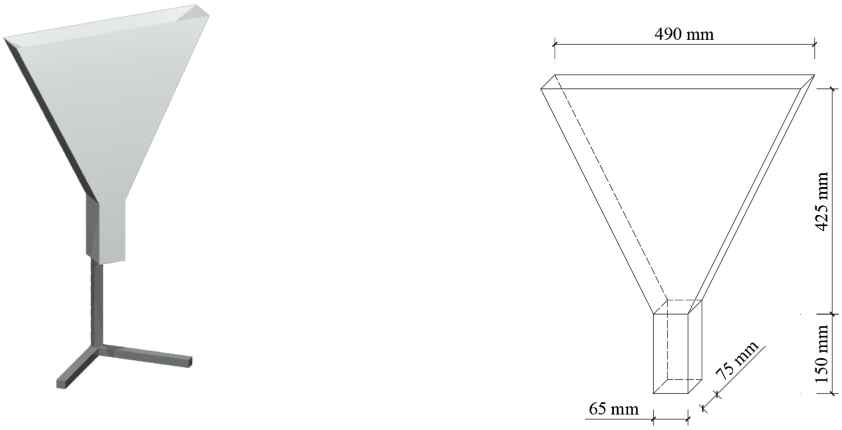

(a) Apparatus (b) Geometry

Fig. 2.2 V-funnel test

The models adopted in numerical simulation are presented in Fig. 2.5, Fig. 2.6, Fig. 2.7 and Fig. 2.8, respectively. The models use fixed FVM meshes, and they cover the full space where the concrete mix may flow during the specific test. The space is occupied by concrete and air, and the Volume of Fluid (VOF) method is employed to capture the interface between them. In order to increase the simulation speed and enhance the stability

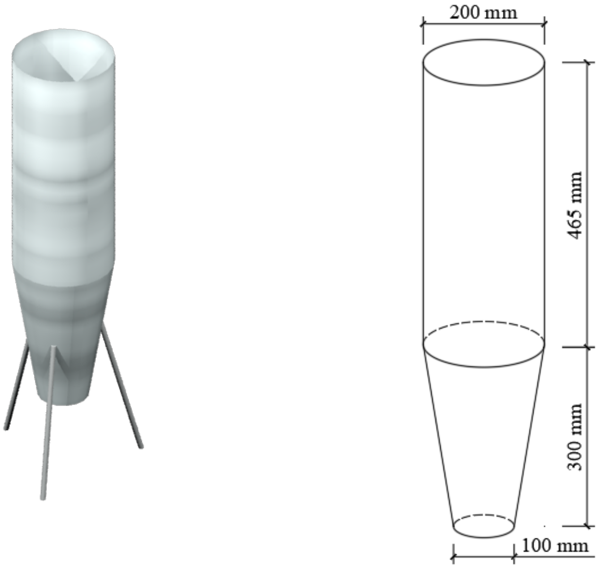

(a) Apparatus (b) Geometry

Fig. 2.3 Modified cone outflow test

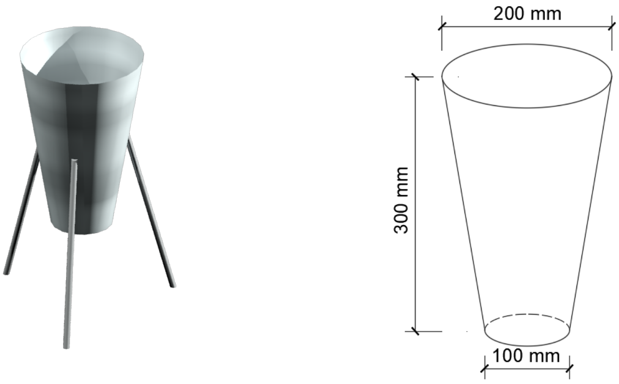

(a) Apparatus (b) Geometry

Fig. 2.4 Inverted cone outflow test

and accuracy, structured meshes are adopted as shown in Fig. 2.5a, Fig. 2.6a, Fig. 2.7a and Fig. 2.8a, where the colours indicate elements at different aspect ratios to meet the mesh quality requirement. The initial distribution of concrete and air in each test are shown in Fig. 2.5b, Fig.2.6b, Fig. 2.7b and Fig. 2.8b, where the blue and green regions represent concrete and air respectively. In reality, air can flow freely in the open space. But for numerical simulation, a finite simulation domain needs to be specified. The sizes of all models have been set sufficiently large such that the closed space would not have any visible impact on the concrete flow.

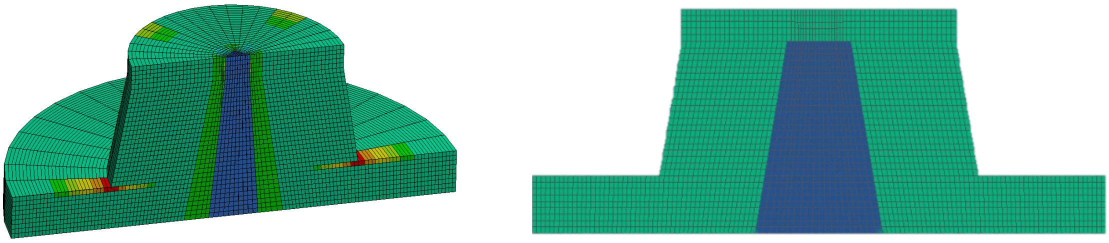

(a) Mesh for slump flow test (b) Initial distribution of concrete (blue) and air (green)

Fig. 2.5 Numerical model of the slump flow test

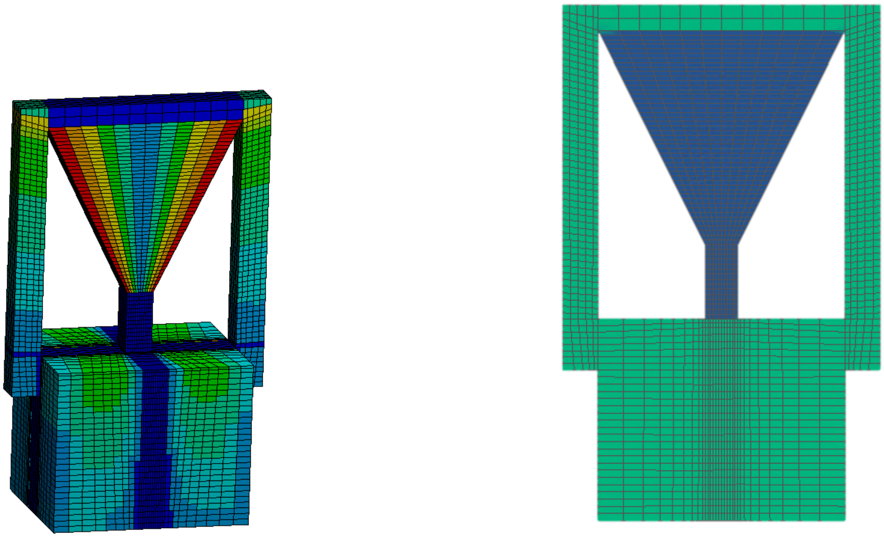

(a) Mesh for V-funnel test (b) Initial distribution of concrete (blue) and air (green)

Fig. 2.6 Numerical model of the V-funnel test

Simulation resolution and convergence check

The spatial and temporal resolution of the numerical simulation must satisfy the convergence requirement to ensure the correct numerical solution is obtained, while the mesh size and time step must also meet the accuracy requirement of the targeted rheological study. For all four workability tests, the accuracy of time-based indices is set as 0.1 s. Depending on the convergence condition, adaptive time stepping is adopted in our simulations, where the maximum time step is set as 0.1 s. In the slump flow test, concrete flow has a high acceleration at the beginning, therefore requiring smaller time steps. In the V-funnel, modified cone outflow and inverted cone outflow tests, the variation of concrete flow over the testing process is much smaller, therefore the time step remains more constant. Besides the time step size, the mesh size must also been chosen carefully to ensure convergence, accuracy and efficiency.

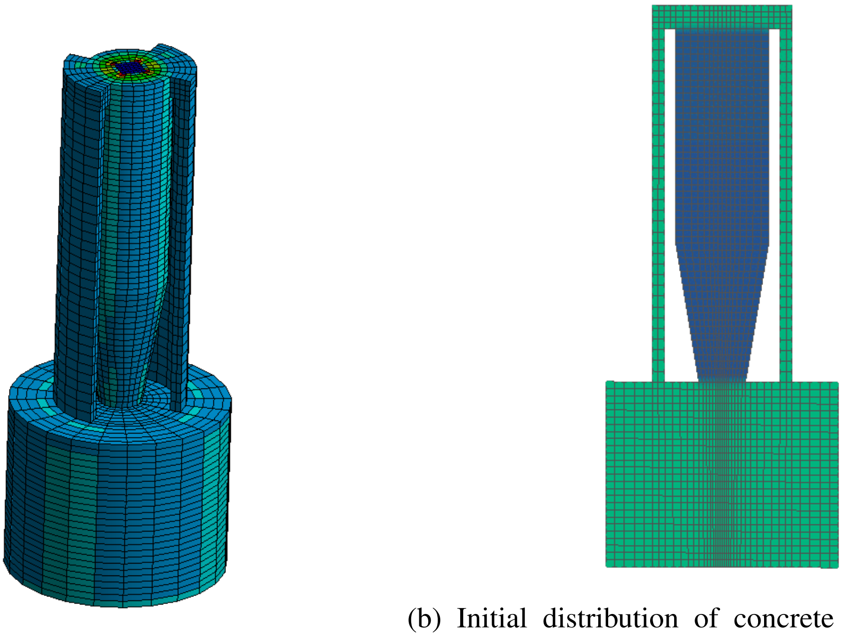

(a) Mesh for modified cone outflow test

(b) Initial distribution of concrete (blue) and air (green)

Fig. 2.7 Numerical model of the modified cone outflow test

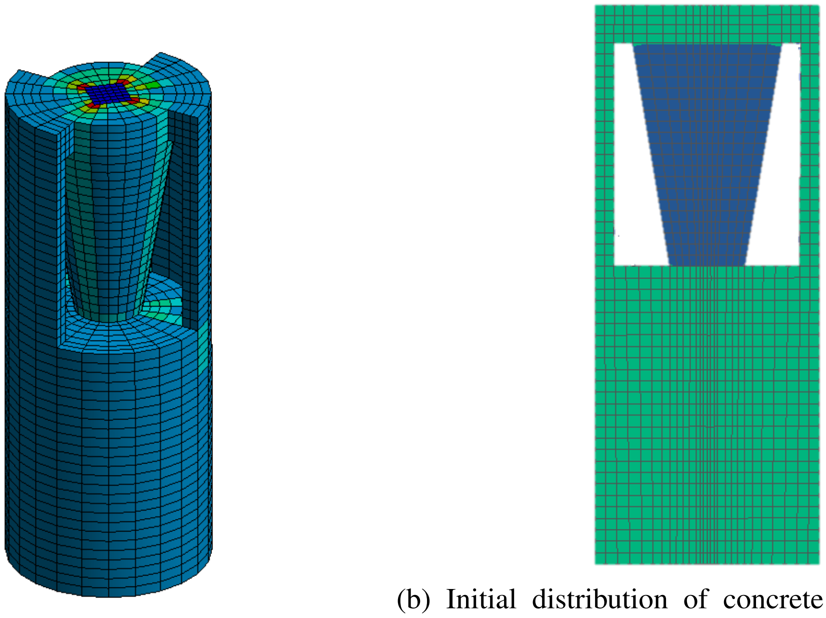

(a) Mesh for modified cone outflow test

(b) Initial distribution of concrete (blue) and air (green)

Fig. 2.8 Numerical model of the modified cone outflow test

An example of the convergence study of the slump flow test is shown in Fig. 2.9a, where three mesh models were compared on a concrete mix with viscosity 50 Pa·s and yield stress 50 Pa. When the element number increases from 49,680 to 103,552, there is significant difference

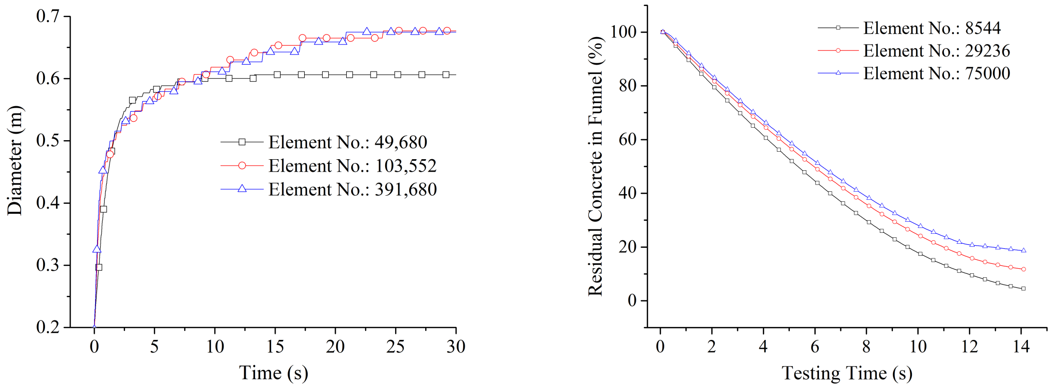

(a) Slump flow test (b) V-funnel test

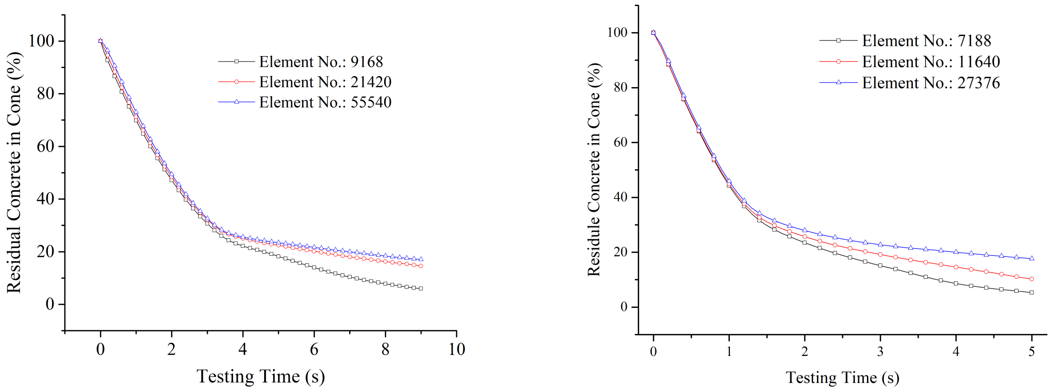

(c) Modified cone outflow test (d) Inverted Cone Outflow Test

Fig. 2.9 Mesh quality validation (viscosity 50 Pa·s, yield stress 50 Pa)

between the two result curves. But when the element number further increases to 391,680, the result only changes slightly. Similar comparisons were also performed on concrete mixes at other rheological ranges. From these convergence studies, the mesh model with 103,552 elements was finally adopted for the simulation of slump flow test. The convergence study was also carried out for the V-funnel, modified cone outflow and inverted cone outflow tests, whose examples are shown in Fig. 2.9b, Fig. 2.9c and Fig. 2.9d respectively. It is noted that for these three outflow tests, the discharge time is the only recorded index. It can be found in Fig. 2.9b, Fig. 2.9c and Fig. 2.9d that the turning points of curves in each figure almost occur at the same time, which implies the discharge time is insensitive to mesh size. The final mesh models chosen for the simulation of V-funnel, modified cone outflow and inverted cone outflow tests contain 29,236, 21,420 and 11,640 elements, respectively.

Indices in workability tests: extraction and classification

The aim of this study is to quantify the relationship between rheological properties of fresh concrete and its workability tests. By adjusting the values of viscosity and yield stress, detailed parametric simulations were performed for all four workability tests described above. Initially, the viscosity was sampled between 10 and 100 Pa·s with an interval of 10 Pa·s, and the yield stress was sampled with 10, 50, 100, 150, 200, 250, 300, 350, 400, 450 and 500 Pa. As shown in Fig. 2.10, a dripping flow pattern was detected in the V-funnel test when the yield stress was greater than 300 Pa, and as a result the discharge time exceeded 70 s. Thus, it is impractical to perform the V-funnel test with the yield stress greater than 300 Pa. As an alternative, the modified cone outflow test and the inverted cone outflow test were introduced to cover the full range of yield stress. Based on the initial result and to provide a finer data set for further analysis, a second batch of simulations were performed for both slump flow and V-funnel tests, by setting the yield stress at 20, 30, 40, 60, 70, 80, 90, 120, 140, 160, 180, 220, 240, 260 and 280 Pa.

Fig. 2.10 Dripping phenomenon

2.2.2 Choose indices: easy to obtain and cover a wide range

Different indices can be extracted from the workability tests. For the slump flow test, the most commonly used indices are the final spread diameter D and the flow time T_{500} (i.e. the

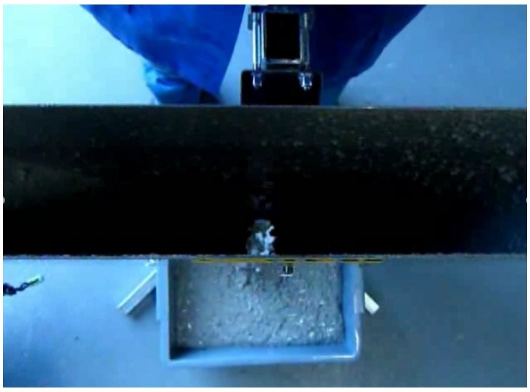

Fig. 2.11 Daylight passing through the nozzle

time taken for the spread diameter to reach 500 mm). Besides these, other indices include the flow time t_D (i.e. the time taken for the spread diameter to reach D), the average flow rate $\bar{v} = D/t_D$ and the maximum increasing rate of spread diameter $v_{\max\_D}$. For the V-funnel, modified cone outflow and inverted cone outflow tests, there are different criteria to determine the discharge time, such as the time when daylight firstly passes through the nozzle t_n, as shown in Fig. 2.11, the time t_m when the majority of concrete flows out of the funnel, and the time t_v when certain amount of concrete flows out of the funnel. Besides these discharge times, the maximum decreasing rate of concrete volume $v_{\max\_t}$ can also be extracted.

The total simulation time for all slump flow tests is set as 30 s. The flow history of a series of slump flow tests is shown in Fig. 2.12, where the yield stress is 10 Pa in Fig. 2.12a, 100 Pa in Fig. 2.12b, and the viscosity increases from 10 to 100 Pa·s. It can be observed that the viscosity affects not only the flow history but also the final spread diameter. The indices D and T_{500} can be extracted directly according to their definitions. The determination of t_D can be referred to [90], which suggested to record the time when the diameter increasing rate decreases to 0.6 mm/s (0.3 mm/s for the radius increasing rate). This criterion is guided by the fact that 0.3 mm is the minimum distance human eye can recognize. Then, $\bar{v}$ can be readily computed from D and t_D. But to determine $v_{\max\_D}$, the diameter increasing rate needs to be calculated for every time step until the maximum value $v_{\max\_D}$ is reached.

The above five indices are not always available depending on the specific cases. First, when yield stress is around 10 Pa, the diameter increasing rate will still be remarkable at the time 30 s. In this situation, the diameter at 30 s is recorded to represent the final diameter, but t_D is no longer available. Secondly, when yield stress and viscosity are both small, the spread diameter D can exceed the boundary of plate. For these cases, D is recorded as 0.9 m. Thirdly, when yield stress increases to around 100 Pa, the spread diameter D will decrease to

500 mm. Thus, the maximum yield stress allowing the extraction of T_{500} is about 100 Pa. Finally, the only universal index is $v_{\max\_D}$, but it is hard to measure in practical tests.

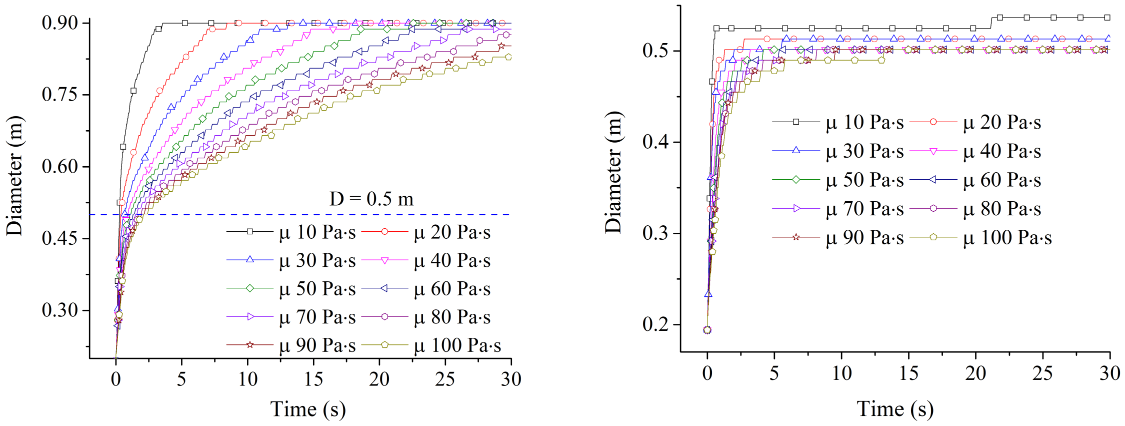

(a) Yield stress 10 Pa

(b) Yield stress 100a Pa

Fig. 2.12 Flow history of slump flow tests

The simulation time of V-funnel, modified cone outflow and inverted cone outflow tests is set sufficiently large to cover the full discharge process. The flow process in these outflow tests can be presented in two formats, as shown in Fig. 2.13, where the viscosity varies from 10 to 100 Pa·s and the yield stress is 150 Pa. Fig. 2.13a illustrates the relationship between the discharge time and the residual concrete, represented by the percentage of initial concrete volume in funnel or cone. Fig. 2.13b shows how the area taken by air in the cross section of nozzle changes with time, and the area of air is also represented by percentage. Both types of figures are produced for the extraction of indices. In the former case, all curves can be roughly divided into two linear parts with a remarkable slope difference. The time values at turning points are recorded as the index t_m when majority of the concrete has been discharged. Similarly, the index t_v can also be directly obtained by recording the time when residual concrete drops to certain percentage. Further, by calculating the volume decreasing rate in each time step, $v_{\max\_t}$ can be recorded as the maximum value. For the latter case, t_n is the time when curves begin to increase from zero.

Classification of workability indices

As discussed above, it is fairly straightforward to extract various workability indices once the simulation results are collected. However, when it comes to real-world tests, the efforts required to measure different indices vary greatly, and as a result the workability indices can be grouped into four categories as listed in Table. 2.1. In Group I, there are D and T_{500} of the slump flow test and t_n of for the three outflow tests. The Group I indices are the easiest ones

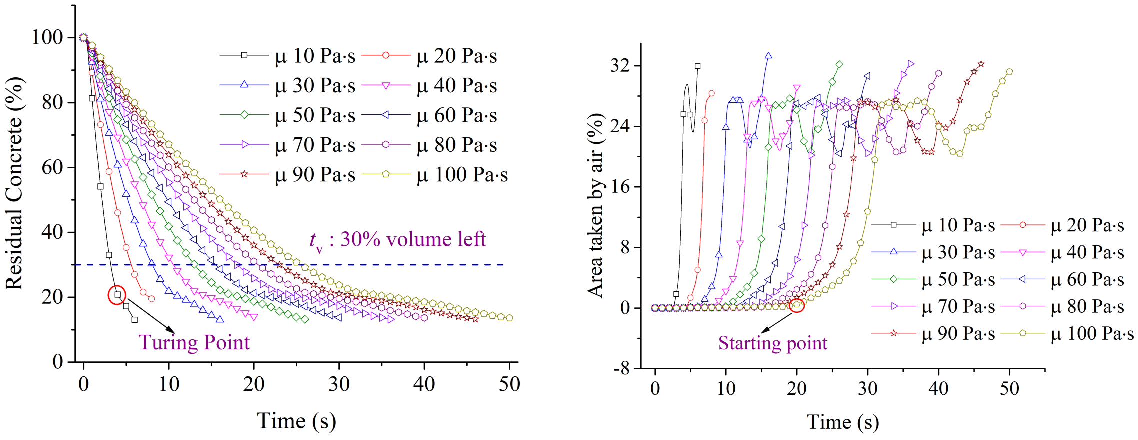

(a) Residual concrete in funnel or cone (b) Area taken by air in cross section of nozzle

Fig. 2.13 Two methods for recording outflow tests (Yield stress 150 Pa)

Table 2.1 Classification of workability indices

Group	I	II	III	IV
Slump Flow Test	D and T_{500}	t_D	$\bar{v}$	$v_{\max\_D}$
V-funnel, Modified Cone Outflow Test and Inverted Cone Outflow Test	t_n	t_m	t_v	$v_{\max\_t}$

to measure and require only one equipment for the measurement. For D, it is a ruler, while for T_{500} and t_n, it is a timer. The Group II indices include t_D and t_m, which also require just one measuring equipment but are more prone to subjective errors. For both t_D and t_m, there is no obvious sign in the practical test for the tester to determine the critical time point for measurement. The Group III indices include $\bar{v}$ and t_V, and they all require more than one measuring equipment. For the former, both timer and ruler are required; for the latter, both timer and volume measuring device are needed. The Group IV indices include $v_{\max\_D}$ and $v_{\max\_t}$, and they are the most difficult ones to measure in practice. The whole testing process must be recorded, and an image processing operation is required to extract the indices.

In view of this classification and the associated constraints in each group, the Group I indices are selected for our study. It is noted that these indices are also recommended by the European Guidelines for Self-compacting Concrete. To further distinguish t_n for the three outflow tests, the value for the V-funnel test will be denoted by t_n', the value for the modified cone outflow test will be denoted by t_n, and the value for the inverted cone outflow test will be denoted by t_n'' in following sections. For outflow tests, the discharge time based on the concrete volume is more comprehensible, hence t_m will also be included to validate t_n for rheology evaluation.

2.2.3 Simulation result and analysis

Slump flow test

Final Diameter *D*

Following the routine stated above, D from all simulation cases of slump flow tests are collected, and two subsequent figures are plotted. To make the figures clear for recognition, some data in dense area is not presented. Fig. 2.14 indicates that D decreases as yield stress increases, and when yield stress is around 100 Pa, the decreasing rate has a dramatic drop. What's more, almost overlapped curves imply that the D is mostly decided by yield stress. But viscosity does have its influence on D. The smaller the yield stress is, the more obvious the influence is. While, when yield stress is above 400 Pa, this influence can be neglected. Fig. 2.15 shows D decreases as viscosity increases. It can be found that the curves are not as smooth as those in Fig. 2.14, because of their different tolerance to the numerical accuracy. Element size of slump flow model is around 5 mm. So, when it comes to D, the accuracy is about 1 cm which is in accordance with the requirement of slump flow test. The occurrence of this unsmooth curves in Fig. 2.15 implies that the influence of viscosity is limited, and the variation is usually within the accuracy of both numerical simulation and real test. Contour plot Fig. 2.16 is a combination of Fig. 2.14 and Fig. 2.15 showing the coupled affect of yield stress and viscosity on D.

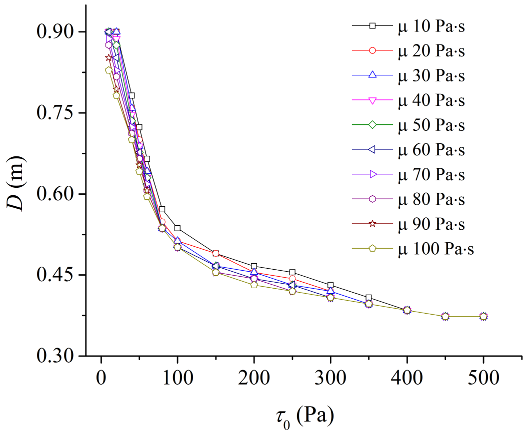

Fig. 2.14 Impact of τ_0 respecting to D

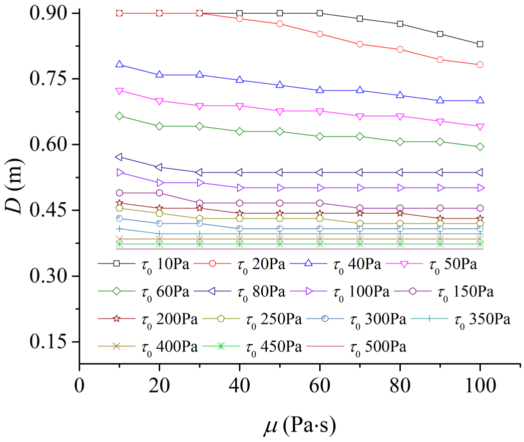

Fig. 2.15 Impact of μ respecting to D

It should be pointed out that the length size of square plate is 0.9 m, which is also same in simulation. So, it can be found that the maximum value of D is fixed to this value for curves belonging to yield stress 10 Pa and 20 Pa. Comparing both figures, it is concluded that the influence of yield stress is nonlinear, while for viscosity, it's almost linear. Besides, D is mostly decided by yield stress, but influence of viscosity also should be considered when

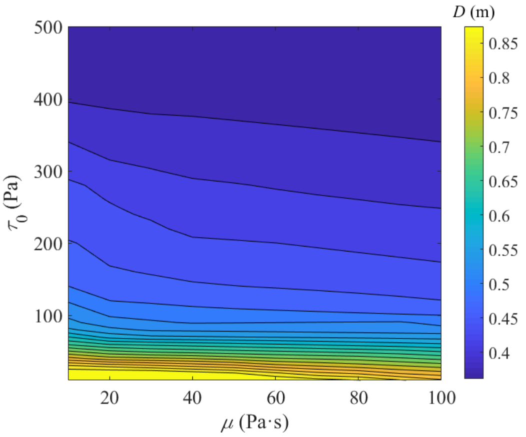

Fig. 2.16 Contour plot of D

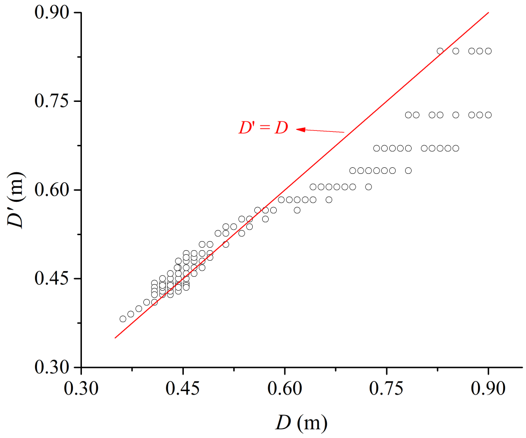

Fig. 2.17 Comparison between D and D'

yield stress is not large. For example, when yield stress is 50 Pa, the interval of diameter is about 8 mm when viscosity increases by 10 Pa·s.

[50] suggested the Eqn. 1.1 to calculate yield stress value from measured D of slump flow test. As his method ignores the impact of viscosity, it is obvious that there will be certain difference between his solution and the simulation method. Apply Eqn. 1.1 to calculate another series of diameter (denoted by D') from the same group of yield stress value, and compare the calculated D' with the simulated D by plotting Fig. 2.17. In this figure, if one dot is located on the red line, it means that the calculated diameter equals to the simulated one. The distribution of these dots indicates that when yield stress is large (small diameter), both solutions give similar result. While, when yield stress is small (large diameter), viscosity will cause large variation in diameter (which also has been pointed out by [9]). And when viscosity is lower than 100 Pa, Eqn. 1.1 usually underestimates the D. In the same range, when it comes recalculation of yield stress from slump flow test, Eqn. 1.1 also underestimates the value of yield stress.

T_{500}

Repeating the same procedure stated above, the figures showing relationship between rheological properties and T_{500} are plotted. Fig. 2.18 shows that T_{500} increases nonlinearly as the yield stress grows larger, and the increasing rate accelerates synchronously. The relationship between viscosity and T_{500} is given in Fig. 2.19, and T_{500} increases almost linearly as viscosity becomes larger. Comparing with D, viscosity plays a more important role in determining T_{500}. Contour plot Fig. 2.20 presents the coupled influence of yield stress and viscosity on T_{500}.

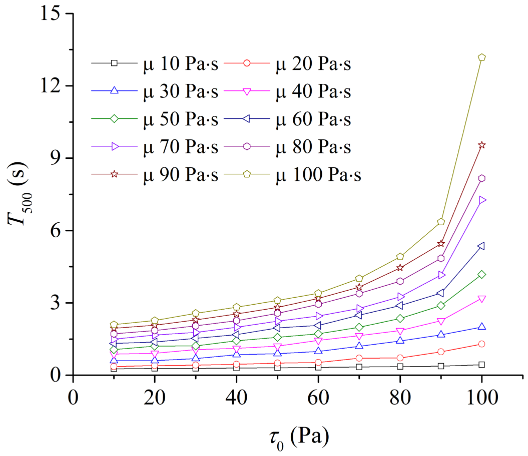

Fig. 2.18 Impact of τ_0 respecting to T_{500}

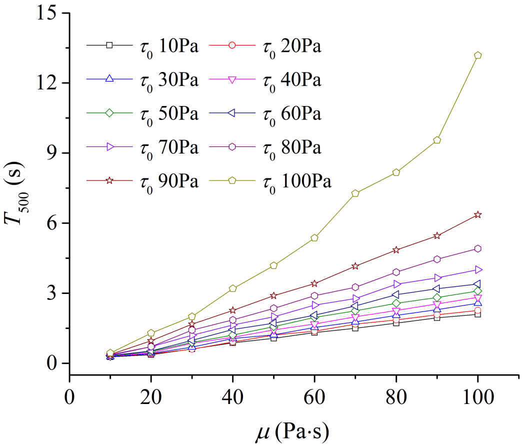

Fig. 2.19 Impact of μ respecting to T_{500}

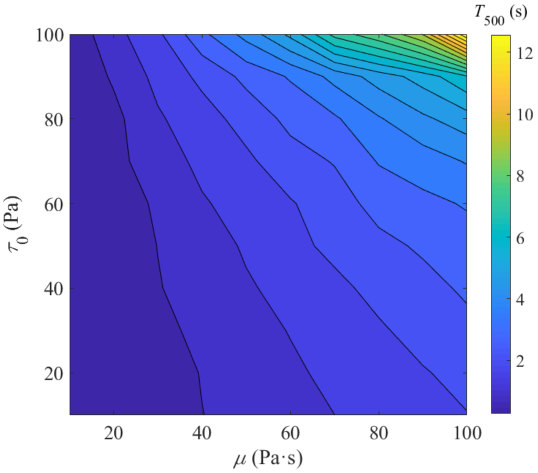

Fig. 2.20 Contour plot of T_{500}

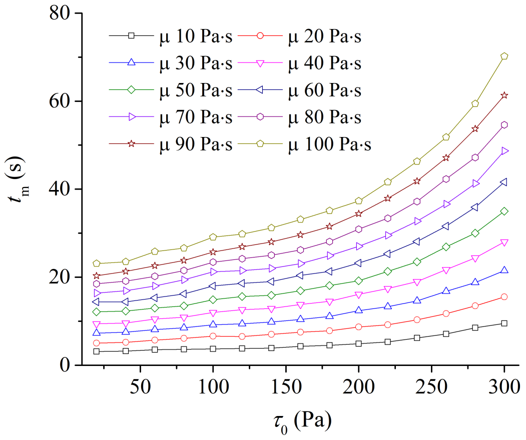

Fig. 2.21 Impact of τ_0 respecting to t_m

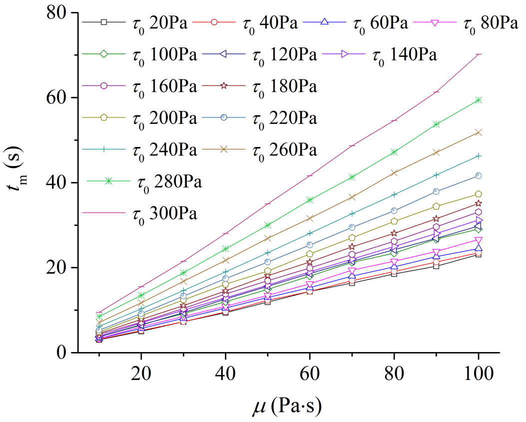

Fig. 2.22 Impact of μ respecting to t_m

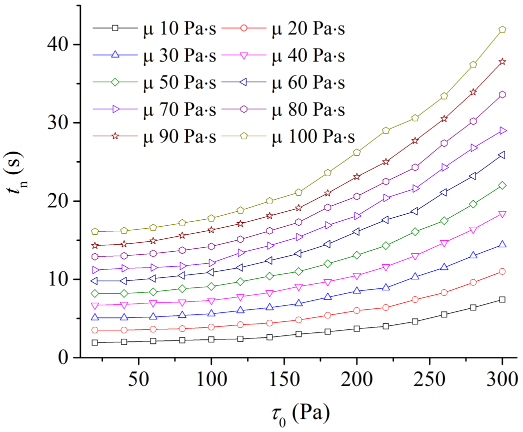

Fig. 2.23 Impact of τ_0 respecting to t_n

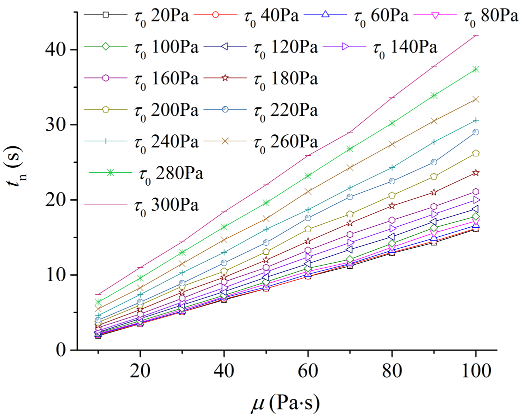

Fig. 2.24 Impact of μ respecting to t_n

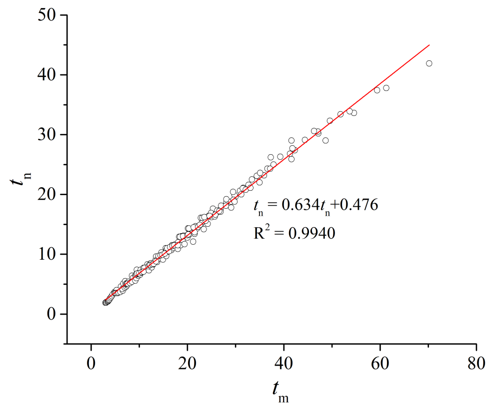

Fig. 2.25 Linear Relationship between t_n and t_m

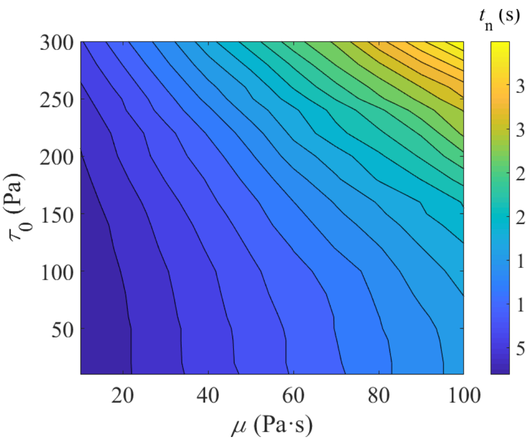

Fig. 2.26 Contour plot of t_n

V-funnel test

Processing output data of V-funnel test simulations, summary of two groups of discharging time t_m and t_n are made as plotted in Fig. 2.21 to Fig. 2.24. It's noticeable that, although the range of their value differs greatly, the corresponding curves share the same trend. Further, quantitative relationship between them is presented by Fig. 2.25, which is highly linear. Based on the this figure, conclusion can be made that two indices imply exactly the same rheological characteristic of concrete. So, index t_n alone is enough to represent the V-funnel test result.

The Fig. 2.21 to Fig. 2.24 show again that the influence of yield stress is nonlinear and for the viscosity it's linear. It can be found that the discharge time is mostly decided by viscosity when yield stress is under 100 Pa. Fig. 2.26 is the contour plot of t_n, which gives the synthesized influence of yield stress and viscosity.

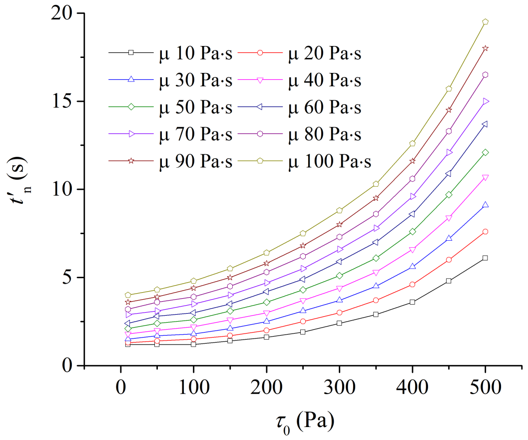

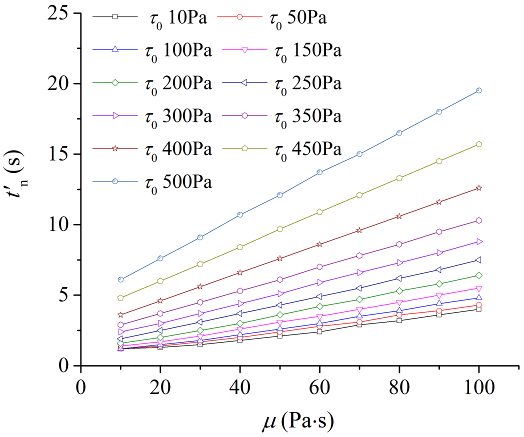

Fig. 2.27 Impact of τ_0 respecting to t'_n Fig. 2.28 Impact of μ respecting to t'_n

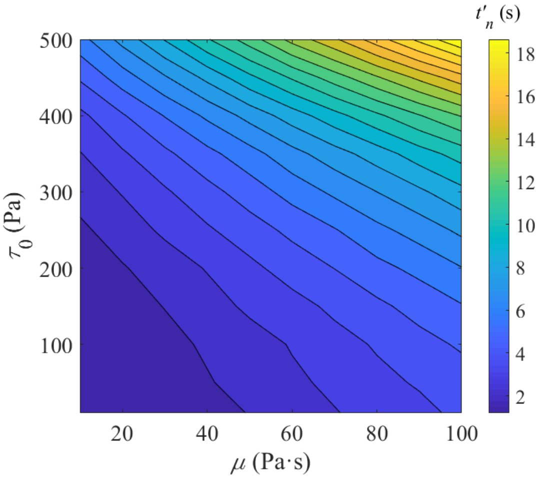

Fig. 2.29 Contour plot of t'_n

Modified cone outflow test

The summary of simulation result of modified cone outflow test is shown in Fig. 2.27 and Fig. 2.28. As explained in last section, index t'_n is the only discussed. Comparing with V-funnel test, the modified cone outflow test could cover a wider range of yield stress, and value of t'_n is much smaller. The corresponding curves share the same evolution trend that the influence of yield stress is nonlinear, while for the viscosity it's linear. Fig. 2.29 is the contour plot of t'_n, and all isolines are almost linear. While, referring to Fig. 2.26, isolines will turn vertically when yield stress is very low. It should be noticed that, when yield stress or viscosity is very small, the discharge time will be too short for human eye to promise its accuracy. So, this modified cone outflow test suggested by EFFC is better to be used for concrete having large yield stress.

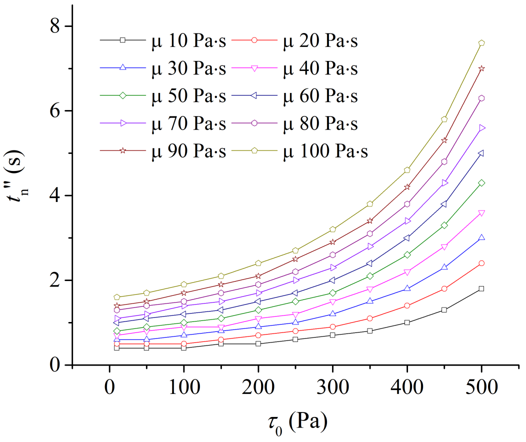

Fig. 2.30 Impact of τ_0 respecting to t_n''

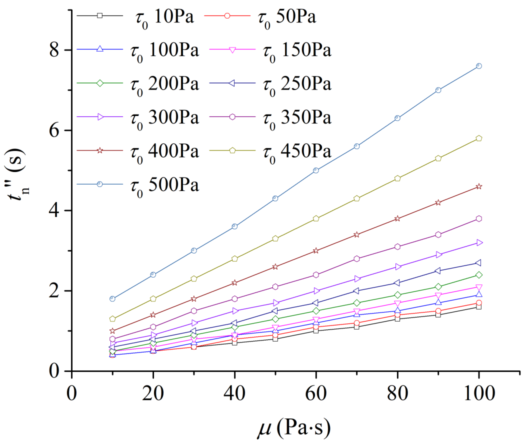

Fig. 2.31 Impact of μ respecting to t_n''

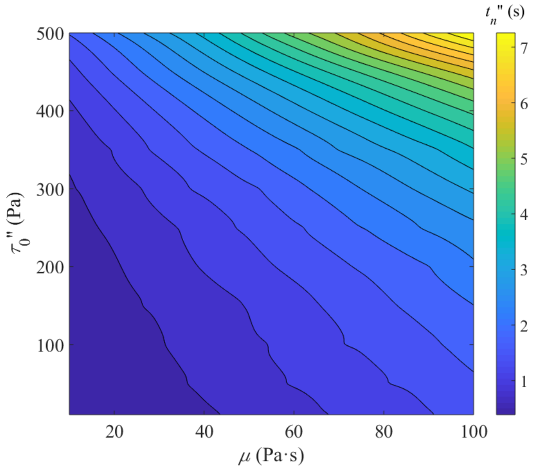

Fig. 2.32 Contour plot of t_n''

Inverted cone outflow test

Fig. 2.30 and Fig. 2.31 give the simulation result of inverted cone outflow test, which are similar to that of modified cone outflow test. But the range of t_n'' is only half the value of t_n'. The contour plot Fig. 2.32 also looks the same with Fig. 2.26 but has lower t_n'' value. It's clear that inverted cone outflow test is also suitable for concrete with large yield stress.

Relationship between slump flow test and V-funnel test

It can be concluded that performance of slump flow test, V-funnel test, modified cone outflow test and inverted cone outflow test depends on both yield stress and viscosity. Theoretically, results of either two tests are sufficient to solve the two parameters of Bingham model. Considering that slump flow test and V-funnel test are standard tests, they are firstly chosen to study the aimed relationship. In addition, as T_{500} is only available for yield stress within 100 Pa, D and t_n are the chosen. After attempting for functions matching for Fig. 2.16 and Fig. 2.26, it's found that they both followed the routine of power functions. But, because of the various high orders of yield stress, the direct solution to solve yield stress and viscosity by explicit expression of D and t_n is not available. Thus, the aimed relationship is expressed in another way as shown in Fig. 2.33 to Fig. 2.35.

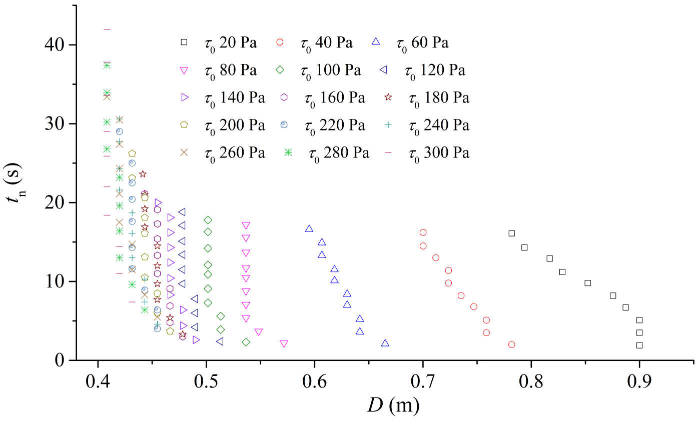

Fig. 2.33 Corresponding (D, t_n) Sharing the Same (τ_0, μ)

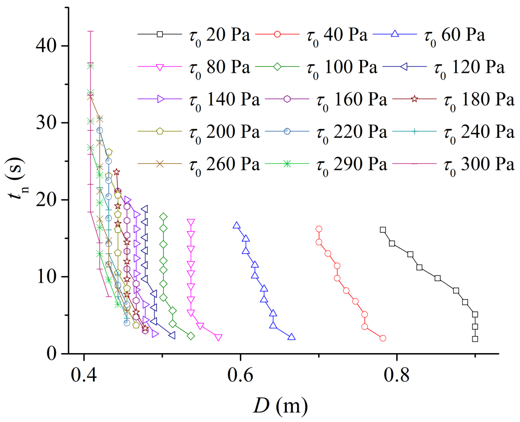

Fig. 2.34 Curves Based on Constant τ_0

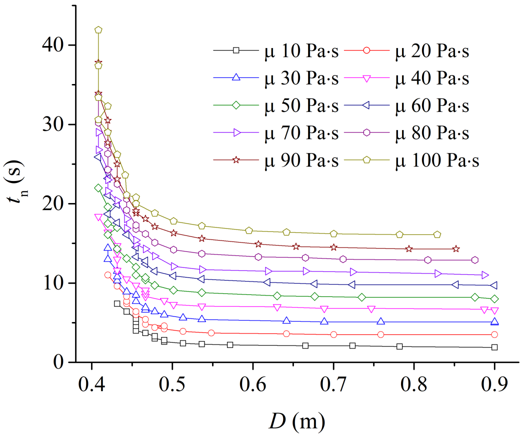

Fig. 2.35 Curves Based on Constant μ

For each pair of yield stress and viscosity, one slump flow test simulation and one V-funnel test simulation are performed, which subsequently output one pair of D and t_n. Every dot in Fig. 2.33 represents such a pair of output data. In this figure, dots in the same colour share the same yield stress value,and Fig. 2.34 is plotted by linking each group of them together. From bottom to top of each group of coloured dots in Fig. 2.33, their viscosity value increases by an interval of 10 Pa·s. So, linking the dots sharing the same viscosity gives the Fig. 2.35.

It's comprehensible that each pair of yield stress and viscosity decides one specific concrete mixture. Distribution of curves in Fig. 2.34 shows how yield stress affects the performance of both tests. Fig. 2.35 present test result in the way that curves show how viscosity affects two test results. For the former, when D becomes smaller, the gap between two adjacent curves becomes narrower. While for the latter, the curves approximately distribute uniformly. If overlapping these two figures, the two groups of curves form a net which expresses a complete corresponding relationship between (τ_0,μ)) and (D, t_n), just as Fig. 2.36. In other words, rheological properties of certain concrete mixture can be obtained directly from D and t_n by referring to this figure.

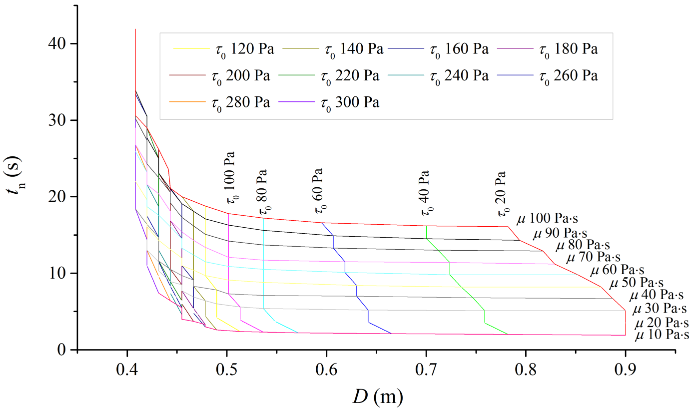

Fig. 2.36 Relationship between (D, t_n) and (τ_0, μ)

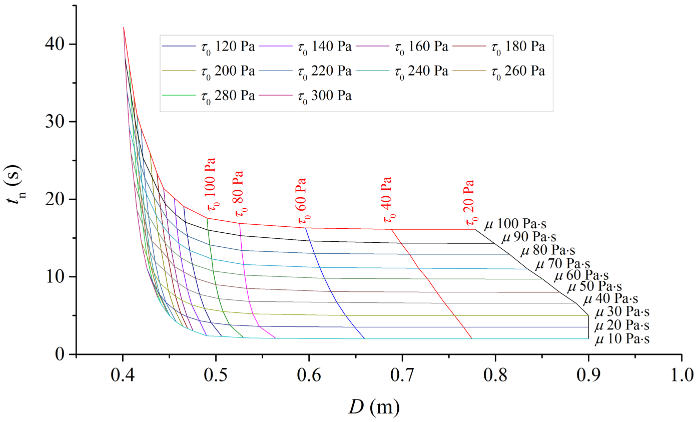

Fig. 2.37 Adjusted Relationship between (D, t_n) and (τ_0, μ)

Theoretically, the resulting curve with either fixed yield stress or viscosity should be smooth and monotonous. While, in Fig. 2.37, it's easy to recognize that the trend of curves is monotonous, but their smoothness is not satisfying. In some local area, curves even cross each other which is unreasonable. These phenomena all result from the accuracy limitation of two sets of simulation data. The numerical error of D, as given earlier, is 10 mm. For t_n, the error is mainly introduced by data processor. As time scale varies, it's hard to set a fixed criterion for all cases, and the critical time for t_n is decided by processor subjectively. Although, the curves relating to t_n look quite smooth, certain error is inevitable but limited. Starting from the above knowledge, Fig. 2.36 can be improved by slight adjustment of simulation result according to the following constraints: (1) two groups of curves should be monotonous; (2) the first derivative of all curves should be monotonous; (3) the maximum adjusted value for D is set as 10 mm; (4) the maximum adjusted value for t_n is 0.3 s.

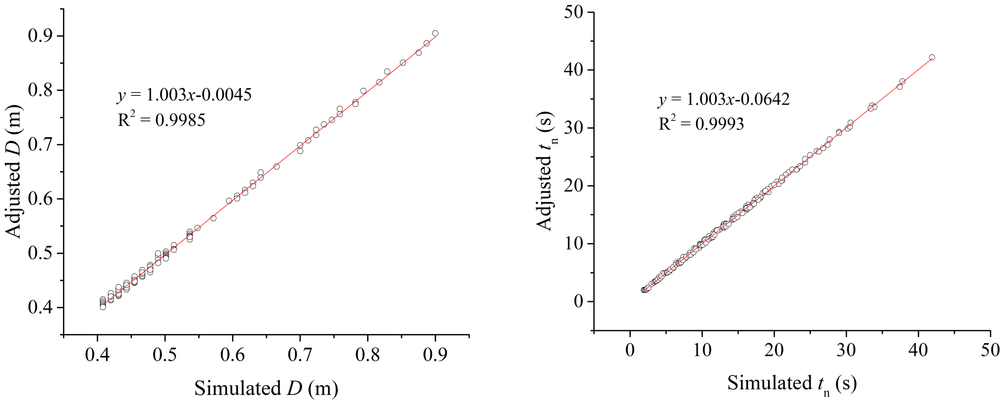

(a) D (b) t_n

Fig. 2.38 Comparison between simulated data and adjusted data

The improved figure is plotted in Fig. 2.37 based on the adjusted data, which looks much reasonable than Fig. 2.36. Then, the quality of new sets of D and t_n are checked as shown in Fig. 2.38. They are compared with the original value from simulation, and the adjustment is found to be satisfying. Both fitting functions of two series of data can be regarded as $y = x$, which means the simulated value equals to the adjusted value. In addition, the coefficients of determination of both fitted functions are above 0.998. As a conclusion, the adjustment for original simulation are acceptable.

Because the curves in left part of Fig. 2.37 are so close to each other, the whole figure is further divided into four parts (given in Fig. 2.39) for better recognition. Fig. 2.39a is for curves where yield stress is below 100 Pa. Fig. 2.39b shows the part of curves where yield stress is within 100 200 Pa. Fig. 2.39c is for the area where yield stress is above 200 Pa and viscosity is larger than 40 Pa·s. Fig. 2.39d is for the rest where yield stress is above 200 Pa and viscosity is below 30 Pa·s.

For Fig. 2.39a and Fig. 2.39b, they are easy to read and recognize the difference between curves. But the intervals between curves with constant yield stress in Fig. 2.39c and Fig. 2.39d are all smaller than 10 mm, whose value is less than the accuracy of D. That means value

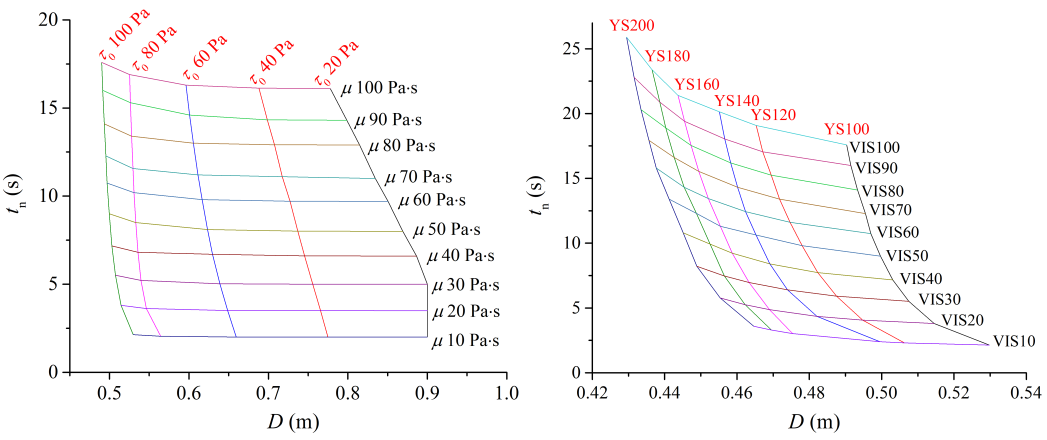

(a) $\tau_0 < 100$ Pa; μ: all (b) τ_0: 100 $\sim$ 200 Pa; μ: all

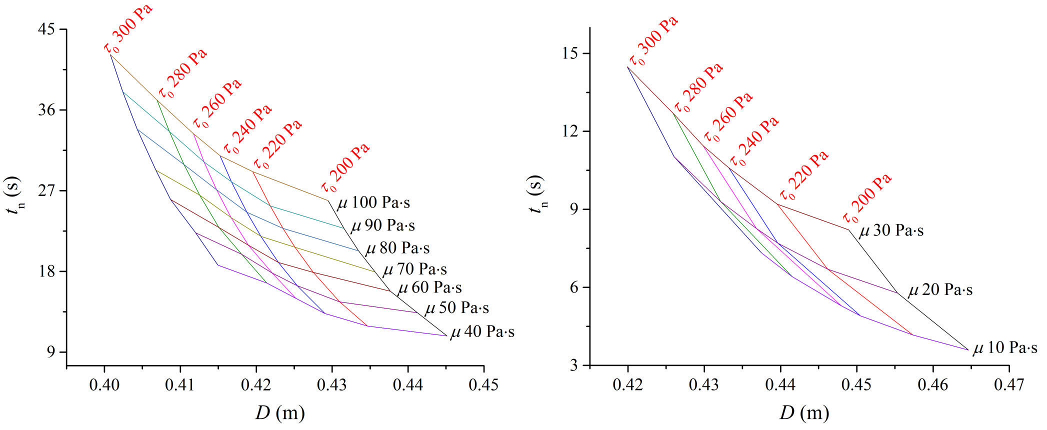

(c) $\tau_0 > 200$ Pa; μ: 40 $\sim$ 100 Pa·s (d) $\tau_0 > 200$ Pa; μ: 10 $\sim$ 30 Pa·s

Fig. 2.39 Relationship between (D, t_n) and varied (τ_0, μ)

in these two figures are inaccurate. Not only for this numerical model but also for real test, when yield stress is large than 200 Pa, slump flow test is not available to achieve a yield stress value with an accuracy smaller than 20 Pa.

It's also noticed that, in Fig. 2.36 and Fig. 2.37, both groups of curves tend to converge to a certain boundary when yield stress grows larger. So, it can be imagined that when yield stress keeps growing, the accuracy of slump flow will still becomes worse.

Relationship between slump flow test and modified cone outflow test/inverted cone outflow test

Repeating the same processing method, the relationship between slump test and modified cone outflow test/inverted cone outflow test can be obtained, as given in Fig. 2.40 and Fig. 2.41. It can be seen that two groups of graphs look very similar, and the major difference is the scale of discharge time. Especially, when yield stress is above 400 Pa, the variation of D is within 10 mm when viscosity changes in the range of $10 \sim 100$ Pa·s. But with a interval of 50 Pa, there are significant gaps (10 mm) between vertical curves. That suggests 50 Pa is reasonable unit to characterize the yields stress of concrete. At the same time, it should be stressed again that when yield stress is small like below 100 Pa, the discharge time is so small, especially for inverted cone outflow test, that the subjective error from the tester will take a larger proportion in the measured value, which makes the value less reliable when comparing with V-funnel result.

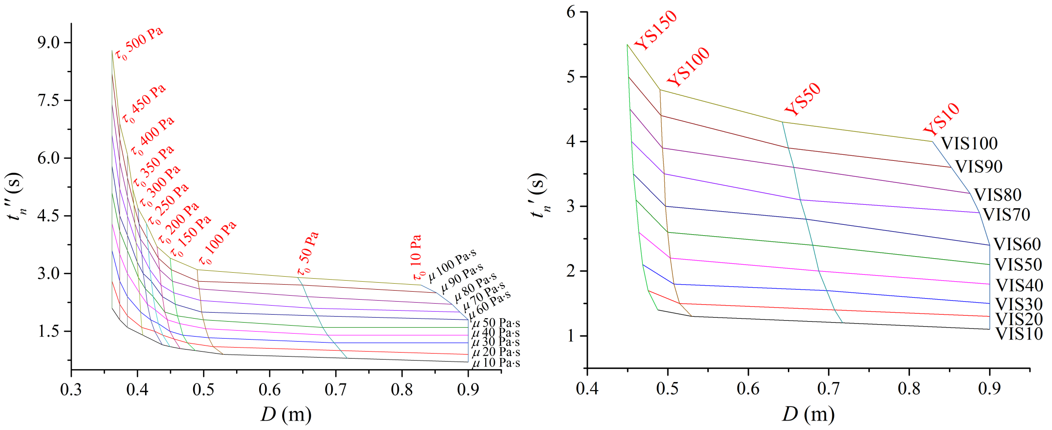

(a) Full Range

(b) τ_0: $10 \sim 150$ Pa

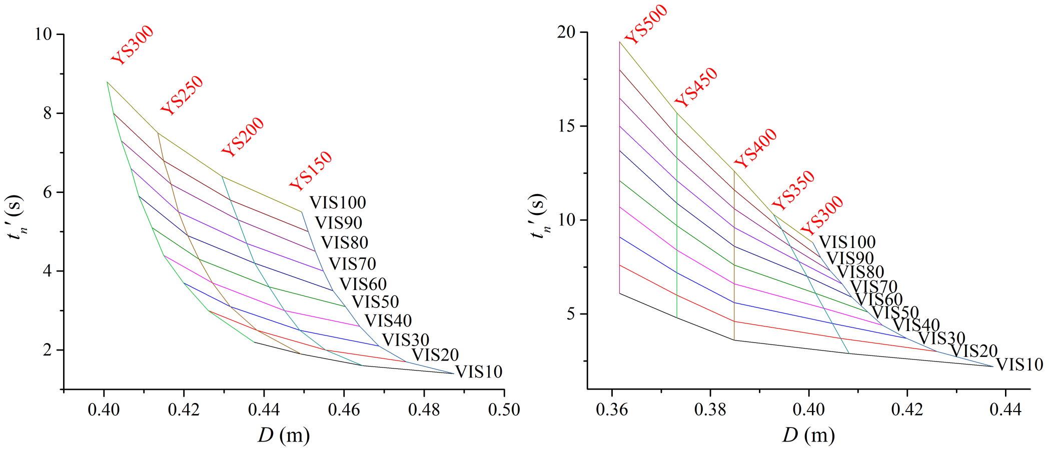

(c) τ_0: $150 \sim 300$ Pa

(d) τ_0: $300 \sim 500$ Pa

Fig. 2.40 Relationship between (D, t_n') and varied (τ_0, μ)

2.2.4 Conclusions

The key aim of this chapter is to quantify the relationship between the flow behaviour of SCC and its rheological properties. The whole study is based on numerical simulation of

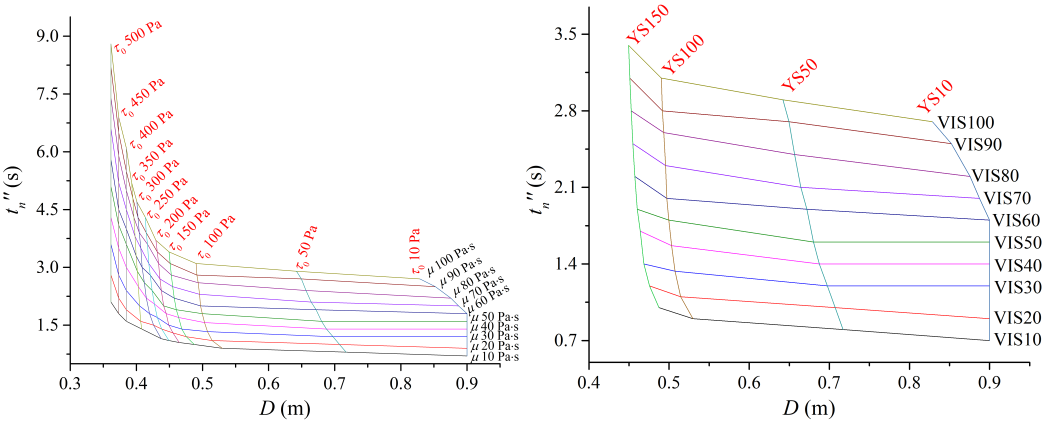

(a) Full Range

(b) τ_0: 10 ∼ 150 Pa

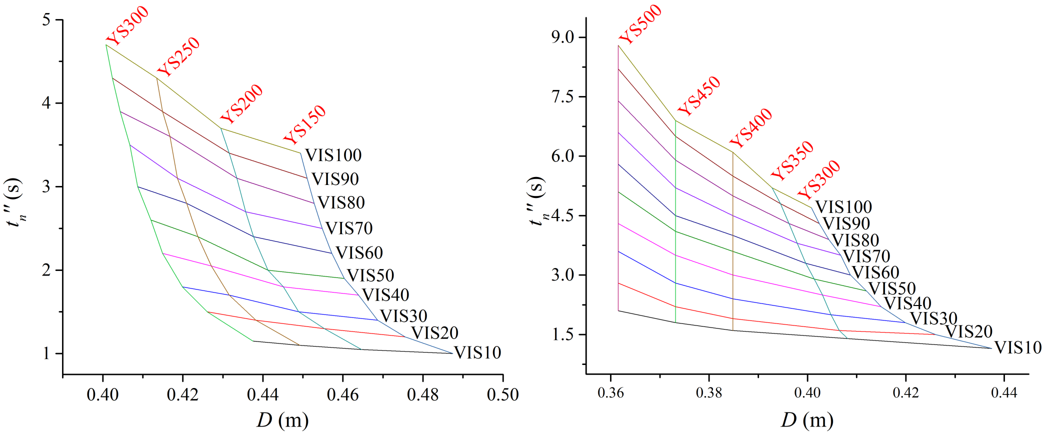

(c) τ_0: 150 ∼ 300 Pa

(d) τ_0: 300 ∼ 500 Pa

Fig. 2.41 Relationship between (D, t_n'') and varied (τ_0, μ)

4 simple tests: slump flow test, V-funnel test, modified cone outflow test and inverted cone outflow test. The former two are standard tests, and the rest two are proposed by researchers in recent years. Comparing with previous studies in this area, our method has the following advantages. Comparing with solution by experiments, the unpredicted variation of concrete mixture can be avoided by numerical method; comparing with theoretical solution based on different kinds of assumptions, our method is more realistic; comparing with previous various numerical study, our study gives a systematic and practical result. Processing the output of simulations, many indices are able to be captured. But considering the complexity to obtain them in real tests, they can be divided into 4 groups. This study only focuses on the easiest indices (D and t_n) for thorough analysis. The following are key conclusions of our study. (1) For all 4 tests, the influence of yield stress in nonlinear, while the viscosity is linear. (2) Theoretically, either of two indices are sufficient to determine both yield stress and viscosity, but no explicit highly accurate expressions for them are available. (3) In space

formed by orthogonal D and t_n (also t'_n and t''_n), two groups of curves can be plotted, and they form a closed net. They represent the test performance of concrete with constant yield stress or viscosity respectively. This figure can be used to determine concrete properties based on test result of slump flow test and any of the 3 outflow tests. (4) When yield stress is above 200 Pa, the accuracy of slump flow test is larger than 20 Pa; when yield stress is above 400 Pa, an interval of 50 Pa in yield stress is enough to distinguish the performance difference in slump flow test of different concrete mixture. (5) V-funnel test is only effective when yield stress is under 300 Pa; modified cone outflow test/inverted cone outflow test finish too quick while yield stress is small. Therefore, V-funnel test is suitable for concrete with low yield stress, while other tests would benefit for concrete with large yield stress.

2.3 Application: casting of diaphragm wall

In this part, the cast of a diaphragm wall is used as an example to demonstrate the application of the easy-to-use charts. In practice, the concrete is usually prepared off-site and will be transported to the site conforming to a strict timetable in the casting of construction. The transportation usually costs several hours, so workability tests will be performed to check the concrete quality before it's poured. According to the test result, the quantitative rheological properties can be obtained directly by referring to the relation charts. Thus, the casting process of the diaphragm wall can be simulated based on the timetable of concrete placement.

In this study, the mixture model [58] in ANSYS Fluent will be used to simulate the multiphase concrete flow in the diaphragm wall. As a comparison, two simulations were run for homogeneous concrete and heterogeneous concrete respectively. The success in simulation approves that the charts given by the last section pave the gap between practice and numerical simulation, and the Fluent mixture model is feasible for the complex multiphase concrete flow simulations.

The study of this section is divided into 4 steps: geometry simplification; the determination of representative concrete phases; the concrete placement procedure; the carrying out of simulations.

2.3.1 Simplification of geometry

The diaphragm wall has a dimension of 10 $m \times 6\ m \times 1\ m$ (depth, width and thickness respectively). Two different cages are placed in the wall, and in each of them, there is a tremie pipe whose bottom is always embedded in concrete. And new concrete is cast into the wall through the two pipes. The geometry of the diaphragm wall is very simple, however, the real rebar cage is very complicated. Compared with the scale of the diaphragm wall, the size of the rebar is very small. So, to make the computational cost available, the two rebar cages were simplified according to Table 2.2.

Table 2.2 Simplification of actual rebar cage and tremie

No.	Actual rebar cage design	Simplified rebar geometry
1	Contact between rebars	Linked rebars
2	Circular rebar	Square rebar
3	Hook of stirrup	Ignored
4	Crossed stirrup	Paralleled stirrup
5	Various rebar diameters	Same size
6	Two-layer rebar	One layer
7	Various spacing in 3 directions	Fixed spacing
8	L-shape coupler rebar	Ignored
9	Circular tremie	Square tremie

(1) Rebars are linked to each other instead of contacting each other to eliminate contact faces.

(2) Hooks of stirrup are ignored and crossed parts are replaced by paralleled ones to reduce numerous details.

(3) Two-layer rebars are all reduced to one layer.

(4) Cross-section of rebars is set to be square and all have the same size ($0.03m \times 0.03m$) to form a closed structure without local small size region, as shown in Figure 2.42. It should be noted that the two cages are not identical, and the left cage is smaller than the right one.

(5) The actual rebar cage contains four spacing patterns for horizontal stirrups. For the simplified geometry, the rebar distribution in the thickness direction is set to be virtually the same as Section B in the Layout of Diaphragm Wall, with slight modification to benefit further meshing work (details can be found in Figure 2.43). As a further simplification, the rebar spacing in the depth direction is set as $0.3m$ for the whole cage.

(6) L-shape coupler rebars are not included in the simplified geometry.

(7) For easier meshing, the circular tremies are also changed to be square ones ($0.27m \times 0.27m$) with the same cross-section area. The position of the two tremies is presented in Figure 2.43, and their length is $9.5m$.

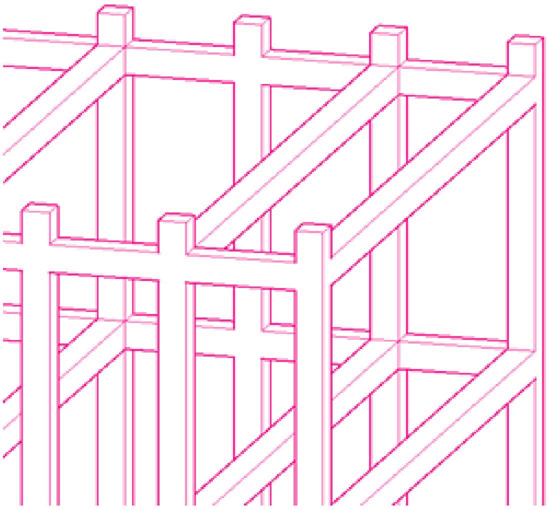

Fig. 2.42 Example of simplified rebar cage

The final geometry is shown in Figure 2.44, and it was meshed by tetrahedron elements as given in Figure 2.45.

2.3.2 Rheological properties of concrete mixtures

There are two different non-Newtonian fluids involved in the concrete placement: the bentonite slurry and the concrete mix. The latter is cast during the excavation to support the borehole from failure. Then, in the cast of concrete, the slurry will be driven out of the hole gradually. In this simulation, the rheology of the bentonite slurry is considered constant. While, the variation in rheological properties of concrete mixes is considered, which can be obtained from the record of on-site slump flow test and invert cone test. As discussed in the literature review, both slurry and concrete are Bingham fluid.

For the bentonite slurry, its density (1080 kg/m^3) and Marsh funnel test result (36 s) were given in the original report. According to the work of Pitt et al., [68], slurry viscosity can be calculated from the Marsh funnel test result, which gives $0.06558 Pa \cdot s$. However, the information for yield stress is limited, so its value is chosen as 10 Pa which is suggested by the EFFC guide [87].

For concrete mixes, as shown in Figure 2.46, the testing results shows a large variation. The horizontal axis represents the discharging time of the invert cone test and the vertical axis is for the spreading diameter of the slump flow test. The former varies from the 1.5 s to 22 s, and the latter is in the range of 320 mm to 800 mm. It indicates concrete rheology differs greatly from truck to truck. Theoretically, it would be perfect if we can recover the properties for every truck of concrete, and simulate the real concrete placement procedure. However, such an arrangement needs to create an individual phase for every truck of concrete, which makes the simulation cost unacceptable. Instead, a smaller random sample of 9 was chosen in the heterogeneous case, as listed in Table 2.3.

Table 2.3 Workability indices of 9 representative concrete mixes

Concrete mixes	**CM1**	**CM2**	**CM3**	**CM4**	**CM5**	**CM6**	**CM7**	**CM8**	**CM9**
Flow Time (s)	4.0	3.7	3.2	6.0	6.3	8.7	11.2	2.0	4.0
Diameter (mm)	470	520	630	400	550	550	480	500	750

Referring to Figure 2.41, the corresponding Bingham parameters were determined and they are listed in Table 2.4. The maximum viscosity is $160 Pa \cdot s$ and the minimum is $60 Pa \cdot s$. The yield stress varies in the range of $40 Pa$ to $350 Pa$. For the homogeneous case, the Bingham parameters are obtained from the averaged workability indices. The latter give discharge time $4.9 s$ and spreading diameter, and the former are viscosity 160 $Pa \cdot s$ and yield stress 90 Pa. This concrete is denoted by CM0 in the following discussion.

Table 2.4 Bingham parameters of 9 representative concrete mixes

Concrete mixes	**CM1**	**CM2**	**CM3**	**CM4**	**CM5**	**CM6**	**CM7**	**CM8**	**CM9**
Viscosity ($Pa \cdot s$)	120	120	160	120	200	240	250	60	160
Yield stress (Pa)	200	110	60	350	80	80	150	130	40

2.3.3 Setup of case studies

As recorded in the Concrete Pour Report, there were 10 trucks of concrete poured into the diaphragm wall. Each truck contained a different volume of concrete, but the total volume poured via each tremie was almost the same. The casting duration for each truck was about 5 minutes while some of them experienced considerably longer time.

The placement process needs to be simplified to facilitate the simulation setup. Firstly, it is assumed that every truck contains the same amount of concrete. Secondly, 10 trucks of concrete are placed into the wall in total, which means 5 trucks for each tremie, and 1 truck of concrete contributes to $1 m$ height in the diaphragm wall. Besides, it is further assumed that each truck is emptied in 5 minutes, and the placement process in two tremies takes place in parallel. For example, when the casting of the n-th truck begins at the left tremie, it's also the starting time of the n-th truck at the right tremie.

The length of two tremies is $9.5m$, so the distance between the tremie ends and the wall bottom is $0.5m$. So, the concrete will go to the wall bottom directly and pile up gradually. When the height of concrete reaches the tremie ends, the latter will be embedded since then. After that, the concrete from the tremie will go into the concrete layer, which pushes up the concrete level and drives the slurry of the wall from the top. The new concrete won't get in touch with slurry anymore so that the concrete properties won't be changed.

To study the influence of rheology variation on the concrete flow in the diaphragm wall, two contrast simulations were designed. In Case 1, the concrete was treated as homogeneous material and the value has been given in the last section. In Case 2, 9 different concrete phases were used as given in Tabel 2.4. The 10 pouring of concrete from different trucks were arranged as shown in Table 2.6. The 9 concrete phases were assigned in a random order to the 10 batches of concrete, and CM6 was repeated twice. Adding the slurry phase, there were 10 different phases in total corresponding to the Table 2.4. For the homogeneous Case 1, although there two different phases, 10 batches of concrete with the same Bingham parameters were used either to visualize the concrete of different batches, by which the concrete distribution of two cases can be compared. The arrangement of this Case 1 is listed by Table 2.5.

Table 2.5 Arrangement of concrete casting in Case 1

	Left1/Right1	**Left2/Right2**	**Left3/Right3**	**Left4/Right4**	**Left5/Right5**
Left Tremie	CM0	CM0	CM0	CM0	CM0
Right Tremie	CM0	CM0	CM0	CM0	CM0
Time (s)	$0 \sim 300$	$300 \sim 600$	$600 \sim 900$	$900 \sim 1200$	$1200 \sim 1500$

Table 2.6 Arrangement of concrete casting in Case 2

	Left1/Right1	**Left2/Right2**	**Left3/Right3**	**Left4/Right4**	**Left5/Right5**
Left Tremie	CM8	CM6	CM4	CM3	CM1
Right Tremie	CM2	CM7	CM6	CM5	CM9
Time (s)	$0 \sim 300$	$300 \sim 600$	$600 \sim 900$	$900 \sim 1200$	$1200 \sim 1500$

2.3.4 Simulation results and concrete

The two cases were run by the mixture model of ANSYS Fluent, which is capable of efficient multiphase flow simulation. In each case, 10 fluid phases were created to capture the concrete distribution of different batches and the clear bentonite slurry. The final results of both cases at time 1500 s are presented in Figure 2.47 to 2.52, showing the spatial distribution of different phases.

The contour plots of bentonite slurry at different places are given by Figure 2.47 and 2.48 for Case 1 and Case 2 respectively. The number in legend means the volume fraction of slurry, where 0 (blue colour) means no slurry and 1 (red colour) is for pure slurry. For each case, two views are provided: the middle section of the wall in the thickness direction; the wall surface. Ideally, when the concrete level rose to the wall top, all slurry was supposed to be driven out the wall. However, there is always a certain amount of slurry left in the tremie pile in practice, which causes defects in the final structure. This phenomenon can be observed in both Cases. Comparing the two sets of figures, we can see the existence of differences in slurry residual. However, it's not significant in terms of the position of appearance and the amount of residual.

The concrete contours are presented in Figure 2.49 and 2.50 for Case 1 and Case 2 respectively. The number in their legends represent the concrete phase of different batches, which is ordered according to Table 2.6. Number 2 to 10 is for CM1 to CM9 respectively, and the number 1 for slurry phase which is not shown in the legends. The two sets of contour plots clearly show the final distribution of every concrete phase in two views: the middle section in the direction of thickness; the external wall faces. Again, the difference can be observed between the two cases, but the overall pattern is very similar. This phenomenon is also true in other views as given in Figure 2.51 and 2.52. Each subfigure is composed of sequential cross-sections in the width direction, and the digit on the right of every sectional contour is the distance of the current section to the left wall surface. The two figures clearly show a profound similarity on the right half diaphragm wall but a significant difference on the left half. Let's look back to the concrete properties in the two halves which are summarized and analyzed in Table 2.7. Comparing it with the homogeneous case with viscosity 160 $Pas \cdot s$ and yield stress 90 Pa, the right half has very averaged value for both parameters which gives 194 $Pa \cdot s$ and 92 Pa. While, for the left half, the viscosity 140 Pa is a bit smaller but the yield stress 164 Pa is almost twice of the homogeneous case. Regarding the standard deviation, the left half shows a relatively large value for the yield stress. In conclusion, both significant differences are from the yield stress design which is indicated to be the source of differed distribution in two cases. However, the quantitative influence of such differences requires further investigation.

Table 2.7 Material properties in two halves of diaphragm wall

Batch	Phase		Viscosity $(Pa \cdot s)$		Yield stress Pa	
	Left	Right	Left	Right	Left	Right
1	8	2	60	120	130	110
2	6	7	240	250	80	150
3	4	6	120	240	350	80
4	3	5	160	200	60	80
5	1	9	120	160	200	40
AVG.	–	–	140	194	164	92
STD.	–	–	66	55	117	41

AVG. denotes the averaged value; STD. denotes standard deviation.

2.4 Conclusions

In this chapter, the workability-rheology chart generated in the last section was successfully applied to simulate the cast of a full-scale diaphragm wall. According to the record of on-site workability tests, the rheological properties of fresh concrete from every truck were obtained. Then, a smaller concrete sample of 9 was generated to represent the variation in rheology, and the real casting procedure was simplified accordingly. Finally, 2 comparative cases were designed which consider ideal concrete and varied rheology respectively. It would indicate how rheological variation could affect the concrete flow. The simulations were carried out by mixture model ANSYS Fluent and 10 phases were created in each case. The final distribution of all concrete phases and slurry phase are presented by various contour plots. It shows that the variation in concrete rheology does affect concrete flow behaviour, but the overall patterns of both cases are still quite similar.

This study is only a demonstration of the real-scale concrete casting simulation. It proves the feasibility of the workability-rheology chart given by the parametric study. This setup works well as a preliminary study. However, in terms of studying the mechanics of defects, the pure fluid assumption on concrete is limited greatly. It's hard to quantify the relationship between the defects and a certain local phenomenon under this setup, especially the influence of interaction between rebars and aggregate. For this purpose, the CFD-DEM approach will be introduced and developed.

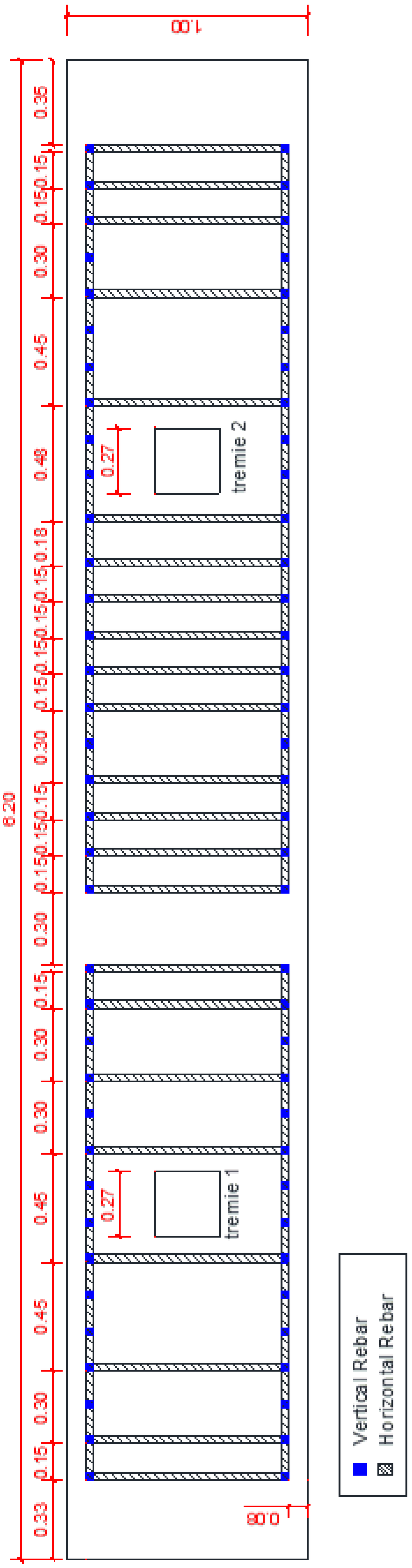

Fig. 2.43 Cross section of rebar cage

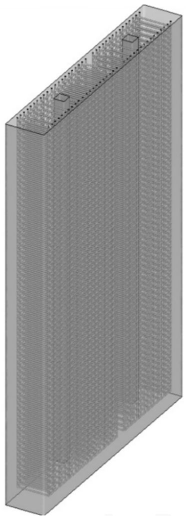

Fig. 2.44 Geometry of the diaphragm wall

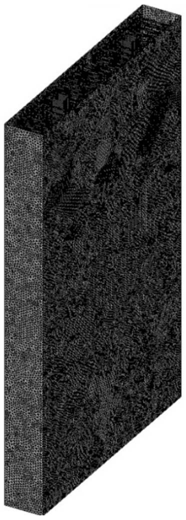

Fig. 2.45 Mesh of the diaphragm wall

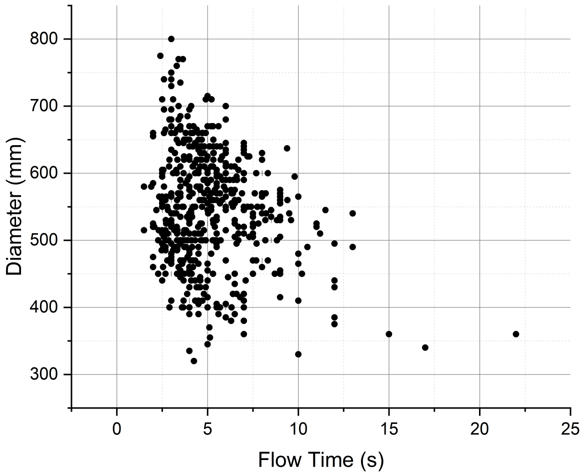

Fig. 2.46 Summary of concrete workability tests

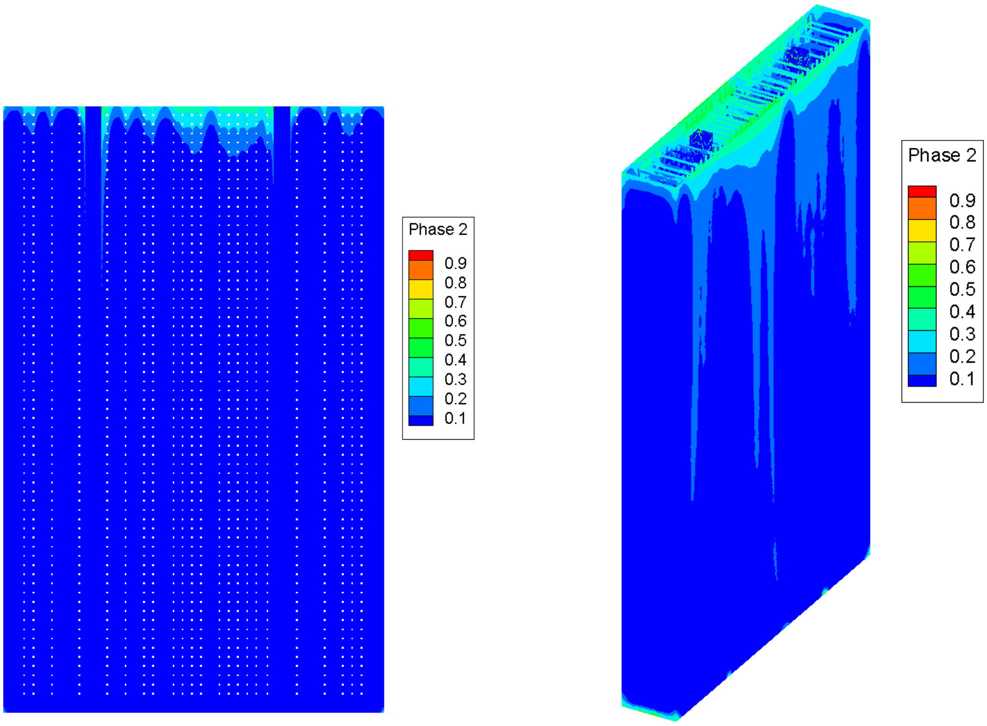

(a) Middle cross section (b) Wall surface

Fig. 2.47 Case 1: bentonite volume fraction in the wall

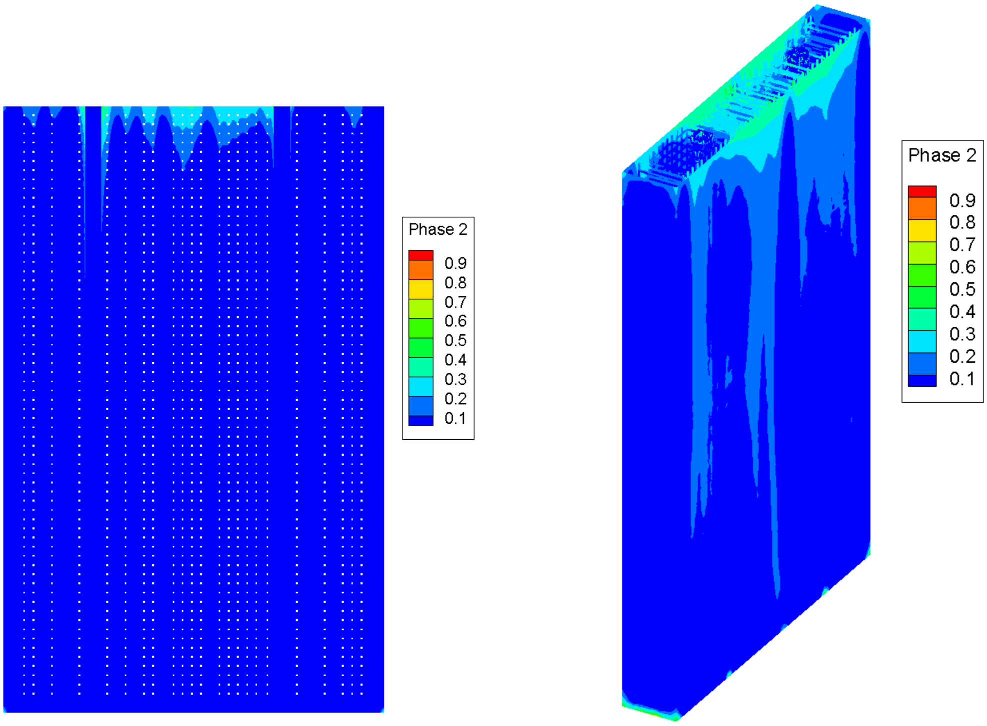

(a) Middle cross section (b) Wall surface

Fig. 2.48 Case 2: bentonite volume fraction in the wall

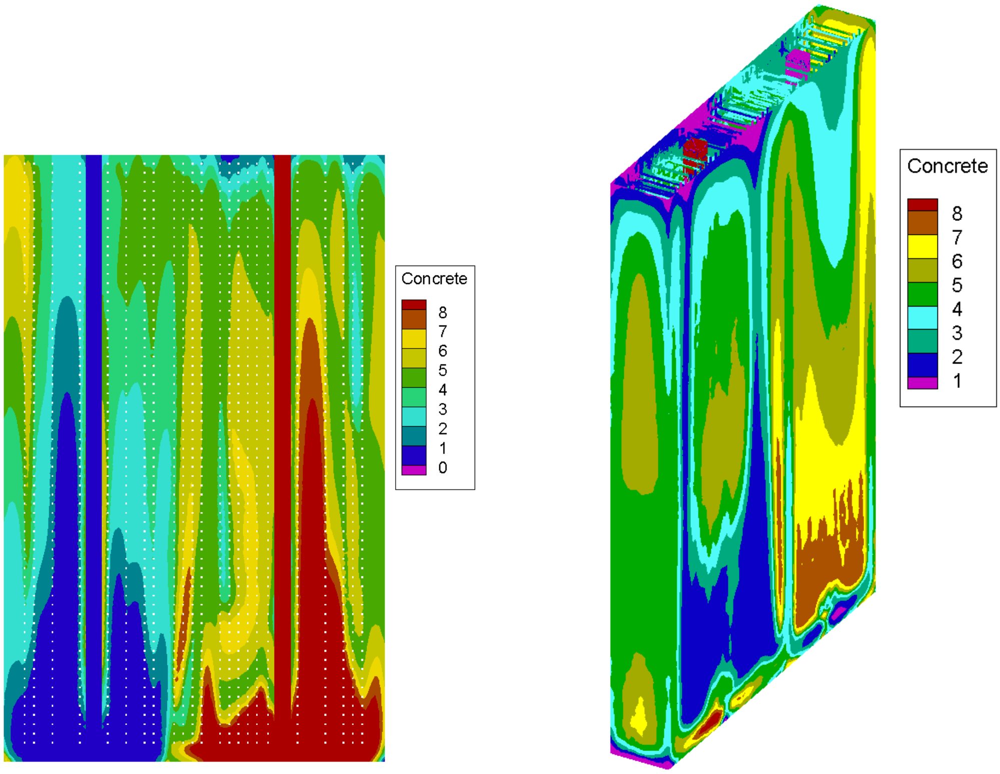

(a) Middle cross section (b) Wall surface

Fig. 2.49 Case 1: volume fraction of 9 concrete phases in the wall

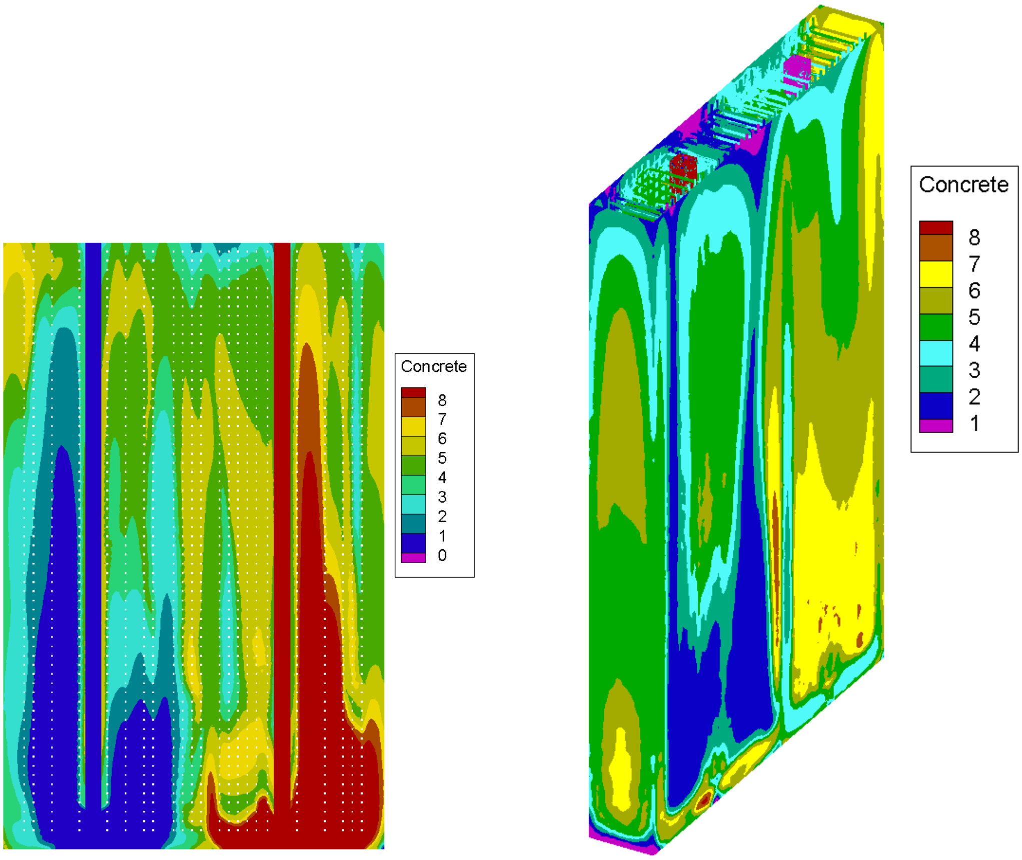

(a) Middle cross section (b) Wall surface

Fig. 2.50 Case 2: volume fraction of 9 concrete phases in the wall

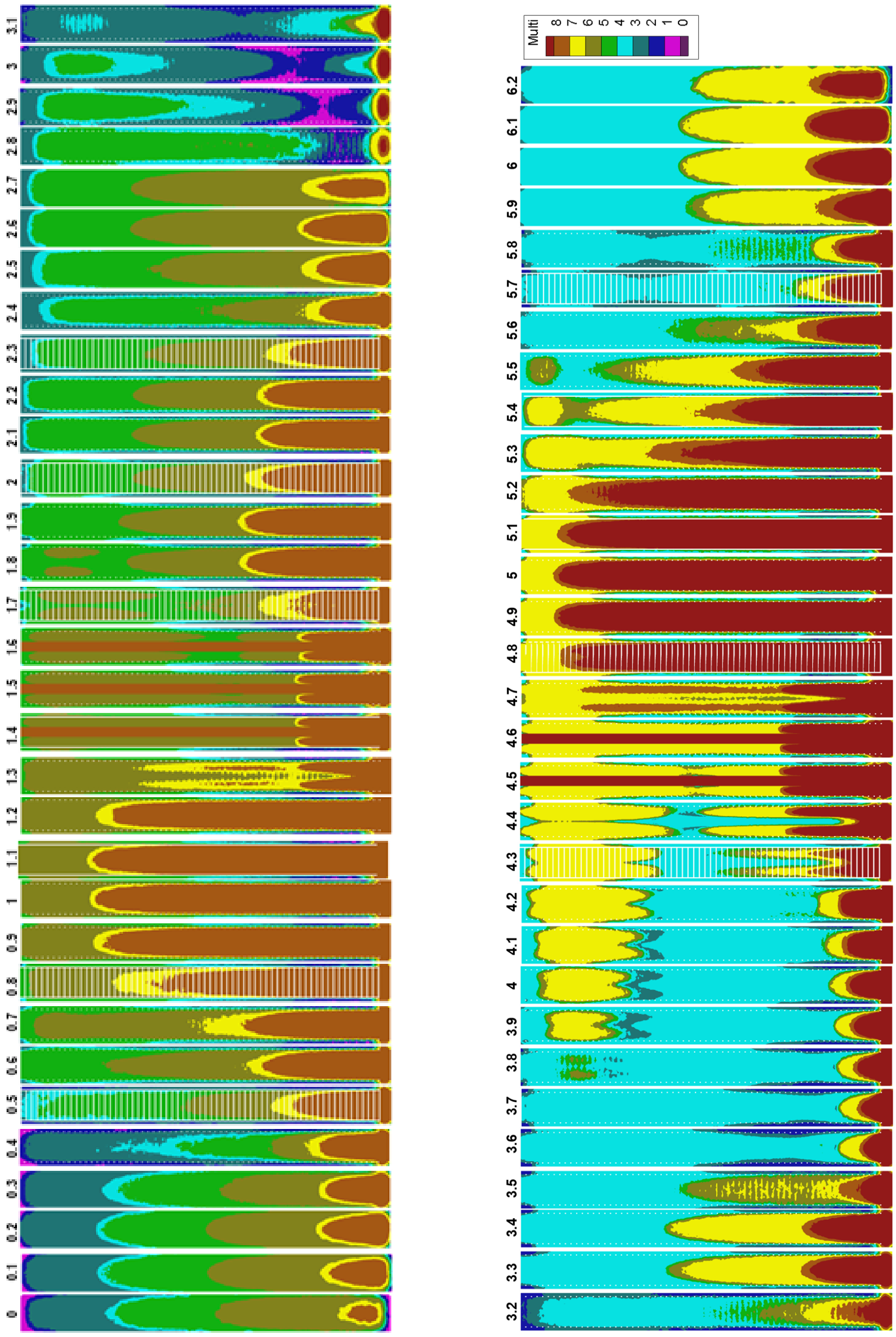

(a) Left cage (b) Right cage

Fig. 2.51 Case 1: volume fraction of 9 concrete phases in the wall

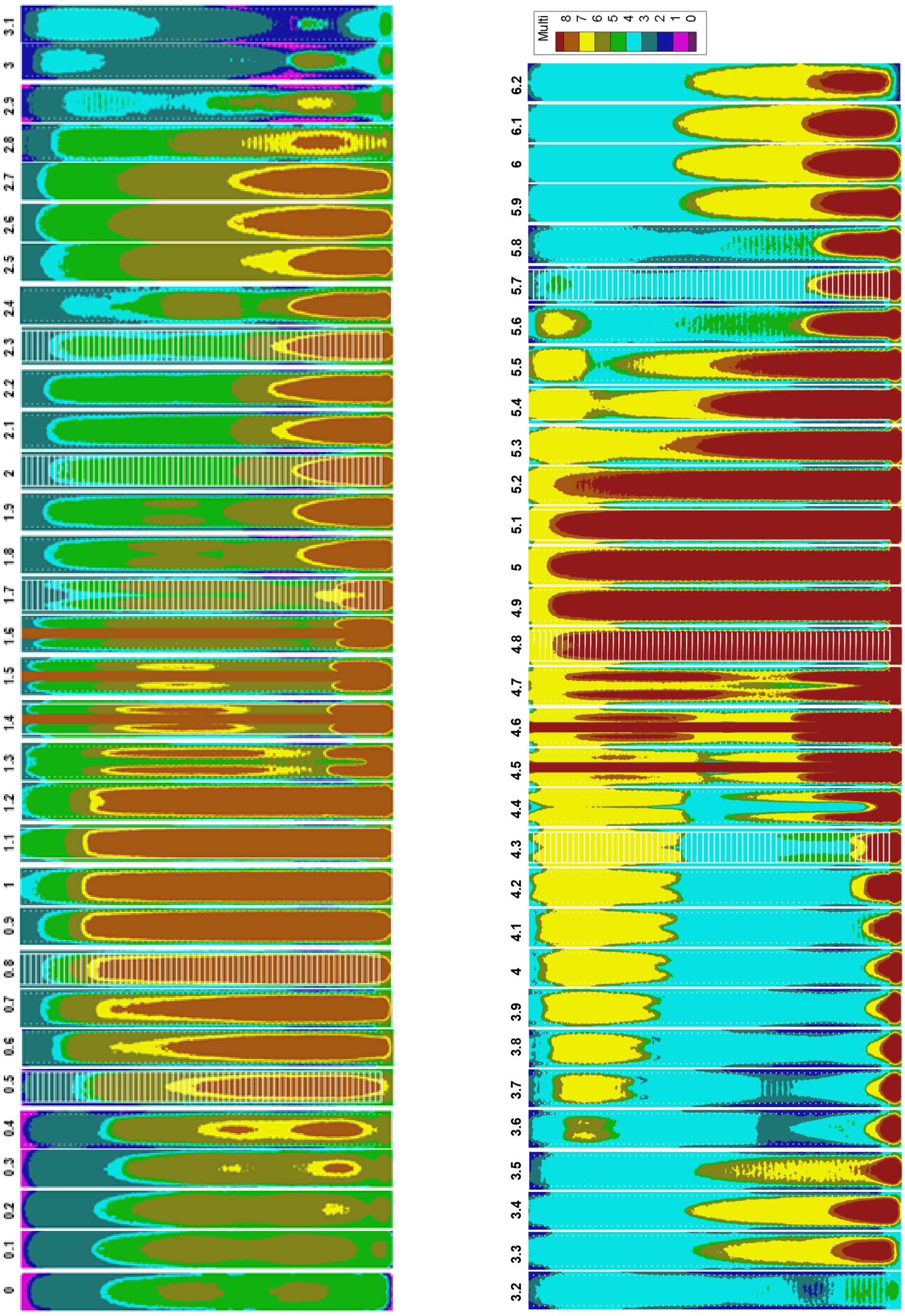

(a) Left cage (b) Right cage

Fig. 2.52 Case 2: volume fraction of 9 concrete phases in the wall

Chapter 3

Introduction to the unresolved CFD-DEM approach

3.1 Introduction

The particulate flow, which is a mixture of fluid and particles, is very common in both nature and industry. The sand storm, the sedimentation transport, bridge scour, fluidized bed, fresh concrete flow and pneumatic convey are all examples, as shown in Fig.3.1. The simulation of the particulate flow has been a popular topic for several decades, and many methods have been developed. Zhou et al. [108] divided the popular methods into two groups: the two-fluid method and the CFD-DEM method. The former group of methods regards both fluid and discrete phases as interpenetrating continuum media but requires the individual particle size to be much smaller than the cell size in the numerical method. By formulating the velocity difference between two phases [3, 97, 58], extra terms are introduced to enclose the governing equations and the dispersion of the second phase can be achieved. However, its accuracy highly depends on the equivalent fluid constitutive relation of the solid phase, which is usually difficult to obtain under this framework especially when there are several types of particles. On the contrary, in the CFD-DEM method, the motion of the solid phase is solved separately by a DEM solver, which captures the actual trajectory of every particle. The main advantage of this group of methods is that it can generate detailed local fluid-particle interaction, but the cost is the dramatically increased computation consumption.

The above general classification can be expanded with a more detailed discussion by considering the relative scale of the solid phase as shown in Fig.3.2. If both the particle size and the velocity difference are very small, the mixture of two different phases can be treated as a single fluid continuum such as the cement paste and toothpaste. But if the

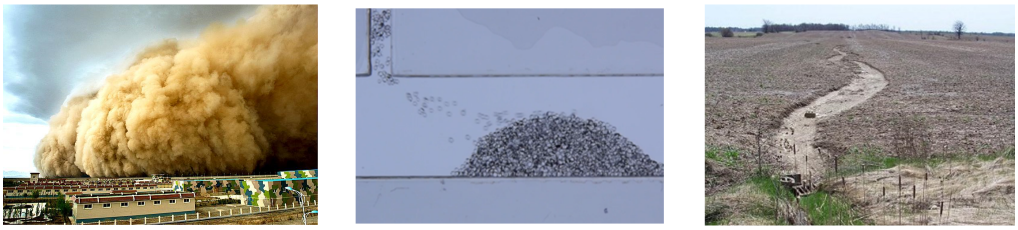

(a) Sand storm [80] (b) Sedimentation (c) Soil erosion [5]

Fig. 3.1 Example of particulate flow

velocity difference cannot be ignored, the two-fluid method is to be used. If the particle size becomes influential or local phenomenon is of interest, the unresolved CFD-DEM approach [91, 57, 47] can be used. This method uses the explicit fluid-particle interacting forces such as the drag model to realize the coupling between the fluid phase and particle phase. In this way, the coupling is called "unresolved". While, when the particle size is times larger than the cell size, the resolve CFD-DEM approach [47, 59] is preferred. It creates the projection between the large particle and the overlapped cells which could recover the fluid-particle interacting on the particle surface. In this way, the coupling force is resolved naturally in the method. At last, for a scenario where the particle is close to the cell, there is a semi-resolved CFD-DEM approach available [98, 51]. This type of method is either an extension of the unresolved approach or the combination of the unresolved and resolved approaches. In Fig.3.2, the computational cost increases from left to the right in terms of the same complexity. Coming back to the purpose of this study, the aggregate size usually varies in the range of $6 \sim 20$ *mm* for SCC, which is close to the mesh size given in Chapter 2.2. Beyond that, as the rebar varies in a similar range, the mesh size has to be close to the rebar size in the real application. In conclusion, the relative size of the aggregate may override the boundary of the medium range and the large range in Fig.3.2. Therefore, to achieve the flow simulation of SCC, the unresolved CFD-DEM is chosen as the basis of this thesis.

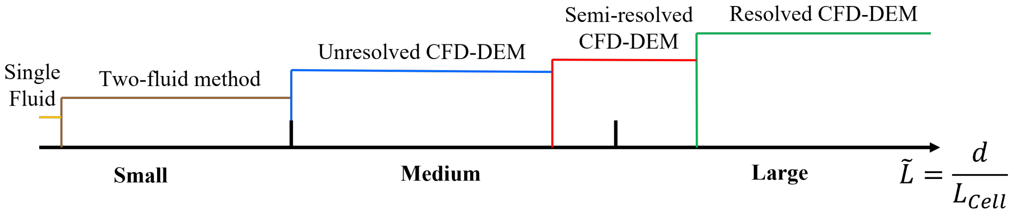

Fig. 3.2 Relative particle size and applicable model

The unresolved CFD-DEM approach was firstly proposed by Tsuji et al. [91] in 1993 to simulate the fluidized bed. Since then, it has been developing very fast in the last 3 decades as the computation power was increasing dramatically. Especially in recent 10 years, the relative publications is exploding as shown in Fig.3.3. Other than popular topic of fluidized and spouted bed [46, 67, 10, 6] in chemical industry, this method has been applied in a very wide research areas such as dense medium cyclone [17, 13], geotechnique [107, 44], pipe wearing [94], proppant transport [104, 106], debris flow [55], coal dust combustion [81] and so on. This chapter includes two parts. Firstly, the formulation of the unresolved CFD-DEM approach is introduced which includes the governing equations and coupling method. Based on it, our in-house code is developed. So in the second part, this code is validated by comparing sophisticated software such as *OpenFOAM*, *LGGGHTS* and *CFDEM*. The other extensions that are required for the concrete simulation will be explained in further chapters.

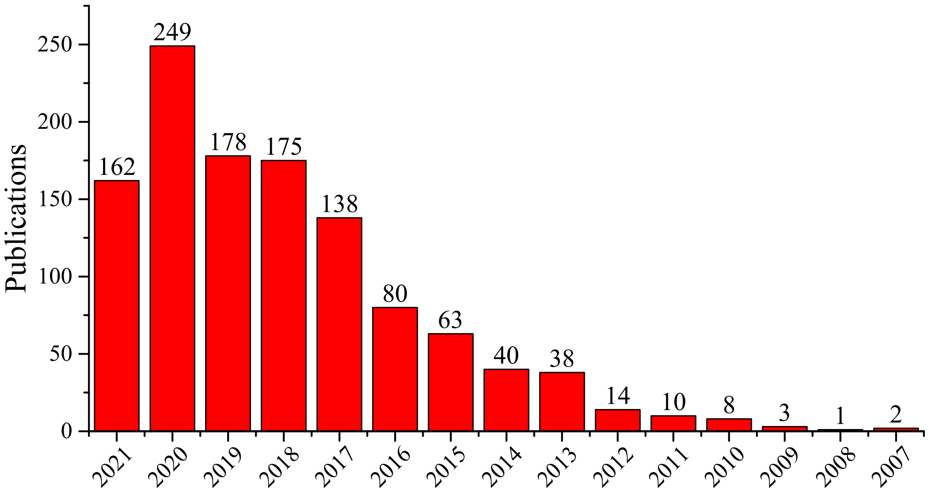

Fig. 3.3 Publications over year (from *Web of Science*)

3.2 Governing equations

3.2.1 CFD

The fresh mortar is an incompressible and highly viscous fluid and in most applications, the flow is in the regime of laminar flow. Therefore, the following volume-averaged Navier-Stokes equations are used to govern the mortar flow:

$$\frac{\partial(\alpha_f \rho_f)}{\partial t} + \nabla \cdot (\alpha_f \rho_f \boldsymbol{u}_f) = 0 \tag{3.1}$$

$$\frac{\partial(\alpha_f \rho_f \boldsymbol{u}_f)}{\partial t} + \nabla \cdot (\alpha_f \rho_f \boldsymbol{u}_f \boldsymbol{u}_f) = -\alpha_f \nabla p + \nabla \cdot (\alpha_f \boldsymbol{\tau}_f) + \alpha_f \rho_f \boldsymbol{g} - \boldsymbol{R}_{fp} - \boldsymbol{f}_{fp} \tag{3.2}$$

where α_f is volume fraction of fluid, ρ_f is the fluid density, $\boldsymbol{u}_f$ is the fluid velocity, p is the fluid pressure, $\boldsymbol{\tau}_f$ is the stress tensor of fluid phase, and $\boldsymbol{g}$ is the acceleration due to gravity. The α_f is introduced to represent the existence of a second discrete phase. It is computed by

$$\alpha_f = 1.0 - \alpha_p \tag{3.3}$$

$$\alpha_p = \frac{\sum_i V_p}{V_{cell}} \tag{3.4}$$

where α_p is the volume fraction of particles, and $\sum_i V_p$ denotes the volume occupied by particles in a CFD certain cell. The term $\boldsymbol{R}_{fp}$ denotes the momentum exchanging term due to drag force. $\boldsymbol{f}_{fp}$ is the other interacting force components, which are usually implemented explicitly. They will be explained in more detail later.

3.2.2 DEM

The DEM is a Lagrangian method, and all particles are tracked at the scale of particle size. Their motion (translational and angular) are governed by Newton's Second Law of Motion as given in Eqn.3.5 and Eqn.3.6.

$$m_p \frac{d^2}{dt^2} r_i = \boldsymbol{F}_{f,i} + F_i \tag{3.5}$$

$$I_i \frac{d}{dt} \omega_{\boldsymbol{i}} = \boldsymbol{T}_{\boldsymbol{i}} \tag{3.6}$$

where subscription i is the particle index, m_p is the mass of a particle, t is time, $\boldsymbol{r}$ is the particle position, F_f represents the sum of forces from the fluid phase such as drag and pressure-gradient forces, and $\boldsymbol{F}$ is the sum of all the other forces such as particle contact and gravity. In Eqn.3.6, I is the moment of inertia, ω is the angular velocity and the $\boldsymbol{T}$ is the total torque due to particle tangential contact forces.

The particles in the DEM model are supposed to be "soft" which allows overlap between particles during the collisions. In every time step, the forces on particles are assumed to be constants. So, by integrating over time, the trajectory of particles are solved explicitly. Based on the relative particle position, various contact models have been proposed to model the collision process. In this work, the spring-dashpot model is adopted for the spherical particles. As shown in Fig.3.4a, the overlap δ is given as:

$$\delta = \left(a_i - a_j\right) - \left(\boldsymbol{r}_i - \boldsymbol{r}_j\right) \cdot \boldsymbol{n} \tag{3.7}$$

where i and j are the two colliding particles, a is particle radius, and $\boldsymbol{n}$ is the unit vector pointing from particle j to i. The contact force is decomposed into the normal, tangential and rolling parts. The normal contact is modeled in Fig.3.4b, its magnitude F^n is given by:

$$F^n = (k\delta + \gamma v_n) \tag{3.8}$$

where k is stiffness of particle, γ is the damping coefficient and v_n is the magnitude of normal relative velocity computed by $v_n = -\boldsymbol{v}_{ij} \cdot \boldsymbol{n} = -\left(\boldsymbol{v}_i - \boldsymbol{v}_j\right) \cdot \boldsymbol{n}$. The tangential force involves the relative tangential velocity $\boldsymbol{v}_t = \boldsymbol{v}_{ij} - \left(\boldsymbol{v}_{ij} \cdot \boldsymbol{n}\right) \boldsymbol{n}$. As modelled in Fig.3.4c, and its magnitude F_t is given by:

$$F^t = min\{\left| k_t \int_{t_{c,0}}^{t} \boldsymbol{v}_t dt \right|, \mu f^n\} \tag{3.9}$$

where k_t is the tangential spring stiffness, γ_t is the tangential damping coefficient, μ is the coefficient of friction, $t_{c,0}$ is the time particles came into contact, and the t is time contact remains. The rolling contact is modelled in a similar way as the tangential. The relative rolling velocity $\boldsymbol{v}_r$ is used instead:

$$\boldsymbol{v}_r = -a'_{ij} \left(\boldsymbol{n} \times \boldsymbol{\omega}_i - \boldsymbol{n} \times \boldsymbol{\omega}_j\right) \tag{3.10}$$

where $a'_{ij} = a'_i a'_j / \left(a'_i + a'_j\right)$ and $a'_\alpha = a_\alpha - \delta/2$, for $\alpha = i, j$. Parameters μ, k_t and γ_t are replaced by μ_r, k_r and γ_r.

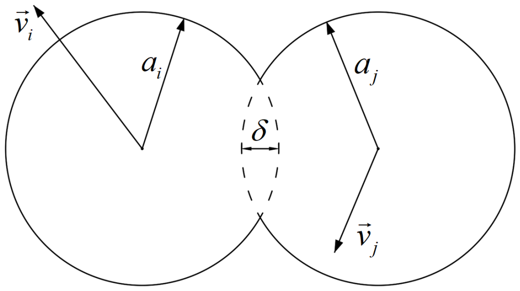

(a) colliding particles

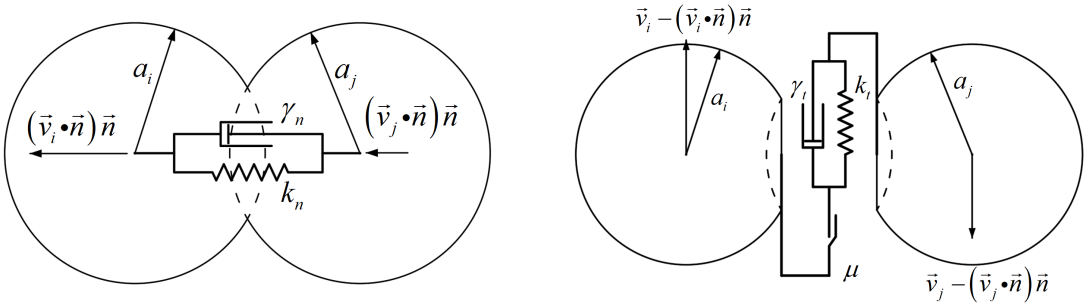

(b) Normal contact model

(c) Tangential contact model

Fig. 3.4 DEM contact model: spring-dashpot

3.3 CFD-DEM coupling

As an Eulerian-Lagrangian approach, the unresolved CFD-DEM technique achieves the coupling between a continuous and a discrete field. In DEM, all particle properties are point-based and assigned to the centre of every particle. While, in CFD, all properties are continuous fields. Because all the expressions of various fluid-particle forces return centre-based values, they can be used differently in DEM. When applying them in CFD, the forces should be mapped into a field. The former can be regarded as the integration of the latter in a certain domain. Except for the forces, the particle volume also should be treated in the same manner, which gives the volume fraction α_f and α_p in the CFD domain. It is a key parameter in determining fluid-particle forces and in the CFD governing equations. The exchanged information is summarized in Figure 3.6. The mapping scheme between point-based value and continuous field will be discussed in Section 3.3.2.

The computation of the exchanged forces requires information from both the DEM side and CFD side, and the details will be presented in Section 3.3.1. The coupling scheme between CFD and DEM solvers can be concluded in 7 steps:

(1) When the coupling starts, the particle volume is mapped to the CFD domain to get the volume fraction field;

(2) Relative fluid variables at the position of every particle centre are interpolated such as fluid velocity, pressure gradient and volume fraction, which will be passed to DEM;

(3) The hydraulic forces at the position of every particle centre are computed according to the interpolated fluid variables and corresponding particle variables;

(4) The hydraulic forces are mapped to the CFD domain;

(5) The DEM solver updates the state of every particle, and the CFD solver updates the fluid field according to their stepping schemes;

(6) The CFD and DEM solvers are coupling at a fixed frequency, and the steps (1) to (6) will be repeated every time.

The stepping scheme of CFD and DEM can be seen in Figure 3.5. The CFD and DEM have decoupled stepping schemes, but are coupled at a fixed frequency. Because the coupled CFD-DEM approach is time-consuming, it is always desired to have a larger time step in either solver if possible. Especially, in the scenarios where the unresolved approach is desired, the CFD side often has a higher cost. To address this issue, the drag force term in CFD will be treated implicitly, and the detail will be presented in Section 3.3.1.

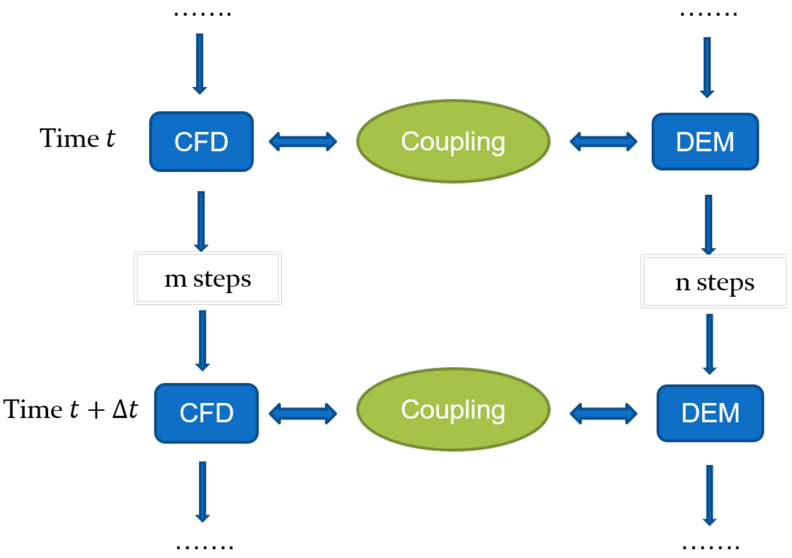

Fig. 3.5 Stepping scheme

3.3.1 Fluid-particle forces and implementation

The fluid-particle force can be decomposed into several components: the drag force due to relative velocity, the pressure-gradient force arising from the fluid pressure gradient, the lift forces (Saffman and Magnus forces) due to particle rotation, the virtual mass force relating

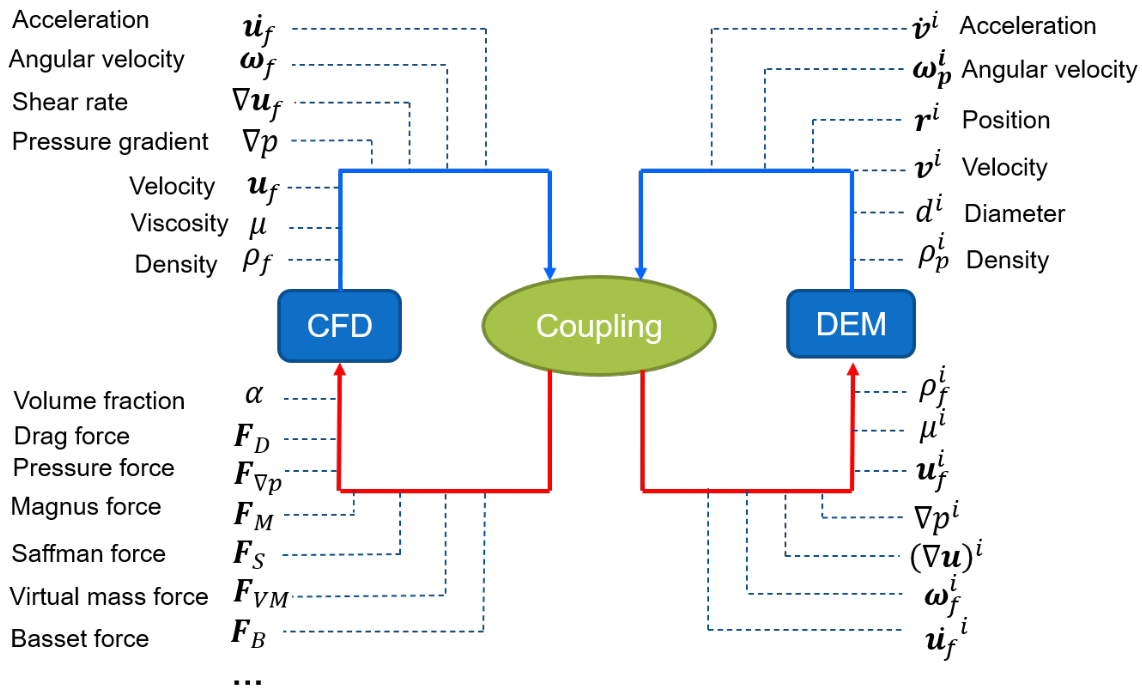

Fig. 3.6 Exchanged information in coupling

the acceleration of surrounding fluid and the Basset force from the lagging boundary layer development with the acceleration of relative velocity. The expressions for the above forces acting on a sphere are listed in Table 3.1. The drag force and pressure-gradient force are essential in all applications while the others can be neglected in many cases as they are usually much smaller. Theoretically, all the forces can be implemented explicitly in both CFD and DEM. However, to enable a larger time step in CFD, the implicit scheme and semi-implicit scheme are used for pressure gradient force and drag force respectively.

Taking the pressure-gradient force as an example, it can be obtained by Eqn. 3.11. It's a simple function of the fluid pressure gradient. However, to apply the point-based force, it should be transferred into a continuous field which will be explained in the next Section 3.3.2. Theoretically, the term applied in CFD should be the volumetric derivative of the pressure-gradient force, which is given in Eqn. 3.12. Referring to governing equation Eqn. 3.2, this force of has been considered in the term $-\alpha_f \nabla p$, because it's assumed that the CFD and DEM share the same pressure. Thus the pressure-gradient force is implemented implicitly. The drag force term is given by term $\boldsymbol{R}_{fp}$, and other forces are included in $\boldsymbol{f}_{fp}$. As the latter uses an explicit scheme that is easy to implement, the drag force is introduced with specific attention.

$$\mathbf{F}_{\nabla p,i} = -\nabla p V_i \tag{3.11}$$

$$\frac{d\mathbf{F}_{\nabla p}}{dV} = -\alpha_p \nabla p \tag{3.12}$$

The drag force on a spherical particle i can be given in the format:

$$\boldsymbol{F}_{d,i} = \frac{V_i \beta}{\alpha_p}(\boldsymbol{u}_f - \boldsymbol{v}_i) \tag{3.13}$$

where $\boldsymbol{F}_{d,i}$ is the drag force which is a part of $\boldsymbol{F}_f$, V_i is the volume of particle i, $\boldsymbol{u_f}$ is the fluid velocity, $\boldsymbol{v_i}$ the velocity of particle i, α_p $(= 1-\alpha_f)$ is the volume fraction of particles in the surrounding space of particle i and β is the inter-phase momentum transfer coefficient due to drag. The drag force has been studied extensively, and many popular models are in use such as the Ergun and Yu model [33, 99], the Di Felice model, the Koch and Hill model [48], the Beetstra model [7] and so on, all conforming to the same format as Eqn.3.13. The expressions of β for these drag models can be found in Table 3.1.

The implementation of drag force requires a lot of parameters. α_f and $|\boldsymbol{u}_f - \boldsymbol{v}_i|$ (also can be represented by Re_p) are the two variables, and the rest are constants. The influence of the two variables on drag force magnitude is presented in Fig.3.7, and the performance of different models is compared at the same time. It's observed that the drag force given by every model increases monotonously when Re_p or α_f grows larger. What's more, the increasing rate of drag force shows the trend too. However, there are significant gaps between every two curves.

For CFD, however, the implementation of drag force terms in Eqn.3.2 has to involve the CFD mesh. For a certain cell, $\boldsymbol{R}_{fp}$ is volume-averaged from the total drag force of all particles accommodating in the same cell:

$$\boldsymbol{R}_{fp} = \sum_i \boldsymbol{F}_{d,i} / V_{cell} \tag{3.14}$$

where V_{cell} is the FVM cell volume. Eqn.3.14 is an explicit expression for $\boldsymbol{R}_{fp}$. To improve the convergence, it can be rewritten in an implicit form by involving the averaged particle velocity $\langle \boldsymbol{v} \rangle$:

$$\boldsymbol{R}_{fp} = K_{fp}(\boldsymbol{u_f} - \langle \boldsymbol{v} \rangle) \tag{3.15}$$

where K_{fp} is the volume-averaged coefficient of total drag force from all particles in the cell, which has a similar meaning with k_d. It's usually implemented as:

$$K_{fp} = \frac{\left|\sum_i \boldsymbol{F}_{d,i}\right|}{V_{cell}\left|\boldsymbol{u_f} - \langle \boldsymbol{v} \rangle\right|} \tag{3.16}$$

In each time step, $K_{f,p}$ and $\langle \boldsymbol{v} \rangle$ are assumed to be constant, and $\boldsymbol{u}_f$ behaves as an implicit part in CFD solver, which means the drag force term $\boldsymbol{R}_{fp}$ is proportional to the fluid velocity $\boldsymbol{u}_f$. Thus, by assuming a part of the drag model to be constant, the drag force is implemented semi-implicitly in CFD.

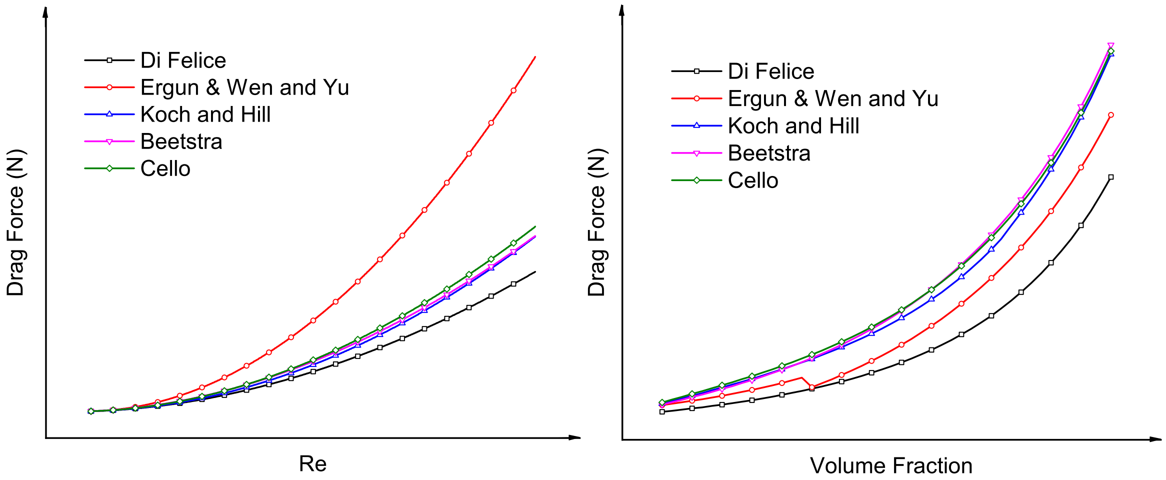

(a) Drag force VS Reynolds number (b) Drag force VS volume fraction of particle

Fig. 3.7 Influence of parameters on drag force

Table 3.1 Summary of Particle-fluid forces

Forces	Expressions
Drag force	
Di Felice [29]	$\beta = \frac{3}{4} C_d \alpha_p \frac{\rho_f}{d} \lvert \boldsymbol{u}_f - \boldsymbol{v} \rvert \alpha_f^{2-\chi}$
	$C_d = \left(0.63 + 4.8 Re^{-0.5}\right)^2$
	$\chi = 3.7 - 0.65 e^{-\frac{1}{2}(1.5 - \log_{10} Re)^2}$
	$Re = \frac{\alpha_f \rho_f \boldsymbol{u}_f d}{\mu}$
Ergun and Yu [33, 99]	$\beta = \begin{cases} 150 \frac{\alpha_p^2 \mu_f}{\alpha_f d^2} + 1.75 \frac{\alpha_p \rho_f}{d} \lvert \boldsymbol{u}_f - \boldsymbol{v} \rvert & \text{if} \alpha_f \leq 0.8 \\ \frac{3}{4} C_d \alpha_p \frac{\rho_f}{d} \alpha_f^{-1.65} \lvert \boldsymbol{u}_f - \boldsymbol{v} \rvert & \text{if} \alpha_f > 0.8 \end{cases}$
	$C_d = \begin{cases} \frac{24}{Re}\left(1 + 0.15 Re^{0.687}\right) & \text{if } Re < 1000 \\ 0.44 & \text{if } Re \geqslant 1000 \end{cases}$
Koch and Hill [48]	$\beta = \frac{18 \mu_f \alpha_f^2 \alpha_p}{d^2} \left[F_0(\alpha_p) + \frac{1}{2} F_3(\alpha_p) Re\right]$
	$F_0(\alpha_p) = \begin{cases} \frac{1 + 3\sqrt{\frac{\alpha_p}{2}} + \frac{135}{64} \alpha_p \ln(\alpha_p) + 16.14 \alpha_p}{1 + 0.681 \alpha_p - 8.48 \alpha_p^2 + 8.16 \alpha_p^3} & \text{if } \alpha_p < 0.4 \\ \frac{10 \alpha_p}{\alpha_f^3} & \text{if } \alpha_p \geqslant 0.4 \end{cases}$
	$F_3(\alpha_p) = 0.0673 + 0.212 \alpha_p + \frac{0.0232}{\alpha_f^5}$
Beetstra [7]	$\beta = 18 \frac{\mu_f \alpha_f \alpha_p \hat{f}^D}{d_i^2}$
	$\hat{f}^D = \left(\frac{180 \alpha_p}{18 \alpha_f^2}\right) + \alpha_f^2 \left(1 + 1.5\sqrt{\alpha_p}\right) + \left(\frac{0.413}{24 \alpha_f^2}\right) \left(\frac{\alpha_f^{-1} + 3 \alpha_p \alpha_f + 8.4 Re^{-0.343}}{1 + 10^{3\alpha_p} Re^{-(1+4\alpha_p)/2}}\right) Re$
Pressure gradient force [3]	$\boldsymbol{F}_{\nabla p, i} = -\nabla p V_i$
Virtual mass force [66]	$\boldsymbol{F}_{vm} = C_{vm} \rho_f V_p (\dot{\boldsymbol{u}}_f - \dot{\boldsymbol{v}})/2$
	$C_{vm} = 2.1 - \frac{0.132}{\left(0.12 + A_c^2\right)}$
	$A_c = (\boldsymbol{u}_f - \boldsymbol{v})^2 / \left(\mathrm{d}_p \frac{\mathrm{d}(\boldsymbol{u}_f - \mathbf{v})}{\mathrm{d}t}\right)$
Magnus force [78]	$\boldsymbol{F}_{\text{Mag}} = \frac{\pi}{8} d_p^2 \rho_f \left[\left(\boldsymbol{\omega}_f - \boldsymbol{\omega}_d\right) \times (\boldsymbol{u} - \boldsymbol{v})\right]$
	$\boldsymbol{\omega}_f = \frac{1}{2} \nabla \times \boldsymbol{u}_f$
Saffman force[79]	$\boldsymbol{F}_{\text{Saff}} = 1.615 d_p^2 \left(\mu \rho_f\right)^{1/2} C_s \frac{\left[(\boldsymbol{u}_f - \boldsymbol{v}) \times \boldsymbol{\omega}_c\right]}{\lvert \boldsymbol{\omega}_c \rvert^{0.5}}$
	$\boldsymbol{\omega}_c = \nabla \times \boldsymbol{u}_f$
Basset force [73]	$\boldsymbol{F}_{\text{Basset}} = \frac{3}{2} d_p^2 \sqrt{\pi \rho_f \mu} \left[\int_0^t \frac{(\dot{\boldsymbol{u}} - \dot{\boldsymbol{v}})}{\sqrt{t - t'}} \mathrm{d}t' + \frac{(\boldsymbol{u} - \boldsymbol{v})_0}{\sqrt{t}}\right]$
Torque [78]	$\boldsymbol{T} = 8 \pi \mu r^3 \left(\boldsymbol{\omega}_f - \boldsymbol{\omega}_p\right)$

3.3.2 Mapping of particle volume and drag force

The coupling scheme is the key part of the unresolved CFD-DEM approach. In DEM, all variables including the exchanged are discrete values based on the centre points of particles. In CFD, the situation is more complicated as the variables are continuous fields. So, it is the volumetric derivatives of the variables that are passed from DEM to CFD including the particle volume and drag force. In this study, the CFD is solved by FVM which is mesh-based, so the issue becomes the mapping between CFD mesh and DEM particles. A simple way to determine the particle volume fraction of a cell is, to sum the volume of all particles up whose centre is accommodating in the current cell, which is called the *particle centred* method. This method has major disadvantages and only applies when the cell size is several times larger than the particle size. The detailed discussion will be given in Chapter 4.

The mapping of all the other variables uses the same method to keep consistency. For example, if the *divided* method is used, every fluid-particle force should be divided into the same number of parts, which should be assigned to the same cell as the volume of sub-parts. Thus, the mapping procedures in the CFD-DEM coupling can be described by the following 7 steps:

(1) Establish the spatial relationship between DEM and CFD domains.

(2) According to the relation map, the particle volume in every cell is computed to obtain the volume fraction α_f.

(3) According to the map, the fluid variables of a cell (such as α_f, ρ_f, μ_f, $\boldsymbol{u}_f$, ∇p, et al.), is assigned to the accommodating particles or sub-parts. For the latter, an averaged value should be used for a whole particle.

(4) Compute the fluid-particle forces ($\boldsymbol{F}_d$, $\boldsymbol{F}_{\nabla p}$, et al.) using the variables of both CFD and DEM.

(5) Mapping the forces to cells according to the relation map.

(6) The averaged particle velocity $\langle \boldsymbol{v} \rangle$ in a cell is computed according to the relation map.

(7) Compute the coefficient $K_{fp,i}$ of all cells.

3.4 Validation

Based on the above knowledge, our in-house code was developed to simulate the coupled fluid-particle flow problem. It contains the 3 main modules: the CFD part, the DEM part and the coupling part. They will be validated step by step by comparing with sophisticated software. The *OpenFOAM*, *LGGGHTS* and *CFDEM* will be used for CFD, DEM, and coupled CFD-DEM validations respectively. In addition, it should be mentioned that the popular open-source software *CFDEM* is also based on the coupling of *OpenFOAM* and *LGGGHTS*.

3.4.1 CFD solver

In the CFD validation, two cases will be carried out for different purposes. Firstly, the case lid-driven cavity is used to validate the CFD solver. Secondly, a bent pipe is used to validate the implementation of the Bingham model.

Lid driven cavity

Lid driven cavity is a classic benchmark to validate the CFD solver. This case is designed as shown in Fig. 3.8, whose height (Y) is 0.1 m, width (X) is 0.1 m and depth (Z) is 0.01 m. The top boundary moves at a constant velocity of 1 m/s towards the right side while the back and front walls are slip walls. For the rest, they are all non-slip walls. The fluid density is 1000 kg/m^3 and its viscosity is 10 $Pa \cdot s$. At the first step, the mesh convergence was carried out by the OpenFOAM to choose the appropriate mesh for this study. As shown in Fig.3.9, 5 different meshes were used in total. Every case has the same partitions along both X and Y directions but shares the same 5 partitions along the Z direction. For example, "35X25" in the figure means that there are 35 divisions in each direction of X and Y, so the total number of elements is 6125. In the figure, the curves plot the velocity magnitude at steady state on the line where X equals to 0.05 m and Z is 0.005 m. It is seen that the curves "20X20", "25X25", "30X30", "35X35" are close to each other but the curve "15X15" is quite distant from them, which demonstrate that the case "35X35" could be used to approximate the converged result. So, the mesh of this case was used for further study as shown in Figure.3.8.

For comparison, the case study of validation was run by both *OpenFOAM* and our in-house code using the same configuration. The contour plots of velocity magnitude at the steady state are taken from the middle of depth direction and compared in Fig. 3.10, which are almost visually identical. Further, referring to Figure 3.9, the velocity magnitude at the same line is compared for the two results as shown in Fig 3.11. Again,s perfect match is observed between OpenFOAM and our in-house code, which proves the validation of the CFD solver of our in-house code.

Bent pipe

As the cement-based materials including concrete are typical Bingham fluid, the implementation of this fluid needs to be validated. As given in Fig. 1.2, the Bingham model is composed of two parts: the vertical part when shear stress is below yield stress and the shear rate is 0; an oblique part which is for a non-zero shear rate. This model can't be used for implementation directly, because the shear rate can't be determined directly by shear rate when the latter is 0. To avoid such numerical issues, the vertical part can be approximated by another oblique

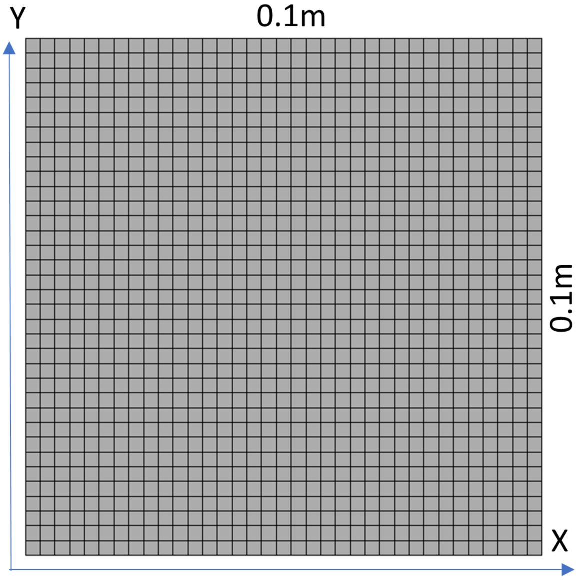

Fig. 3.8 Geometry and dimension of lid driven cavity

segment as long as its slope is large enough. Thus, the implementation of the Bingham model can be expressed in the form of apparent viscosity as given in Eqn. 3.17,

$$\tilde{\mu} = \begin{cases} \tau_0/\dot{\gamma}_c, & \gamma \le \dot{\gamma}_c \\ \tau_0/\gamma + \mu, & \gamma > \dot{\gamma}_c \end{cases} \tag{3.17}$$

where $\widetilde{\mu}$ is the fluid apparent viscosity. This model will be further discussed in Chapter 5.5.

To validate the above implementation, the bent pipe case (Fig. 3.12) is designed and run by both in-house code and *OpenFOAM*. The pipe has a circular section and the diameter is 0.4 m. The length of the two linear parts are both 1 m, and they are connected by a 90° bent part. A Bingham fluid is flowing inside the pipe from the bottom left side at a fixed velocity 0.01 m/s and flows out from the top right boundary where the pressure is set to be 0. The surface of the pipe is set to be a non-slip wall. The fluid viscosity is 100 $Pa \cdot s$, yield stress is 80 Pa and density is 2400 kg/m^3. The simulation at steady state are given in Fig. 3.13 and 3.14. The former shows the pressure field on the surface of the pipe and the latter gives the velocity field at the middle cross-section. The high similarity between the results of in-house code and the *OpenFOAM* strongly approve the validation of the Bingham fluid implementation.

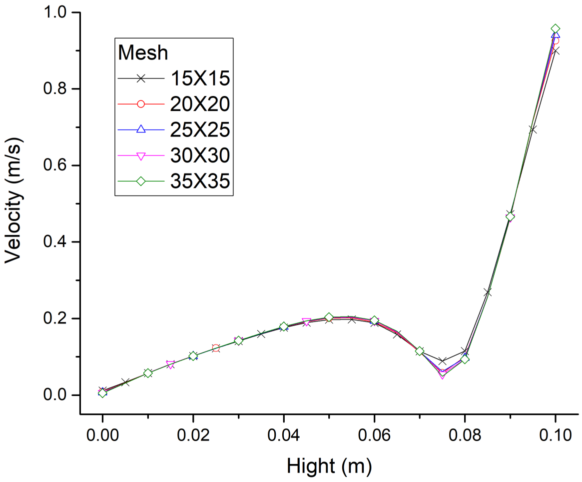

Fig. 3.9 Mesh convergence by OpenFOAM

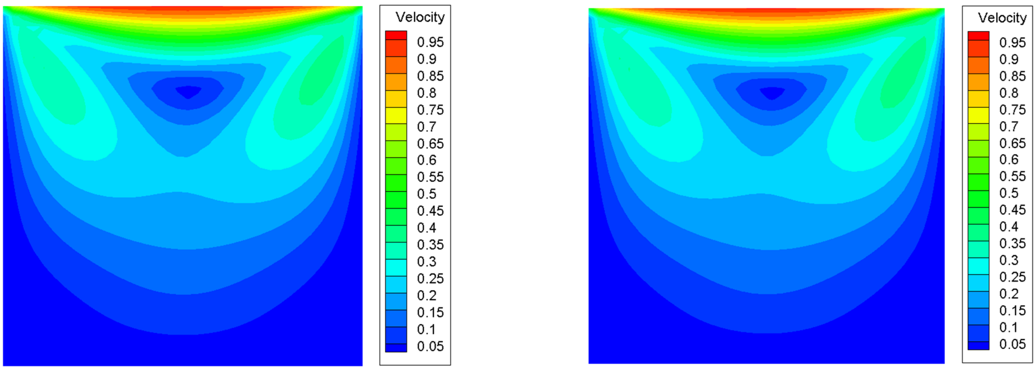

(a) In-house code (b) *OpenFOAM*

Fig. 3.10 Contour plot of velocity magnitude

3.4.2 DEM solver

To validate the DEM solver, a slope failure case is designed as shown in Fig.3.15. The width, height and depth of the large grey container are 0.5 m, 0.6 m and 0.1 m respectively. Initially, 4774 particles were packed by gravity in a tall column whose width is 0.1 m. The particle diameter is 0.01 m, and density is 2500 kg/m^3. The Hertz model is used for the particle collision, and the parameters are given in Table 3.2. When the simulation started, the particles were released from the right side and the slope failure phenomenon was observed due to the gravity, whose value is 9.81 m/s^2 pointing downwards. This cases was run by both the *LGGGHTS* and in-house code, and their comparison is presented in Fig.3.16. In total, 7 profiles of particle pile at different instances are compared including 0.1 s, 0.2 s, 0.3 s, 0.4 s, 0.5 s, 0.6 s and 0.7 s. The pictures with grey particles are from *LGGGHTS* and the others

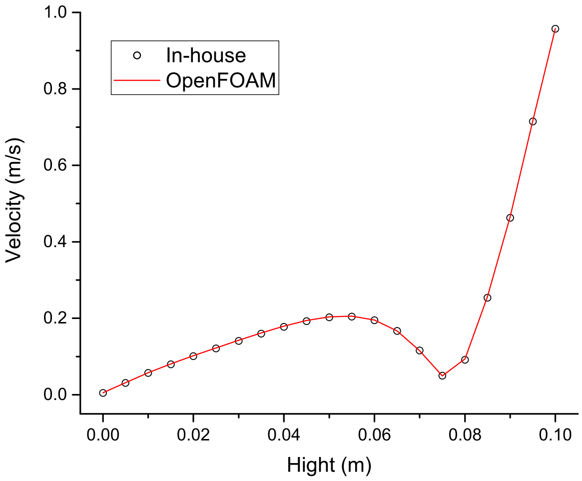

Fig. 3.11 Comparison: velocity at the middle section

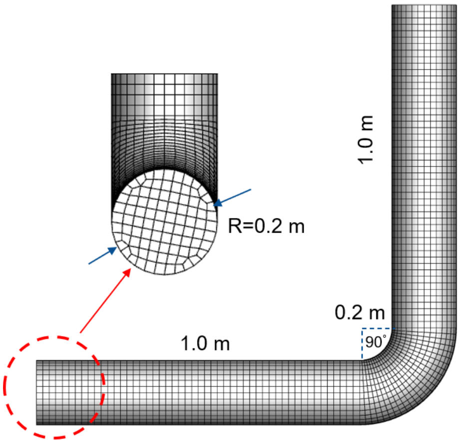

Fig. 3.12 Geometry and dimension of lid driven cavity

with yellow particles are from in-house code. It can be observed that every pair of pictures from the same time shows great similarity, which indicates our in-house DEM solver is valid.

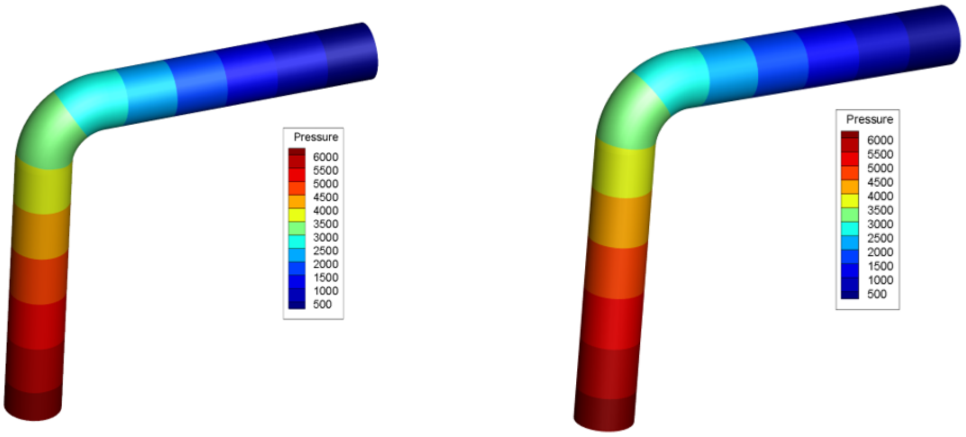

(a) In-house code

(b) *OpenFOAM*

Fig. 3.13 Contour plot of pressure on the surface of bent pipe

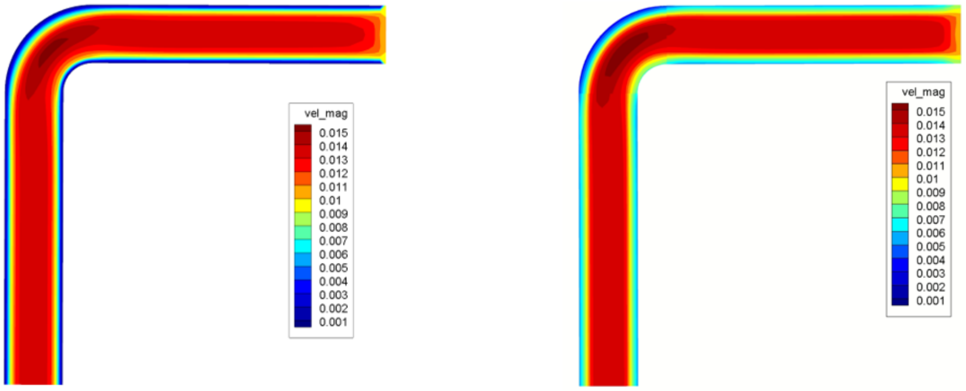

(a) In-house code

(b) *OpenFOAM*

Fig. 3.14 Contour plot of velocity magnitude in the middle section of bent pipe

Table 3.2 Parameters of contact model for case slope failure

Parameters	**Value**
Density	$2500\ kg/m^3$
Diamter	$0.01\ m$
Young's Modulus	$5.0 \times 10^6\ Pa$
Restitution Coefficient	0.7
Friction Coefficient	0.5
Poisson's Ratio	0.49
Gravity	$9.81\ m/s^2$

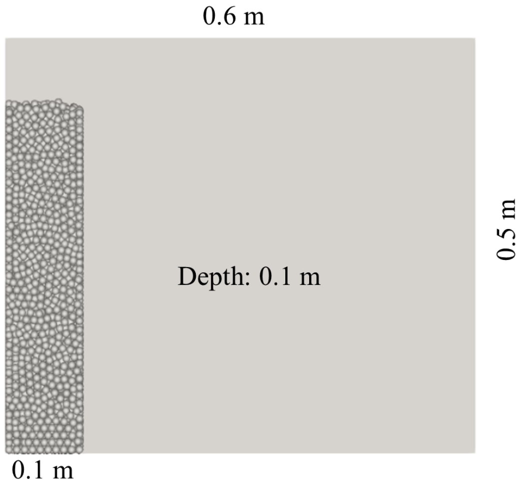

Fig. 3.15 Initial letup of the slope

3.4.3 CFD-DEM coupling

One particle case

The validation of CFD and DEM coupling starts from a simple case. It is about one particle moving in a steady flow in a bent pipe. However, as this work is also a key part of Chapter 5.4.2, this work will be presented in that chapter to make its content more compacted. The analysis shows that our in-house code generates exactly the same result with the *OpenFOAM*, which demonstrates the validation of our code.

A large amount of particles

To validate the coupling between CFD and DEM in our in-house code, the slope case used in DEM validation will be followed. The geometry of the domain and the particle configuration will be the same as shown in Fig.3.15 and Table 3.2. On the CFD side, the whole domain is filled with the fluid, whose density is 1000 kg/m^3 and viscosity is 0.1 $Pa \cdot s$. Its cell size is 0.01 m as shown in Fig.3.17. Initially, in the whole domain, the fluid and particles are at rest, and the boundaries are all walls. As a comparison, this case was run by both our in-house code and the *CFDEM*. And, both of them used the *DPVM* for the volume fraction computation. For the detail of this method, please refer to Chapter 4.3.2. The comparison of the *OpenFOAM* and in-house code is given in the Fig.3.18. In total, 2 s was simulated and the pile stopped at the end. Comparing the corresponding images one by one, we can find that the profiles of the particle piles at the same moment in the two cases are very similar. But a bit of delay is observed in the result of the in-house code. It could come from the

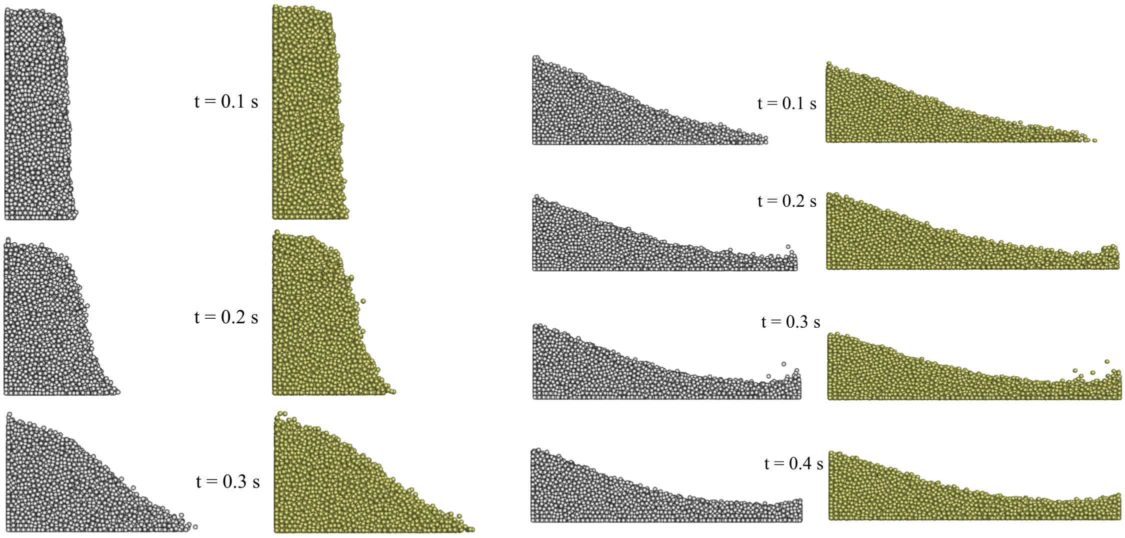

(a) Time 0.1 s to 0.3 s

(b) Time 0.4 s to 0.7 s

Fig. 3.16 Profile comparison between *LGGGHTS* (left column) and in-house code (right column)

CFD part, the coupling scheme or both. Nevertheless, this result is sufficient to prove the validation of the coupling implementation of our in-house code.

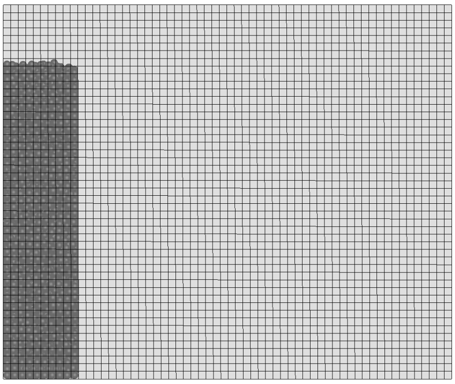

Fig. 3.17 Mesh of the slope domain

3.5 Conclusions

The unresolved CFD-DEM approach is a powerful numerical method to study the fluid and solid particulate flow. It provides a result with great quantitative details including velocity, pressure, particle position, volume fraction, forces and so on. These variables are difficult to

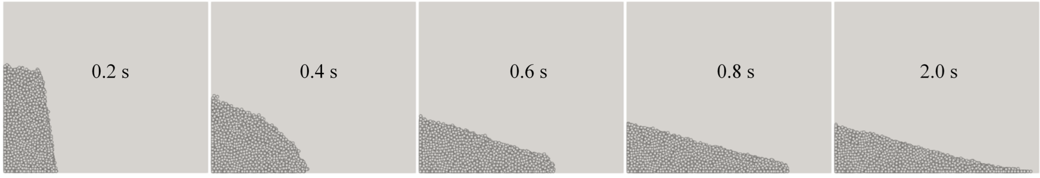

(a) *OpenFOAM*

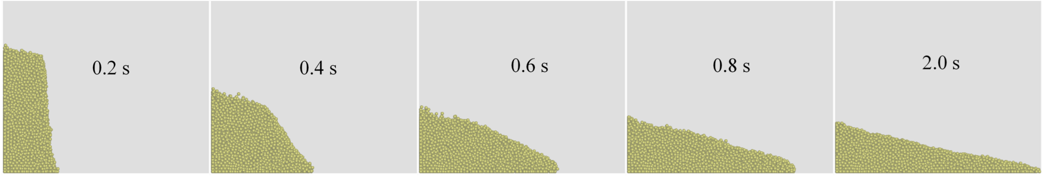

(b) In-house code

Fig. 3.18 Result comparison of slope failure in fluid: *OpenFOAM* VS in-house code

track in the experiment due to either expensive costs or limitations on monitoring techniques. So, this approach allows us to investigate the complex particulate flow with great advantages. For this reason, it was chosen as the numerical technique to study the concrete flow.

In this chapter, the formulation and implementation of the unresolved CFD-DEM approach are introduced in detail including the governing equations of both CFD and DEM, the coupling scheme, the field mapping and so on. According to the theory, an in-house CFD-DEM code was developed by our group for further work. The validation of this code was done in 3 steps by comparing it with different sophisticated software. The CFD solver was validated by *OpenFOAM*, the DEM solver was compared with *LIGGGHTS* and the coupled CFD-DEM was compared with *CFDEM*. For the first one, two cases were designed for different purposes. The lid-driven cavity was used to prove the CFD solver provides an accurate fluid result, and the bent pipe case was run to validate the implementation of the Bingham model. For the DEM solver, the slope failure case was used. At last, for the validation of the coupled CFD-DEM, the same slope failure case was used but the domain was filled with fluid. All the results of the above 3 steps showed that the CFD, DEM and the couple CFD-DEM generated the same result as the sophisticated software, which means our in-house code is validated. Since then, further work will be carried on based on this code to achieve the simulation of the fresh concrete.

Chapter 4

VOF-DEM model and coupling strategy

4.1 Introduction

Chapter 3 has introduced the framework of CFD and DEM coupling between one single fluid phase and one discrete phase. Obviously, that is not enough to realize the modelling of SCC flow. The difficulty lies in 5 aspects:

(1) The concrete flow under gravity belongs to the free surface flow and a multiphase model is necessary to establish a three-phase system: mortar, aggregate and air.

(2) On the interface of air and mortar, material properties differ greatly on its sides. This discontinuity issue brings great concern to the mapping between CFD and DEM.

(3) In the mapping, the particle volume should be conserved which in turn promises the fluid volume conservation.

(4) The size of aggregate varies in a quite large range like $6 \sim 20$ *mm*. So, the mapping scheme for the particle volume should be insensitive to its size.

(5) In the real application, a uniform structured mesh is not always promised such as the meshes of slump flow test and V funnel test given in Fig. 2.5 and 2.6 respectively. The cell size varies in a range of $5 \sim 40$ *mm*. So, the mapping scheme should be able to handle any random mesh type such as mesh with varied size over the domain or unstructured mesh.

For the 1^{st} factor, the VOF method is to be introduced to solve the two-phase flow in the CFD domain. So, in the case of concrete, it becomes a three-phase system including air, mortar and coarse aggregate as shown in Fig. 4.1. The implementation of the VOF method will be discussed in Chapter 4.2. The rest 4 factors all add to the complexity of the mapping between the CFD domain and DEM domain which brings the great concern of numerical stability and accuracy. To this end, the current mapping schemes will be reviewed and discussed in detail. It is found that the majority of current mapping schemes only focus on the calculation of volume fraction and a systematic study on all exchanged variables is absent. To address this issue, the *statistic kernel* method is proposed as a basic scheme to cover the whole mapping process. Combining the VOF method and the kernel-based mapping scheme, the case study will be presented in Chapter 4.4 to show the performance of our extended in-house code.

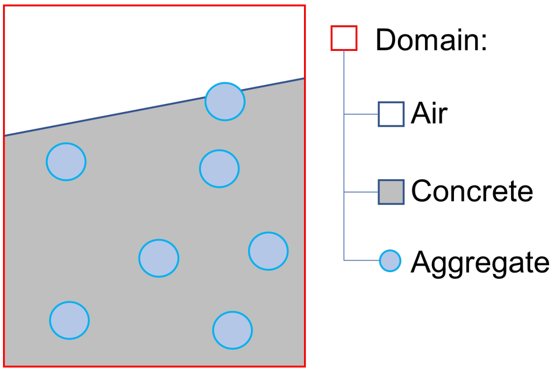

Fig. 4.1 Three-phases system

4.2 Two-phases flow: VOF model

To enable the two-phases flow in the CFD domain, the VOF method is chosen to capture the interface between phases. Besides the two governing equations in Chapter 3.2.1, a 3^{rd} transport equation is required as given:

$$\frac{\partial \alpha_f \varepsilon_1}{\partial t} + \nabla \cdot \left(\alpha_f \boldsymbol{u}_f \varepsilon_1\right) = 0 \tag{4.1}$$

where ε_1 is the volume fraction of fluid phase 1 in the total fluid volume of a certain cell. It is used to indicate the content of different fluids in a cell, and its value varies in the range of 0 to 1. Value 1 means pure fluid phase 1, value 0 represents pure fluid phase 2, and value in between means the mixture of both phases. To distinguish it from the volume fraction α_f and α_p, ε_1 and ε_2 will be called the indicator of fluid phase 1 and phase 2 in the following discussion. For the latter, the VOF method assumes that phases in the same cell share the same velocity; viscosity and density are weighted values of the indicator ε. Mathematically, these assumptions mean:

$$\boldsymbol{u}_f = \boldsymbol{u}_1 = \boldsymbol{u}_2 \tag{4.2}$$

$$\rho_f = \varepsilon_1 \rho_1 + \varepsilon_2 \rho_2 \tag{4.3}$$

$$\mu = \varepsilon_1 \mu_1 + \varepsilon_2 \mu_2 \tag{4.4}$$

$$\varepsilon_1 + \varepsilon_2 = 1. \tag{4.5}$$

In our in-house code, the CICSAM [92] scheme is used to implement the VOF solver. To validate the code, a dam break case was designed to compare the performance of our code and *OpenFOAM*. The geometry and dimension of the domain are given in Fig. 4.2, where the blue area is occupied by water and the grey area is air. Their properties are listed in Table 4.1. The four edges are all non-slip walls, while the interface between air and water is free. So, when the simulation starts, the water will fall under gravity from its right side. This case was run by both OpenFOAM and our in-house code by the CFD solver. Their results are compared by frames as shown in Fig. 4.3. It is obvious that the two sets of results are almost identical which demonstrates the validation of our in-house code.

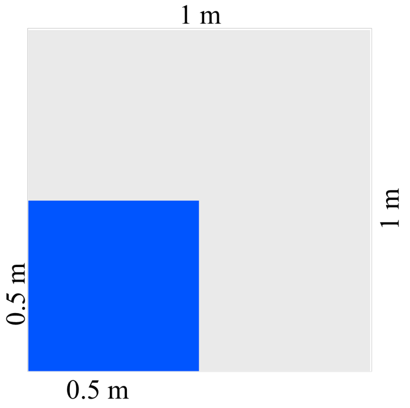

Fig. 4.2 Geometry of dam break

Table 4.1 Fluid properties in dam break case

Material	**Density** (kg/m^{-3})	**Viscosity** ($Pa \cdot s$)
Water	1000	8.9×10^{-4}
Air	1.225	1.8×10^{-5}

In the dam break case, the α_f equals to 1 which is a constant. So, the functionality of the VOF model in the coupled CFD-DEM solver is not discussed yet. This implementation is referred to as the VOF-DEM method in some literature [45, 101, 69, 84]. The coupling scheme of the three-phases system can be described schematically by Fig.4.4. Generally, it can be divided into 2 steps. In the first step, the two fluid phases are treated as one mixed phase. Properties of the latter are computed according to the volume-weighted properties of individual fluid phase as shown in Eqn. 4.3 and 4.4. Thus the mixture field and particle state can be solved by the coupled approach given in Chapter 3. After that, in step 2, the

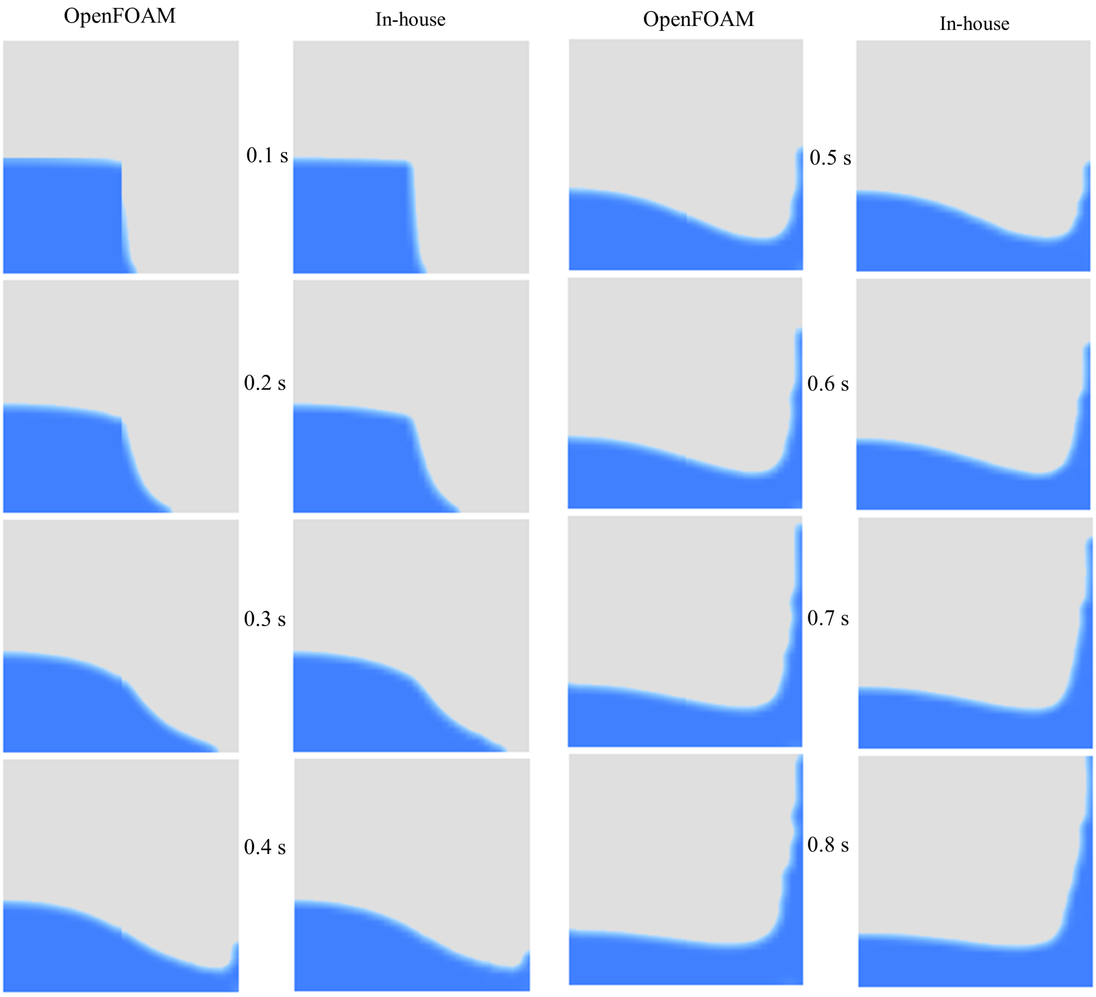

(a) 0.1 s to 0.4 s

(b) 0.5 s to 0.8 s

Fig. 4.3 Dam break result: comparison between OpenFOAM and in-house code

VOF method will be applied to solve the fields for phase 1 and phase 2. Thus, the state of 3 phases is all updated. However, this scheme alone is not sufficient enough to promise a stable and smooth simulation. As will be explained in the next section, the mapped parameters are required to be smooth on the scale of both space and time.

4.3 Mapping in space dimension: volume fraction

Fig. 3.6 in Chapter 3 has listed the variables exchanged between CFD and DEM domains. Among them, the mapping of volume fraction α_p is the most important and should be determined before working on the others. This topic has been investigated by numerous papers and it will be expanded in Chapter 4.3.2. However, the other variables are seldom

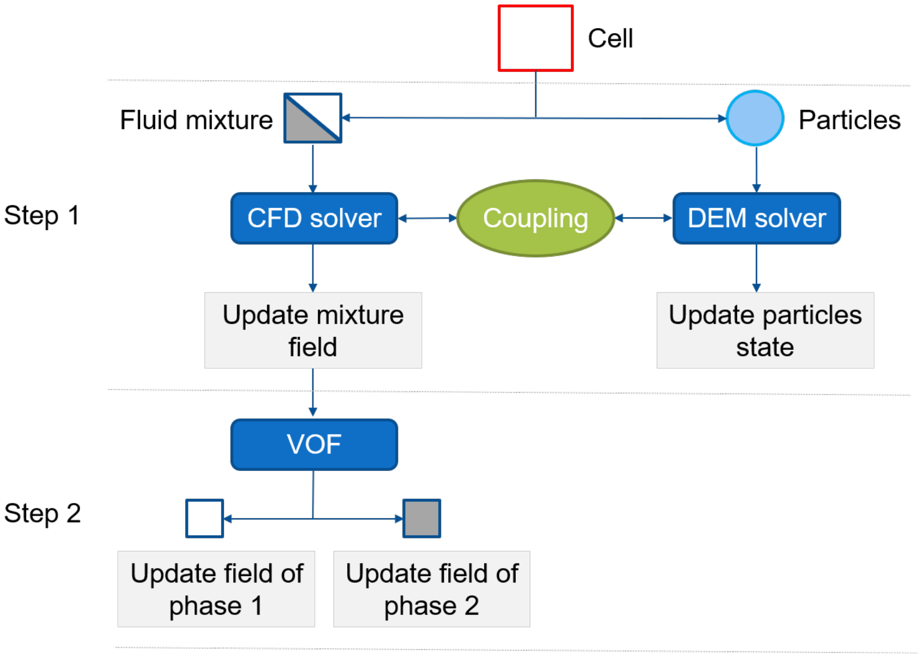

Fig. 4.4 Coupling scheme of the DEM-VOF method

discussed. Especially in the VOF-DEM method, variables of different sources should be treated differently. For example, the volume fraction is a value denoting spatial property while the viscosity involves both material and spatial properties. For a particle straddling on the interface of two fluid phases, the mapping scheme should take both dimensions into consideration.

The mapping process of multiple variables can be concluded into 3 steps.

(1) Establish the spatial relationship or map between the CFD mesh and the point-based particles in DEM, which gives the volume fraction field.

(2) According to the above relation, the variables are collected from local fluid fields and particles to compute fluid-particle forces.

(3) Distribute the computed forces to the CFD and DEM domains.

This chapter only focuses on the first step, and the other two will be discussed in the next Chapter 4.4.

4.3.1 Volume fraction in different equations

According to the unresolved CFD-DEM approach, the value of volume fraction α_f is used in two stages. Firstly, α_f is required in the calculation of fluid-particle forces, which is used in the coupling stage. Secondly, it appears in every terms in CFD governing equations including

Eqn. 3.1, 3.2 and 4.1, which works as an correction due to existence of particles. In different equations, α_f has very different meanings.

For the fluid-particle forces, the value of α_f should be an averaged value in a certain area in the perspective of numerical technique. This point can be explained by taking the drag force as an example. Let's think about the case of one particle dropping in water as given in Fig.4.5. Initially, the domain is full of static water and a particle is dropped at a velocity of 0.001 m/s in the middle of the domain. The width, height and depth are 0.1 m, 0.3 m and 0.1 m respectively. If the case is to be solved by the unresolved CFD-DEM approach, the first thing is to be determined is the meshing of the CFD domain. This is an important factor affecting the simulation accuracy, which can be analyzed by the size ratio of cell size l to particle diameter d. As shown in Fig.4.5, the particles of the same size locate in different cells, whose size ratios varies from 1 to 4. Since the whole particles are inside, the volume fraction α_p can be calculated directly by particle volume over cell volume. It's obvious that the larger the size ratio is, the smaller the α_p is, as shown in Fig.4.6a. Using the Di Felice drag force as an example, the corresponding relationship between α_p and drag force is plotted in Fig. 4.6. It can be seen that while the case is the same, a different size ratio results in diverse initial drag forces because of the varied range used to compute the volume-averaged volume fraction. And, both α_p and $|\boldsymbol{F}_D|$ converges quickly when size ratio grows larger. However, to determine which value is the most accurate, we should come back to the definition of volume fraction. As there is only one particle that is far from the boundaries, theoretically the value of α_p is 0, which gives drag force 1.05×10^{-7} N. So, when the size ratio is above 5, the calculated drag force reaches an error of 1%, and when the size ratio approaches infinite the drag force will converge to the theoretical value.

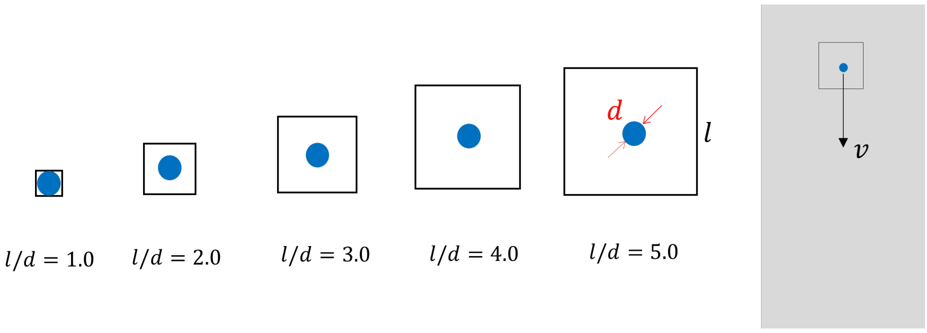

Fig. 4.5 One particle drop: size ratio and volume fraction

The above phenomenon can also be explained analytically. The drag models are commonly derived based on the assumption that the drag force is a function of volume fraction

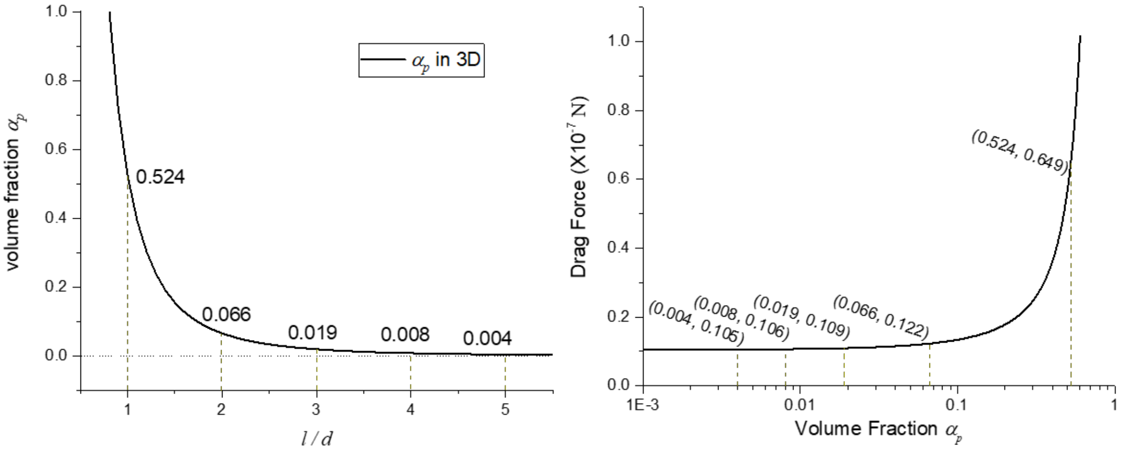

(a) α_p and l/d

(b) α_p and $|\boldsymbol{F}_D|$

Fig. 4.6 The influenced area of a single particle

and Reynolds number. The original definition of the latter is given by

$$\boldsymbol{F}_d = \frac{\rho_f \left|\boldsymbol{u}_f - \boldsymbol{v}\right| d}{\mu}. \tag{4.6}$$

Compared with the formula in Table 3.1, the two of them are different in two aspects. Firstly, the latter for the CFD-DEM approach, the volume fraction α_f is taken into consideration. Secondly, due to the existence of CFD mesh, the $\boldsymbol{u}_f$ is the velocity of the cell where the particle resides. However, in the Eqn.4.6, the fluid velocity is 0 which is of course an apparent value of the whole fluid field. Let's assume such a scenario as shown in Fig.4.7 that a particle is located in a porous medium where the α_f is 0.5 and the inlet velocity at the left boundary is $\boldsymbol{u}$. So, the fluid velocity $\boldsymbol{u}_b$ in the porous area can be given by

$$\boldsymbol{u}_b = \frac{\boldsymbol{u}_f}{\alpha_f} \tag{4.7}$$

Bring it into the formula in Table 3.1, the Eqn.4.6 is obtained. It shows that the definitions of Reynolds number in two formulas are consistent: the value is based on the apparent fluid velocity in a certain large space. The scale of this space is an important factor to determine a correct Reynolds number. In the beginning, the fluid velocity is static, so the relative velocity is constant no matter how large this scale is. However, α_f will decrease as the scale grows larger. The influence of α_f on the drag force has been given in Fig.3.7b. Therefore, we can see that both the two parameters *Re* and α_f are dependent on the averaging scale.

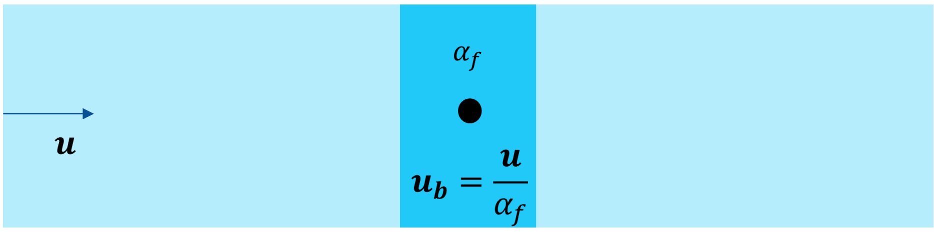

Fig. 4.7 Particle in a porous medium

What's more, if there are a group of particles, the volume used for the calculation should be limited so that the influence of the neighbouring particles can be implied by the value of α_p. While the second limit is a major but unsolved challenge concerning the research community. Many researchers have proposed different scales for the averaging area. For most of them, the value is suggested to be $2 \sim 10$ times of the particle diameter [93, 67, 10, 98].

However, there is an additional upper limit on the cell size because the CFD requires a fine enough mesh to obtain a result with reasonable resolution. Consequently, the conflict often occurs between size ratio requirement and cell size limit when the particle is relatively large compared with the characteristic dimension of the domain. For example, the cell size can be close to the particle diameter or even smaller than that.

For the second purpose, α_p is used to denote the presence of particles in the CFD domain. Similarly, its resolution is also determined by the CFD mesh size and a finer mesh recovers the particles with a higher resolution. In the view of CFD, the drag force on a particle is contributed by the cell(s) where this particle accommodates. So a cell without particles inside won't have momentum exchange. If neighbouring particles exist, their influence on the current particle will be implied by the volume fraction of their cell owners. If a cell is fully occupied, the solved CFD velocity will equal the particle velocity as there is no fluid inside. More importantly, this setup also helps conserve a smooth fluid field. While, for the cells in between, momentum exchange should be considered. Of course, it is possible to use the averaged α_p for drag force calculation, but the resolution of the original CFD mesh is then lost. So, to maintain the best accuracy of a certain mesh, α_p for CFD solver should be calculated directly according to the volume occupied by particles. So, in consideration of accuracy, it can be concluded that:

(1) If the size ratio is in an appropriate range, the resolution of α_p required by the CFD solver would be the same as the resolution for drag force.

(2) If the size ratio is smaller than a pre-defined value, α_p used in CFD solver would have a higher resolution than the one that the drag force requires. The latter should be an averaged value from a group of successive cells to satisfy the pre-defined value.

4.3.2 The state of the art

The most straightforward scheme to compute α_p is the particle centre method (PCM). It assumes that the entire volume of a particle locates in its centre. So, the whole volume is averaged in the cell where the centre is located. This scheme is easy to understand but has a lot of disadvantages which can be explained by assisting of Fig.4.8.

(1) In Fig.4.8a, there are two sub-figures and the size ratio is relatively large. As the particles are all in the cell C, according to the PCM, the volume of all particles will be averaged in cell C which gives α_0 for both figures, while the value of the neighbouring cell F is 0. We can see one major disadvantage for this situation: α_p generated by PCM shows discontinuity property in both space and time scale. In the top figure, the particles locate on the left side of cell C while for the bottom figure the particles are on the right side. Let's assume, the top figure shows the particle position of time t, and the bottom is for time $t+dt$. Since they give the same α_p, we can say that the value of α_p is discontinuous over time. It will have a sudden change if a particle moves inside or outside the cell C. And the minimum portion of such change is based on the particle volume. What's more, as shown in the bottom figure, when a particle approaches the face shared by both cells, the distances between this particle and two cell centres become closer. Theoretically, the influence of this particle on the cell F will be more significant. However, the PCM can not consider this process but results in a sharp gradient between the two cells, which shows the feature of spatial discontinuity. The work of Peng et al. [67] showed that the error of such condition can be up to 50%. As a conclusion, the PCM generates a discontinuous α_p field in both time and space dimensions.

(2) In Fig.4.8b, there are 2 types of particle. Both of their size ratios are relatively small and face the unbounded problem. For example, the 4 smaller particles are straddling on 9 cells in total, but their centres are in the same cell, which means their volume will all be assigned to the same cell according to the PCM. Once the total volume is larger than the cell volume, the value of α_p will exceed 1, which is unphysical. When it comes to the large particle, this problem becomes more severe that α_p is definitely above 1. However, if the size ratio is large, it becomes reasonable to regard the particles as points since they are small compared with cells. In this case, the value of α_p is limited naturally by the particle packing density. The unboundedness is the result of spatial discontinuity of the PCM, and it gives the lower limit of size ratio.

(3) As stated in the last paragraph, the size ratio to apply the PCM must be relatively large. In the circumstances, if the resolution of α_p for drag force is satisfied by the CFD mesh, the two requirements for the α_p fields become the same one, which means only one mapping scheme is enough.

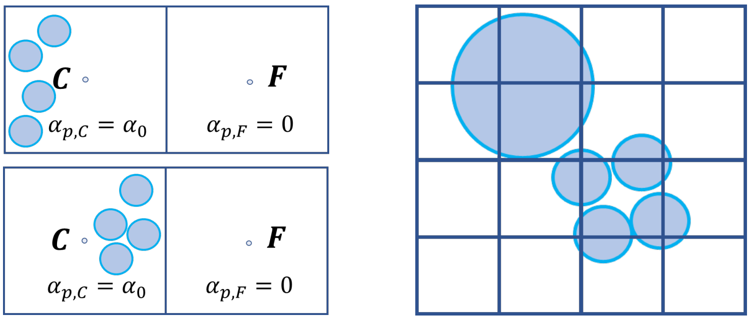

(a) Large size ratio (b) Medium size ratio

Fig. 4.8 Disadvantages of PCM under different size ratio

To address the first two major disadvantages, various mapping schemes have been proposed in the literature. For the unboundedness issue, the divided particle volume method (DPVM), which divides a particle into several sub-parts when it is straddling on multiple cells, was developed from the PCM. Wu et al. [100] generated an analytical solution to divide particles in the unstructured mesh which considered the exact overlap between a particle and the cells it is straddling on. It was proved to provide a smoother α_p [67] but was also very time-consuming. The open package *CFDEM* [47] uses a different implementation for the DPVM. The particle is divided into 29 non-overlapping sub-parts, and the volume of every sub-part is assumed to locate on the respective centroid so that the PCM can be applied for each of them. This method eases the unboundedness issue but still has a limit on the size ratio. For example, when the size of a sub-part is close to the cell size, the unboundedness issue will occur again. Besides the DPVM, there is another group of schemes that solve this issue by enlarging the averaging area. Instead of dividing a particle into smaller parts, this type of scheme will average the particle volume in a set of successive cells, as a consequence of which the size ratio between the enlarged area and the particle would match the requirement of PCM. Link et al. [57] implemented this method by assuming a porous cube in a structured mesh. For every particle, a group of cells that forms a cube will be found as the influenced area, which is the so-called *porous cube*. Following a similar idea, the software *CFDEM* [47] proposed a *big particle* method which uses a bigger virtual porous sphere to represent the real particle in the CFD domain. Accordingly, the original particle volume will be distributed in an averaged manner to the cells that are swapped by the virtual porous sphere. Compared with *porous cube* method which is based on uniform structure mesh, the latter can be used for arbitrary mesh. Taking a step further, Deb and Tafti [24] were firstly proposed the *dual-grid* method to deal with the issue caused by the small size ratio. In the CFD domain, a fine mesh was used to have high resolution on the interface of two fluid phases. Another coarse mesh was involved in calculating α_p. As a consequence, extra interpolation is needed between the two grids. We can see that all the methods focus on the unboundedness issue but pay no attention to the discontinuity issue. The DPVM can produce a more precise α_p field in a fine CFD mesh than the other 3 methods as the latter average particle volume in a larger area. So, the DPVM is intended to satisfy the second α_p requirement for CFD solver, while the other 3 methods tend to match the first requirement for drag force.

To address the discontinuity issue of PCM, some other schemes have been proposed. The *statistic kernel* method, which can be regarded as an development from the *big particle* method, determines the volume distribution of a particle by a distribution function including Gaussian [11, 98] and Johnson distribution functions [109]. The particle is also assumed to affect a porous spherical area in the CFD domain, which is determined by the distribution function. Taking the Gaussian function as an example, its expression is given by

$$f(x) = e^{-\frac{x^2}{2\sigma^2}} \tag{4.8}$$

$$w_{ij} = \frac{f(x_{ij}) V_{cell,j}}{\sum_j f(x_{ij}) V_{cell,j}} \tag{4.9}$$

where f denotes the distribution function, w_j is the weighting factor of cell j, x_{ij} is for the distance between particle i and cell j, and σ is the standard deviation used to control density distribution. It means that the particle is treated as a porous sphere in the CFD domain, and w is evaluated by the distance x. The closer a cell to the particle centre is, the larger the w is. In 2015, Sun and Xiao [83] proposed a *diffusion-based* method to solve the two issues of PCM or DPVM. It starts from the result given by PCM, where the field may be discontinuous in space and have overshooting value of α_p. Then, α_p is treated as a diffusive variable and a transient diffusion equation can be established as given in Eqn.4.10. The $\tilde{t}$ denotes the pseudo time of the simulation. Thus, driven by the α_p gradient between cells, there will be flux from a cell with a high value to a cell with a lower value. After a certain duration, a smooth field will be achieved and the maximum value will decrease to a value below the maximum particle packing density. The latter can be used as a criterion to set the number of time steps. In the paper of Sun and Xiao, the *diffusion-based* method is proved to be equivalent to the Gaussian-based *statistic kernel* method. Compared with the latter, the former is easier to implement and much less time-consuming. However, after the diffusion process, the quantitative mapping relationship is unknown because the flux of α_p between cells is the total amount of exchange that can not be decomposed into portions from different particles. So, in the further mapping process, the consistency between α_p and other variables can not be conserved. According to the above two methods, the α_p field changes every time particle moves and its value is smoothed in the space since it is distance-evaluated. As a consequence, both methods solve not only the unboundedness issue but also the discontinuity issue. However, despite the advantages of the distance-evaluated method, as the α_p is not averaged in the influenced area, the two methods do not intend to match the requirement for drag force calculation. Although an averaged field can be approximated by using a large σ in *statistic kernel* method or more steps in the *diffusion-based* method, the high resolution of α_p is then violated which doesn't match the requirement for CFD solver.

$$\frac{\partial \alpha_p}{\partial \tilde{t}} = \nabla^2 \alpha_p \tag{4.10}$$

In conclusion, the disadvantages of PCM have been sufficiently studied by researchers, and many different methods have been proposed to improve PCM. Some of the methods solve the disadvantage partially such as the DPVM, *porous cube* method, *big particle* method and *dual-grid* method. While the *statistic kernel* method and *diffusion-based* method solve the disadvantages in one frame and both of them are flexible enough to work for all types of mesh and a full range of size ratio. It provides a smooth α_p field whose value is bounded naturally when appropriate parameter σ is used.

4.3.3 Summary

The information of the last two chapters can be concluded in Fig.4.9. According to the resolution of generated α_p, the mapping methods can be divided into 2 groups. For the PCM, *porous cube/sphere*, *dual-grid* methods, they give a relative low resolution in volume fraction field as the latter is averaged in a relative large area. For the rest 3 methods, they can provide high resolution. Given that, the mapping of volume fraction in the study will be carried out in two steps as the following:

(1) *statistic kernel* method is used to generate a smooth and high-resolution volume fraction field in the CFD domain;

(2) in computing fluid-particle forces, the volume fraction is to be averaged from the cells in pre-defined ranges.

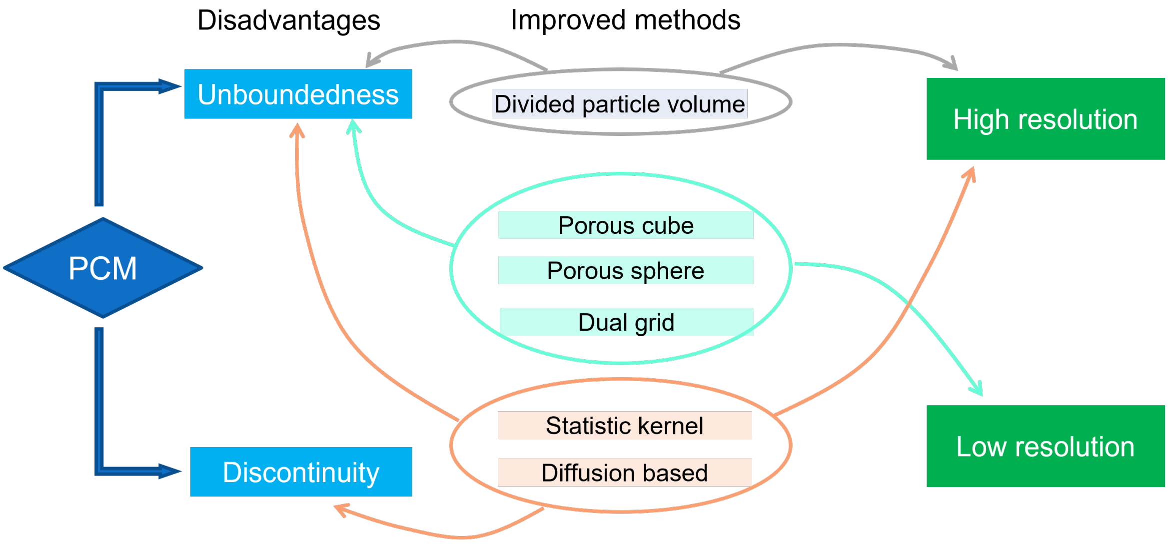

Fig. 4.9 Summary of mapping method for volume fraction

Due to the diverse particle diameter and cell size in concrete simulation, none of the above 7 can be used directly as a unified method working for all combinations. If the particle is much larger than the cell size, the DPVM has to divide the particle into more parts which would be very time-consuming. For the *porous cube*, *porous sphere* and *dual-grid* methods, they can not provide a high-resolution α_p field since they averages particle volume in a large area. The *statistic kernel* or *diffusion based* methods uses evaluates volume fraction by the particle-cell distance and doesn't consider the particle shape. So, if the particle is much larger than the cell size, the chosen of σ would be a problem, because α_p value at the particle center could be unbounded if σ is too small. However, if the latter is not small enough, the particle volume will be smeared in relative large space. What's more, in reality, the cells inside the particle are fully occupied by the particle, so the virtual fluid field should be equivalent. Both methods can not promise this point in the current framework. Because of that, an improved smooth distribution function (Eqn. 4.11) is developed, which takes the particle radius and cell size into consideration

$$f(x) = \begin{cases} e^{-\frac{|x-r,\,0|^2_{max}}{2\sigma^2}} & \text{if } x \leq l+r \\ 0 & \text{if } x > l+r \end{cases} \tag{4.11}$$

$$\sigma = |l, r|_{min} \tag{4.12}$$

where r denotes the particle radius, $|x-r,\ 0|_{max}$ gives the maximum value between $x-r$ and 0, and $|l,r|_{min}$ returns the minimum value between l and r. The performance of Eqn.4.11

is shown in Fig.4.10, where the size ratio of the cases varies in the range of $1/20$ to 10. $|x-r,0|_{max}$ is used to check if a cell center is inside or outside of a particle. If it is inside, $x-r$ would be negative, so the larger value 0 will be returned. If not, $x-r$ becomes positive and will be output. As a result, this term gives the same value for all the cells inside the particle, which is shown demonstrated by sub-figures $1/20$, $1/10$ and $1/5$ in Fig.4.10. In other words, these cells have the same distributing density in the space, which is physically better than Eqn.4.8 which uses x directly. To avoid the possible violation of the upper limit in α_p, the particle volume is allowed to distribute in a wider range outside of the particle, which is characterized by the standard deviation σ. Its value takes the minimum one between particle radius r and cell size l to increase the resolution. Taking the case of size ratio $1/20$ for an example, l is much finer than r so that the former is used for σ to shrink the porous layer outside of the particle. On the contrary to that, for the case of size ratio 10, r is much smaller than l. Using the former for σ can increase the volume concentration which increases the resolution in α_p field. The distribution area is cut off at the distance $l+r$, which means the one or two cells off the particle surface are considered as the influenced area to achieve a smooth volume fraction field. So, at least 3 cells in each dimension will be used. In conclusion, this improved distribution function maintains a great balance between high resolution and field smoothness.

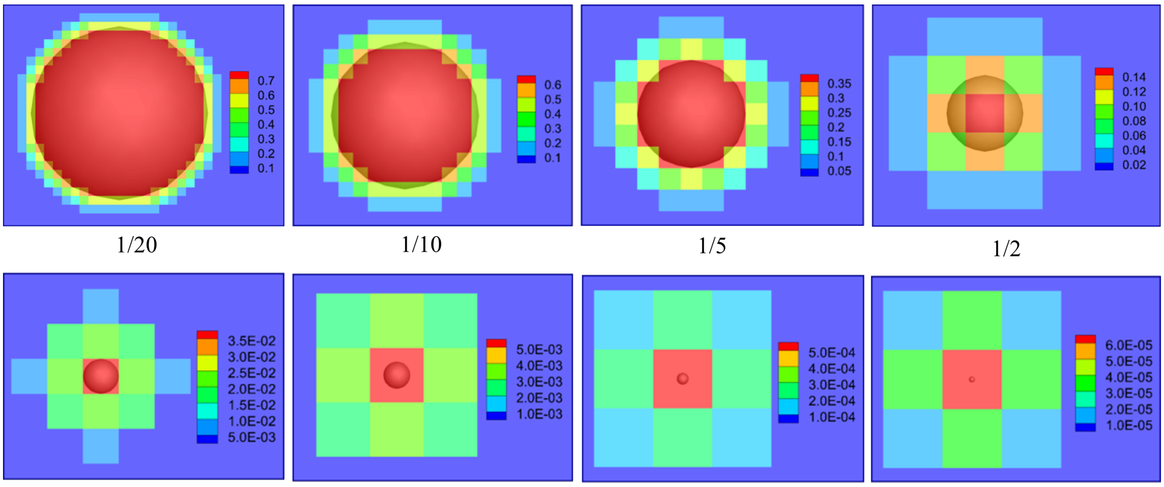

1/20 1/10 1/5 1/2

1 2 5 10

Fig. 4.10 The α_p field VS size ratio l/d

For step (2), the pre-defined area is still a hard question facing debate. According to suggestions in the literature, a commonly used value $3d$ will be applied in this study.

4.4 VOF-DEM method: force mapping and case application

4.4.1 Mapping of variables in different dimensions

The α_p is used to represent the relationship between CFD and DEM domains in space dimension. Referring to the drag model, variables in other dimensions should be considered for mapping including the material dimension (such as μ and ρ_f) and the time dimension (involving kinematic variables such as $\boldsymbol{u}_f$, $\boldsymbol{v}_p$ and so on). The three dimensions are corresponding to the 3 base units m, kg and s. If it is a single Newtonian fluid on the CFD side, the material domain will be homogeneous which indicates the mapping is not necessary. However, if it comes to the concrete simulation, the case will be very complicated. Firstly, the fluid is non-Newtonian which means the viscosity is diverse in the space. Secondly, as there are two fluid phases, material variables are not homogeneous anymore. Thirdly, as the drag force involves variables of 3 dimensions, the weighting factor used to distribute this force should consider the contribution of all sides.

Firstly, in the space dimension, the time is also uniform in both forward and backward directions. However, as the mapping is performed for variables at the same time, it is not necessary to discuss this dimension.

In the space dimension, besides α_p, other variables relating to the unit of length m are also involved such as the kinematic variables position, velocity, acceleration and so on. Because in the Cartesian coordinate system, the length scale is uniform in every direction. Therefore, it is reasonable to adopt the distance-evaluated method to map the longitudinal value without considering the direction in the space dimension. Although the kinematic variables often relate to the time dimension like the velocity, they are always mapped at the same time. Therefore, such variables can be classified into the same group as the space dimension.

In the material dimension, two factors - non-Newtonian fluid and multiphase flow - would add to the complexity of the mapping process greatly. Firstly, in the field of a non-Newtonian fluid, the viscosity is a function of shear rate, which means its value is non-constant. As it is an important parameter in the drag model, the viscosity should be mapped onto the particles. Secondly, when there are multiple fluids in the CFD domain, all material related variables could be diverse in the space including density and viscosity. This phenomenon happens at the interface of two phases, where the value of ε_1 is between 0 and 1. So, when a particle is close to or straddling on an interface, relative variables should be mapped by appropriate methods. In this study, only incompressible fluids are considered and an individual material is homogeneously distributed in space. So, they can be treated in the same manner as spatial variables.

In the first step, the statistic kernel function is used to map the volume fraction in the CFD domain, and the expression is given by:

$$\alpha_{p,j} = \frac{\sum_i w_{ij} V_{p,i}}{V_{cell,j}} \tag{4.13}$$

where i and j are indices for particle and cell respectively, and w_{ij} denotes the weighting factor when mapping the volume of particle i to cell j. To explain the step 2 and 3, the drag force is taken as an example. Referring to the Table 3.1, the drag force requires CFD variables α_f, $\boldsymbol{u}_f$, μ and ρ_f, and DEM variables $\boldsymbol{v}$ and d. For the former 4 variables, they will be treated in the same manner, in which they are to be averaged in a certain area to match the size ratio requirement from the drag model. It can be expressed by:

$$\phi_{p,i} = \frac{\sum_j w_{ij} \phi_{f,j} V_{cell,j}}{\sum_j w_{ij} V_{cell,j}} \tag{4.14}$$

where $\phi_{p,j}$ denotes the value of variable ϕ for particle j, $\phi_{f,i}$ is for the value at cell i and $V_{cell,i}$ is the volume of cell i. When all parameters are ready at the particle position, the drag force can be computed. Then we need to think about how to map the drag force to the CFD domain. The drag force involves variables from space domain like α_f and $\boldsymbol{u}_f$, and material domain including ρ_f and μ. So mapping the drag force to a certain cell, both its relative position and material property should be counted. In the framework of the unresolved CFD-DEM approach, the particles are treated as porous media in the CFD domain, which has a larger size than its diameter. For a cell contributing to the drag force, the $\boldsymbol{u}_f$, μ, ρ_f, V_{cell} and the accommodated portion of particle volume are all important factors in determining the weight factor. However, the drag models are derived empirically. The field of fluid velocity around a particle is very complicated. So, to avoid the instability issue, the influence of $\boldsymbol{u}_f$ is not weighted in the mapping. While all the other mentioned factors will be treated equally. The consequential mapping of drag force is given by Eqn. 4.15 and 4.16.

$$\boldsymbol{F}_{d,ij} = w_{d,ij} \boldsymbol{F}_{d,i} \tag{4.15}$$

$$w_{d,ij} = \frac{\rho_{f,j} \alpha_f \mu_j w_{ij}}{\sum_i \rho_{f,j} \alpha_f \mu_j w_{ij}} \tag{4.16}$$

where $\boldsymbol{F}_{d,i}$ denotes drag force acting on particle i, $\boldsymbol{F}_{d,ij}$ is the contribution of cell j to drag force $\boldsymbol{F}_{d,i}$ and $w_{d,ij}$ is the weighting factor for drag force mapping between particle i and cell j. If α_f of a cell is 1, it means the cell is pure fluid and w_{ij} will equal to 0 either, which results in a 0 value in $w_{d,ij}$. If α_f equals to 1, the cell is fully occupied by particle. In this case, the relative velocity becomes 0 because the virtual fluid velocity equals to the particle velocity. For a α_f in the range of $0 \sim 1$, it indicates part of particle surface is in the current cell so that drag force should be assigned. Based on the same logic, the other particle-fluid forces like the lift forces and virtual mass force can be mapped. And once the mapping methods for variables in all dimensions are implemented for the VOF-DEM method, our in-house code is ready to simulate the three-phase system.

4.4.2 Case application

The coupling of our in-house code is implemented according to the introduced methods. To validate its performance, 3 different cases were designed. In the first case, a medium size ratio was considered and a group of particles were dropped from the air into water. In the second case, there was a big particle dropping from air into the water which considered the small size ratio. In the last case, the particle-fluid torque due to relative rotation was implemented according to the scheme given in Chapter 4.4.1. For demonstration, a big rotating particle straddling on the interface of water and air was simulated. In terms of the large size ratio, it won't be covered here since it has been sufficiently discussed in the literature.

Case 1: dropping of a group of particle

In this case, a group of 750 particles are released from the air phase and dropped into the water phase. As shown in Fig.4.11a, the fluid domain has a 2 m height in total, half of which is occupied by air (transparent domain) and the other is water (green domain). The width and thickness of the domain are 1 m and 0.4 m respectively. Fig.4.11b shows the initial position of particles. It can be seen that they are randomly distributed in the air phase. The material parameters of both CFD and DEM are listed in Table 4.2. The gravitation acceleration is 9.81 m/s^2. The cell size of CFD mesh is 0.05 m, which gives a medium size ratio 1.25 (as shown in Fig.4.12a). For the particle-fluid forces, only the drag force and pressure gradient force are activated. Besides, the surface tension is not considered either.

In the simulation, the time step of CFD was set to be 0.0001 s and the DEM was 0.00001 s, which gives a ratio of 10. In total, duration of 4 s was run for this case. The simulation result is presented in Fig. 4.12 and 4.13. The former shows the water level on the first and final steps. According to Fig. 4.12b, at the time 4 s, all the particles had settled on the bottom of the container, and the water-air interface was almost level. By taking an average, the water level was measured to arise by 0.0623 m compared with the initial, which indicates a volume increase of 2.491×10^{-2} m^3 in the green domain. Accordingly, the final water level should be 1.0628 m. To show the volume change in the green domain, the history of its averaged level was tracked as shown in Fig.4.12c. In the duration of $0 \sim 0.4$ s, the level of the green domain was increasing gradually because of the entrance of the particles. After that, the average level reached its peak which gives a value 1.0625. Respecting to rise in average level, it shows a numerical error of 4.8×10^{-3} which is really small. The whole process of the particles crossing the water-air interface is presented in Fig. 4.13. We can see that all the particles entered the water phase at 0.4 s which is in accordance with the Fig.4.12c. In this figure, there are two sets of graphs in it: the top 9 show the relative position of the particles respecting the water-air interface; the bottom 9 display the disturbance of the interface. The result shows that the in-house VOF-DEM method holds the volume conservation successfully and is capable to generate a reasonable result for the case with a medium size ratio.

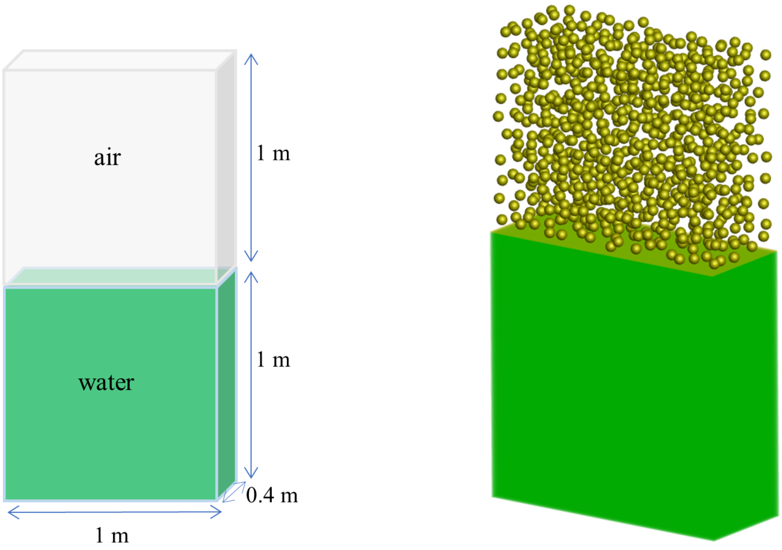

(a) Geometry (b) Initial position of particles

Fig. 4.11 Design of case 1

Table 4.2 Material properties of case 1

DEM Parameters	Value	CFD Parameters	Value
Density	2500 kg/m^3	Air Density	1.225kg/m^3
Diameter	0.04 m	Air Viscosity	0.000018 $Pa \cdot s$
Young's Modulus	5.0×10^6 Pa	Water Density	1000 kg/m^3
Restitution Coefficient	0.97	Water Viscosity	0.00089 $Pa \cdot s$
Friction Coefficient	0.1		
Poisson's Ratio	0.49		

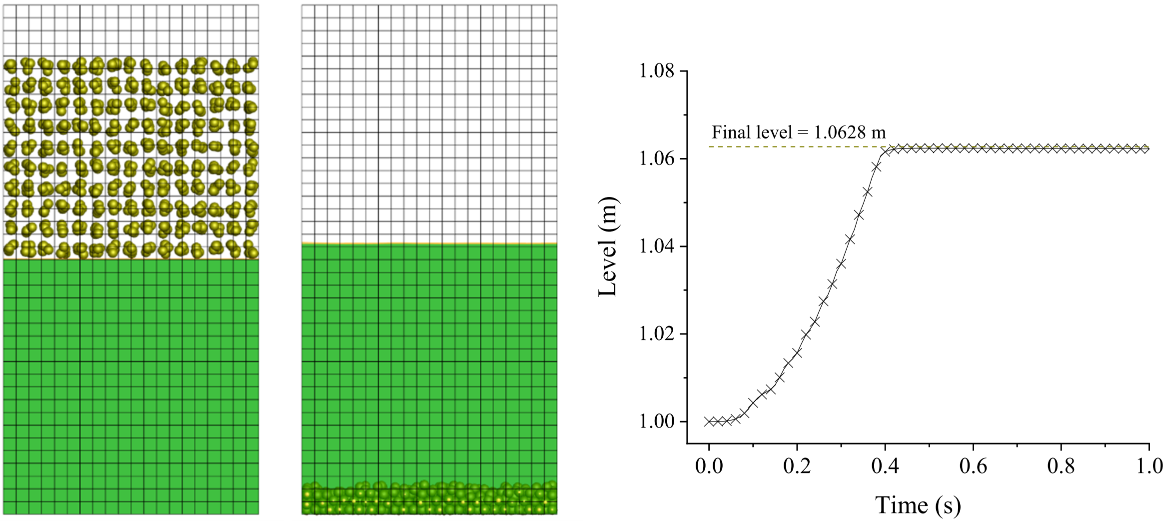

(a) Initial level (b) Final level (c) History of averaged water level

Fig. 4.12 Case 1: arising of water level

Case 2: drop of a big particle

This case is designed to simulate a big particle falling into water from the air. As shown in Fig. 4.14, the dimension of the CFD domain is 0.5 m × 0.5 m × 1.0 m, and the bottom point of big particle locates in the middle of the domain which is exactly on the top the water surface. The material properties are listed in Table 4.3 which is the same with Table 4.2 except the particle size. This case has a relative small size ratio $1/8$, where the cell size is 0.025 m and the particle diameter is 0.2 m as shown in Fig.4.14c. In total, a duration of 1 s was simulated. When the whole particle was in the water, the volume of the green domain was supposed to be increased by the amount of the particle volume which was 4.12×10^{-3} m^3. Fig.4.15 shows the history of the volume of the green domain. We can see that the curve reaches the expected value 0.12912 m^3 at about 0.3 s. The curve is composed of 2

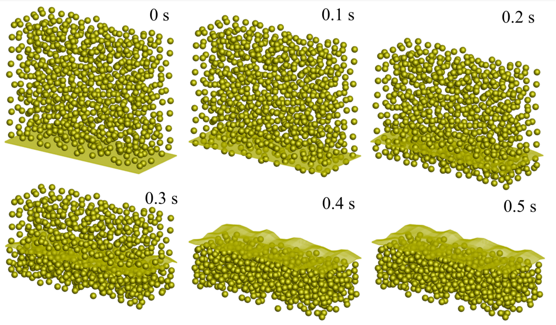

(a) Passing interface

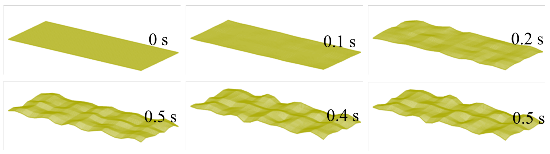

(b) Disturbance of the water surface

Fig. 4.13 Case 1: dropping of particles

stages: the increasing stage and the converged stage. The first stage is in accordance with the interface crossing process. The increasing rate is small at the beginning and end and reaches the maximum in the middle. This is determined by the spherical shape of the particle. The cross-sectional area is small and increases towards the particle center. In the second stage, the whole particle was in the water so that the volume didn't change any more. This case again proves the volume conservation of the VOF-DEM method.

The falling process of the particle is plotted in Fig.4.16. Compared with Case 1, we can see that this case provides a higher resolution in the local field of an individual particle. Its motion can be divided into 3 stages. The duration of $0 \sim 0.3\ s$ was the first stage when the particle entered the water and created a pit on the surface. On the second stage $0.3 \sim 0.6\ s$, the particle hit the bottom and bumped back. In the meanwhile, the water was pushed upwards which diminished the pit and created a peak instead. On the last stage from $0.6\ s$ to $1.0\ s$, the particle fell downwards again and a stronger wave appeared. This case shows that the VOF-DEM is capable to simulate a case with a small size ratio.

Case 3: rotation of a big particle

The purpose of this case is to demonstrate the implementation of torque $\left(\boldsymbol{T}_{fp}\right)$ due to relative rotation between fluid and particle, which is based on the mapping scheme for interacting forces. The expression for the torque has been given in Table 3.1. As shown in Fig. 4.17, this case uses the same configuration of Case 2 except for the particle position. Initially, the

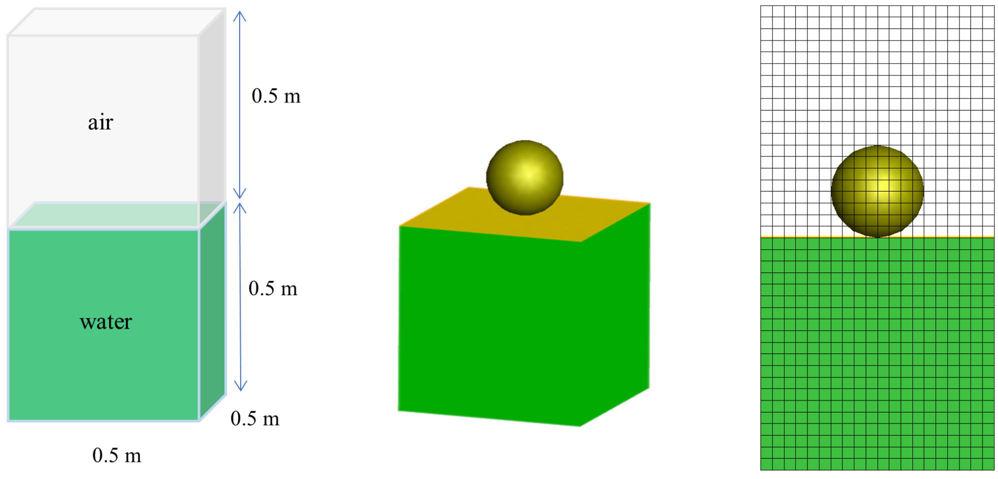

(a) Geometry (b) Initial position of particles (c) Size ratio of 8

Fig. 4.14 Design of case 2

Table 4.3 Material properties of case 2

DEM Parameters	**Value**	**CFD Parameters**	**Value**
Density	2500 kg/m^3	Air Density	1.225kg/m^3
Diameter	0.2 m	Air Viscosity	0.000018 $Pa \cdot s$
Young's Modulus	5.0×10^6 Pa	Water Density	1000 kg/m^3
Restitution Coefficient	0.97	Water Viscosity	0.00089 $Pa \cdot s$
Friction Coefficient	0.1		
Poisson's Ratio	0.45		

particle centre was located on the centre of the CFD domain so that half of the particle was in water and half in the air. It was fixed on its centre and spinning respecting to its vertical axis at a constant angular velocity 5 rad/s (anti-clockwise). In the expression of $\boldsymbol{T}_{fp}$, the variables includes μ and the relative angular velocity $\boldsymbol{\omega}_f - \boldsymbol{\omega}_p$. The mapping of the former has been used in Chapter 4.4.1. For the latter, the same mapping method for $\boldsymbol{u}_f - \boldsymbol{v}$ will be applied. Then, the torque acting on the particle can be computed. However, this value can not be mapped to the CFD mesh directly. As depicted in Fig.4.18, the value mapped to the each cell should be a force $\boldsymbol{F}_t$, which can not be obtained directly from $\boldsymbol{T}_{fp}$. The relation between the two of them can be given by

$$\boldsymbol{T}_{fp} = \sum_j \boldsymbol{F}_{t,j} d_j \tag{4.17}$$

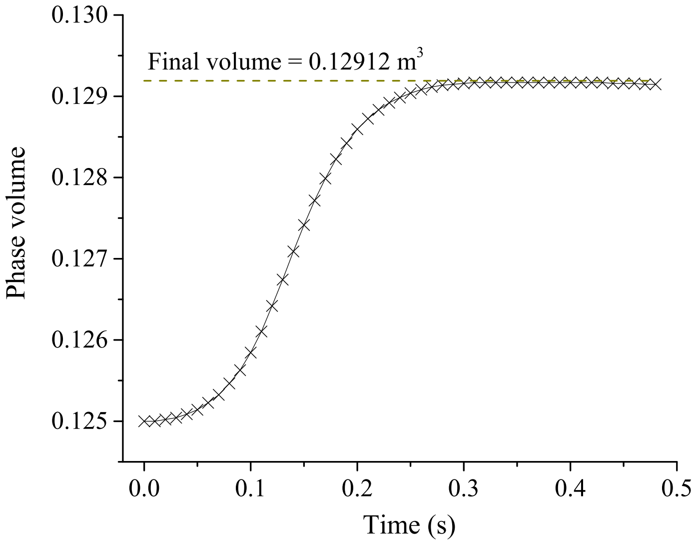

Fig. 4.15 History of the volume of green domain

where j is the index of neighbouring cells. Assume that the contribution of a cell on $\boldsymbol{T}_{fp}$ can be weighted by w_t. Therefore, $\boldsymbol{F}_{t,j}$ can be computed by

$$\boldsymbol{F}_{t,j} = \frac{w_{t,j}\boldsymbol{T}_{fp} \times \boldsymbol{d}_j}{\left|d_j\right|^2} \tag{4.18}$$

where $\boldsymbol{d}_j$ denotes the distance vector pointed from the particle centre to the cell centre. It indicates that $\boldsymbol{F}_t$ must be normal to $\boldsymbol{d}_t$ and $\boldsymbol{T}_{fp}$, because any other component makes no contribution to $\boldsymbol{T}_{fp}$. Referring to the expression of w_d given in Eqn.4.16, w_t is to be computed by

$$w_{t,j} = \frac{\mu_j w_j}{\sum_j \mu_j w_j}. \tag{4.19}$$

A step further, for implicit implementation in CFD, a torque-induced coefficient $\boldsymbol{K}_t$ is defined as

$$\boldsymbol{F}_{t,j} = \boldsymbol{K}_{t,j} \times (\boldsymbol{\omega}_{f,j} - \boldsymbol{\omega}_p) \tag{4.20}$$

$$\boldsymbol{K}_{t,j} = \frac{\boldsymbol{F}_{t,j} \times \left(\boldsymbol{\omega}_{f,j} - \boldsymbol{\omega}_p\right)}{\left|\boldsymbol{\omega}_{f,j} - \boldsymbol{\omega}_p\right|^2}. \tag{4.21}$$

The above mapping scheme was implemented in our in-house code, and the Case 3 was designed for demonstration. In total, a duration of 4 s was simulated with a time step 0.0001 s, and the result is presented in Fig.4.19. It shows that, while the particle kept rotating, the water was driven to follow synchronously. The wave on water surface grew stronger over

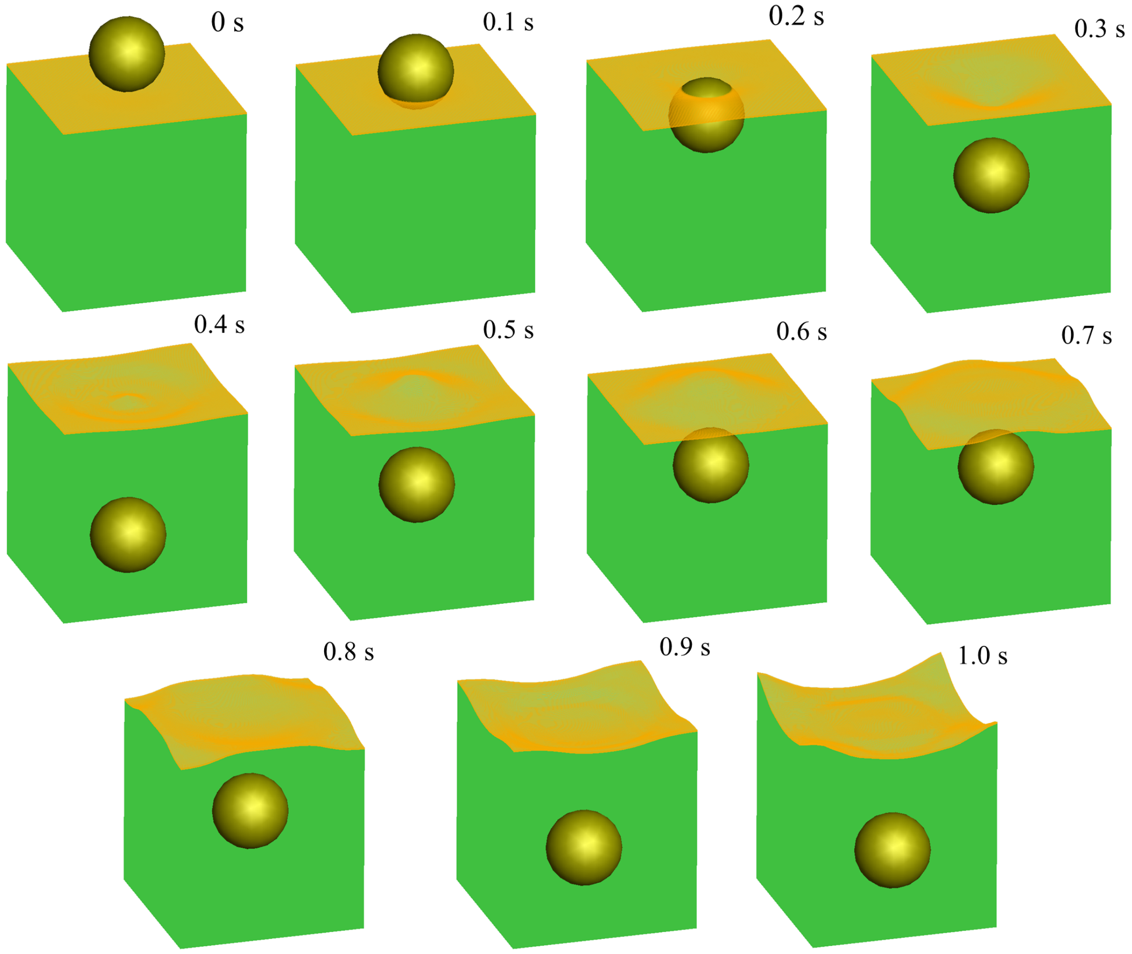

Fig. 4.16 Result of case 2

time and reached the peak at time 4 s. The reasonable result shows that the mapping scheme works well for the fluid-particle torque.

4.5 Conclusions

In Chapter 4, the unresolved CFD-DEM approach was introduced and the model of Bingham fluid was implemented. However, for concrete flow simulation, more functions must be developed. Firstly, the multiphase model should be embedded into the framework of the unresolved CFD-DEM approach. Because in most applications the fresh concrete flow is a process of free-surface flow. As the Eulerian FVM is used for the CFD, the air phase also is involved which requires a multiphase model. Secondly, the CFD mesh and aggregate size both vary in a quite large range, which brings difficulties into the mapping process between

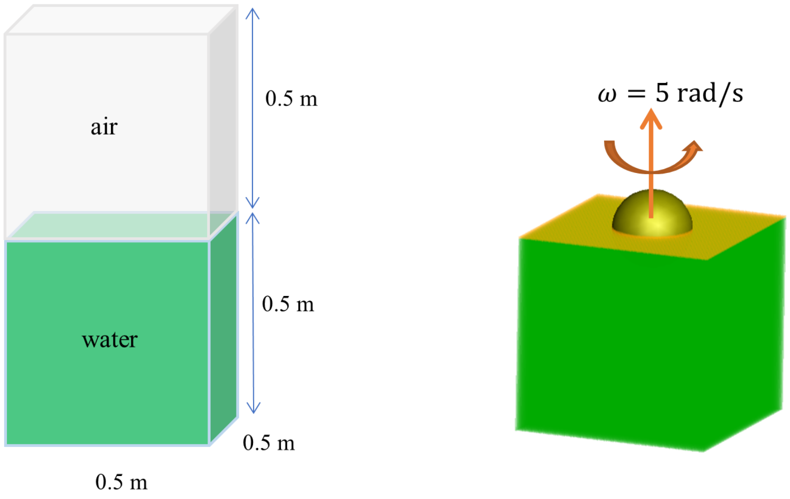

(a) Geometry (b) Initial position of particles

Fig. 4.17 Design of case 3

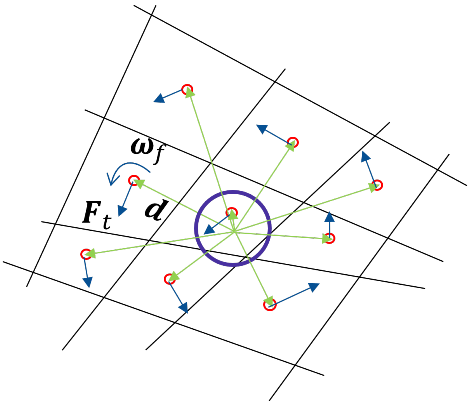

Fig. 4.18 Schematic of torque mapping

CFD and DEM. In addition, the sharp gradient of material properties around the fluid interface also worsens the situation. They all ask for a smooth mapping method independent of the size ratio between CFD cell and particle diameter.

For the first purpose, the VOF method was applied to solve the multiphase fluid flow, and a transport equation was added as the third CFD governing equation. The performance of the VOF in our in-house code is validated by a dam break case. Embedding the VOF method in the unresolved CFD-DEM approach is the so-called VOF-DEM method. A step further, to achieve a stable simulation with the VOF-DEM method, a smooth mapping scheme is required, which is in the same position as the second problem.

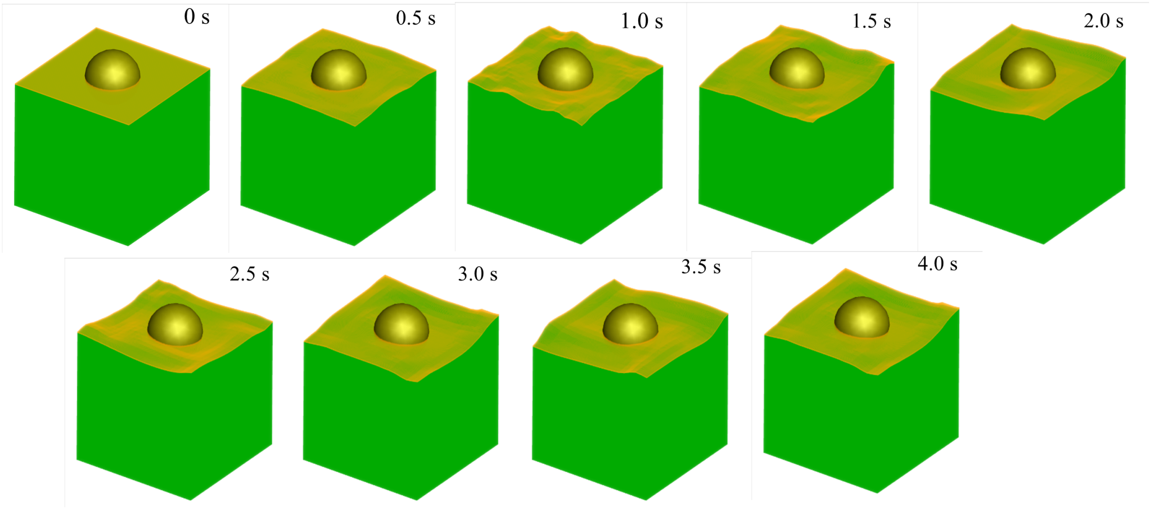

Fig. 4.19 Result of case 3

On the coupling stage, there are several variables to be mapped forth or back such as particle volume, fluid-particle forces, fluid velocity, pressure gradient etc. Based on the dimensional analysis, these variables involve 3 dimensions: time, space and material. As the coupling of CFD and DEM occurs in the same instant, the dimension of time doesn't need to be considered. In terms of space and material dimensions, they are homogeneous in the domain which means no specific direction is required. The second problem concerns most about the mapping of particle volume which happens in the space dimension and gives the significant variable α_p (also α_f). As an important variable in CFD governing equations, it is supposed to imply the particle existence with a resolution as high as possible. While, in the calculation of particle-fluid forces such as drag force, an apparent value in a certain large area is demanded. Therefore, the mapping scheme of volume fraction in this study is determined as: for the field in CFD, statistic kernel method with an improved distribution function is used for mapping; in the calculation of forces, the averaged value in the influenced field of a particle is applied. In addition, for the latter, all the relative variables like fluid velocity, pressure gradient, fluid density, viscosity and so on should follow the same averaged manner. However, when mapping the computed forces to the CFD mesh, the contribution of the variables in the material dimension should be counted differently. Taking drag force as an example, the cell with higher viscosity, higher fluid density and higher fluid volume fraction should be assigned a larger weighting factor. In conclusion, the CFD domain requires a high resolution in the mapped field to solve a more accurate result in the local field around a particle. However, in terms of the fluid-particle forces, the models given in the literature are all derived based on a far fluid field. Therefore, the apparent value of relative variables in a certain area is proposed to use.

In the study of the unresolved CFD-DEM approach, quantitative validation is always a major challenge that requires a lot more effort. It will become a research topic beyond this thesis. In this chapter, 3 cases were designed to phenomenally demonstrate the VOF-DEM method and the mapping scheme. The first case simulated the falling of a group of particles from air into water, where the size ratio is medium. Meanwhile, the rising water level and chaotic surface disturbance were tracked. The result shows that the VOF-DEM could conserve the individual fluid volume while the interface-passing happened. What's more, the method is capable to capture a reasonable phenomenon in this process. In Case 2, a big particle was used to run the free drop simulation. Its size ratio was $1/8$ which is quite small. The same objects were tracked and similar conclusions were drawn. The two cases prove the validation of the VOF-DEM method on a full range of size ratio. In Case 3, by referring to the mapping scheme for the interacting forces, the torque due to the relative rotation was discussed and implemented in our in-house code. In the simulation, a fixed big particle was designed to straddle on the interface of two fluids and rotate at a constant angular velocity. The in-house code generated a reasonable torque-induced wave on the water surface. In conclusion, the 3 cases show that the VOF-DEM method cooperates with the mapping scheme and is versatile enough to handle various situations.

Chapter 5

Relaxing scheme: release the drag-induced time step criteria

5.1 Literature review

For dynamic simulation, the time step criterion is inherent, as the core of the numerical method is to assume some time-dependent variables to be constant in every time step. Therefore, to promise the accuracy of the simulation, the time step should be small enough to ensure these assumptions are reasonable. In terms of the unresolved CFD-DEM approach, there are two different sources of criteria. The first group of criteria are given by the two solvers individually without the coupling. There has been numerous stability study on both pure CFD and pure DEM, so they won't be expanded here. The second source is the exchanged fluid-particle forces, which introduce extra time step constraints to both CFD and DEM solvers. Taking the most important component drag force as an example, it is a high-order function of the relative velocity between fluid and particle, where a reasonable small time step is needed. If its value is smaller than those from the first source, it becomes the critical value in determining CFD/DEM stepping scheme. However, despite such importance, the research on this topic is still very limited. Kloss et al. [47] mentioned that the DEM time step needs to be set at an order of magnitude smaller than the CFD time step, which is a rather subjective suggestion. But, for some specific cases such as chemical reactions on the CFD side, a small CFD time step is also desired. Blais et al. [8] proposed the solutions for drag-induced critical time step for both DEM and CFD solvers. However, they were given without detailed derivation and case validation. Compared with the solutions proposed in this study, the DEM solution is agreed but the CFD solution is not. F. Mikito [38] pointed out that high viscosity (above 100 $Pa \cdot s$) will result in a very small time step which makes the computational cost unaffordable. To deal with the issue, he proposed a simple method to enable the geodynamic simulation by the unresolved CFD-DEM approach, which ignores the inertial term of every particle in the DEM solver. In other words, it means that every particle reaches a new equilibrium state instantaneously at the beginning of every step, so the drag-induced time step constraint is removed. Based on the same manner, the CFD governing equations are also simplified to allow a larger time step. As it ignores the acceleration process in both solvers, its application is limited.

In the most study, the drag-induced critical time step is larger than a pure CFD or DEM solver. As will be proved in this study, smaller particle diameter and higher fluid viscosity will decrease the drag-induced criteria. Therefore, as the most common fluids, air and water have a very small viscosity, such cases usually don't need to be concerned. But when the drag-induced criteria become dominant, there is no robust solution to give the evaluation yet. What's more, in some cases, the drag-induced critical time step is so small that the computational cost becomes unacceptable, such as the cases with high viscosity (magma, fresh concrete, grease et al.) and small particle size (all kinds of colloid such as cement paste, slurry and smog). Taking the fresh concrete as an example which is a classic Bingham fluid, it has extreme large apparent viscosity when the shear rate is very small and the consequent critical time step can be as small as 10^{-9} s for both CFD and DEM. However, unfortunately, a general and robust method to deal with these extreme drag-induced time step criteria is absent either. Not to mention, the CFD always desires a larger time step because of the high computational cost compared with DEM.

Given the above knowledge, this study also focuses on the drag-induced time step constraints and makes it our target to propose a versatile method to remove them, which is case-independent. Two goals are achieved: obtain robust derivation for the drag-induced time step constraints for both DEM and CFD solvers; remove the two constraints by applying the relaxing scheme. In the perspective of a particle, the drag force works as a damp, which is always opposite to the direction of relative velocity. Every time the particle state (force, velocity, acceleration or others) changes, the particle will relax itself to a new equilibrium by the drag force. In the unresolved CFD-DEM approach, the DEM solver assumes the drag force to be constant in every time step, while the CFD solver assumes the drag force is proportional to the relative velocity. Because the equilibrium state is not considered, both assumptions predict unbounded particle velocity or acceleration, which is the source of numerical instability. This relationship between the particle boundness and numerical stability will be discussed in details in this study. Meanwhile, the expression to compute critical time step and a simpler form for approximation will be covered, which is the first goal. A step further, we can see that, if the relaxation process approaching to the equilibrium can be given analytically, the time step constraints will be gone immediately. This is the concept of the so-called relaxing scheme. The interpretation of this scheme will be detailed in Section 5.3, and its key idea is to derive the self-bounded analytical solutions for the drag force terms in both DEM and CFD solvers.

After the derivation, the approximation of the critical time step and the bounded solutions for the drag force terms will be verified individually for DEM and CFD solvers. Without using the relaxing scheme, both DEM and CFD shows the time step constraints from the exchanged drag force as expected. On the contrary, the simulation given the relaxing scheme allows a time step 2 orders larger for both DEM and CFD sides without sacrificing accuracy. However, the simulation result shows that's not the limit of the relaxing scheme because the other numerical assumptions become the bottleneck when the time step is large. Anyway, it proves that the relaxing scheme can enlarge the drag-induced critical time step greatly so that it is neglectable in determining the time step of the simulation system.

The main work of this chapter will be presented in 5 parts. In section 5.2, the drag-induced time step constraints will be analysed and expressions are given for DEM and CFD solvers. In Section 5.3, the solutions to interpret the relaxing scheme will be detailed for both DEM and CFD solvers. The case verification in terms of accuracy is to be given by Section 5.4, and a demonstration for the complex case is given in Section 5.5 to show the potential of the relaxing method. In the end, the conclusion is given in the last section.

5.2 Critical time step

5.2.1 Four sources of critical time step

The critical time step is one of the many inherent stability criteria of numerical methods. For a pure CFD case, different conditions can affect the determination of its critical time step. For example, a system approaching a steady state can bear a relatively large time step, the solver based on Forward Euler Scheme needs to meet the CFL condition, the multiphase flow with high density ratio also requires the CFL condition to capture a smooth interface. The more detailed discussion won't be covered in this study and it is denoted by Δt_f in the following. For a pure DEM case, the critical time step is controlled by the particle collision process, it will be denoted by Δt_p^C.

When CFD and DEM are coupled, one extra critical time step will be introduced to each of the two solvers. Let's denote the former by Δt_f^D, and the latter by Δt_p^D. The detailed derivation for their exact value and their approximation can be found in the next section.

Coming back to the determination of the stepping scheme of each solver, they can be given by the following two expressions:

(1) the step size of CFD part: $\Delta t_{CFD} \leq min\left(\Delta t_f, \Delta t_f^D\right)$;

(2) the step size of DEM part: $\Delta t_{DEM} \leq min\left(\Delta t_p^C, \Delta t_p^D\right)$.

5.2.2 Derivation of the drag-induced critical time step

Critical time step of DEM

In this section, the analysis of the critical time step starts from the simpler DEM solver. At the first step, let's rewrite the governing equation Eqn.3.5 as:

$$\boldsymbol{F} = m_p \frac{d v_p}{dt} = \boldsymbol{F}_d + \boldsymbol{f} \tag{5.1}$$

where $\boldsymbol{F}$ is the translational total force on the particle, $\boldsymbol{F}_d$ is the drag force, and $\boldsymbol{f}$ is the summation of all other forces except the drag force. In DEM, $\boldsymbol{F}$ and $\boldsymbol{u}_f$ are assumed to be constant in each time step, and the $\boldsymbol{v}_p$ is to be solved. Particle motion in this period can be interpreted by such a scenario: a particle is moving in an infinite space filled with the constant fluid flow (constant $\boldsymbol{u}_f$), and is subjected to a constant external force $\boldsymbol{f}$. In reality, we know that this particle will gradually change its velocity approaching a terminal velocity $\boldsymbol{v}_p^\infty$, where the $\boldsymbol{F}_d$ balances $\boldsymbol{f}$ and the particle is in equilibrium. So, it is obvious that the constant assumption of $\boldsymbol{F}_d$ is only valid if the time step is small enough. Otherwise, the overshooting of $\boldsymbol{F}_d$ will cause numerical oscillation or even divergence. This critical point is the target of further discussion.

In every time step, the state of an individual particle can be described by Fig.5.1, where $\boldsymbol{v}_{pf}$ is the relative velocity equaling to $\boldsymbol{u}_f - \boldsymbol{v}_p$, and $\boldsymbol{F}_d^\infty$ is drag force at equilibrium. The superscript ∞ means that the process of a particle approaching the equilibrium last infinitely. Initially, the particle is subjected to the force $\boldsymbol{f}$ and has a velocity $\boldsymbol{v}_p$. The fluid velocity is $\boldsymbol{u}_f$, so the drag force $\boldsymbol{F}_d$ can be determined accordingly. Under this condition, the particle relative velocity will always change approaching the $\boldsymbol{v}_{pf}^\infty$ which is irrelevant to the time scale. Alternatively, this process can be mathematically described by Eqn.5.2, which is the key condition of the whole work.

$$\lim_{t\to\infty} \boldsymbol{F}_d + \boldsymbol{f} = \left(k_d \boldsymbol{v}_{pf}\right)^\infty + \boldsymbol{f} = 0 \tag{5.2}$$

Based on the DEM assumption of constant drag force $\boldsymbol{F}_d$, Fig.5.2 describes the evolution of $\boldsymbol{v}_{pf}$ in time step i. At the beginning of time step i, relative velocity is $\boldsymbol{v}_{pf}^i$, the other forces are given by $\boldsymbol{f}^i$ and the particle acceleration is $\boldsymbol{a}_{pf}^i$ as given by Eqn.5.3.

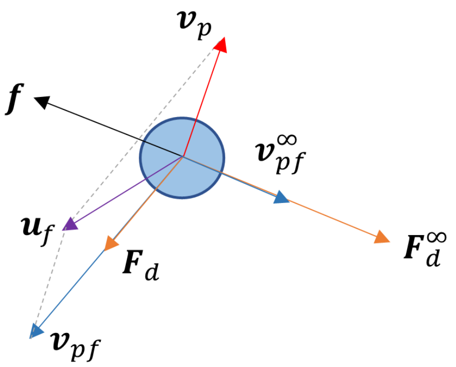

Fig. 5.1 State of a particle

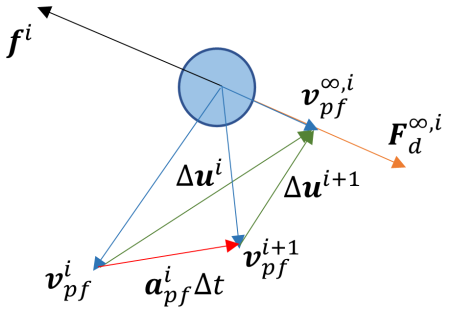

Fig. 5.2 Definition of weak criterion

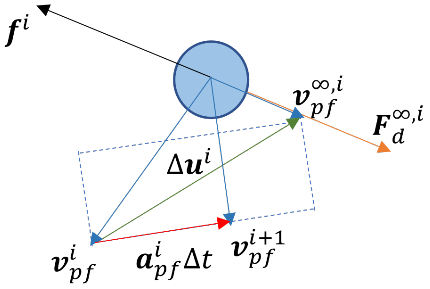

Fig. 5.3 Definition of strong criterion

$$\boldsymbol{a}_{pf}^i = \left[\frac{d\left(\boldsymbol{u}_f^i - \boldsymbol{v}_p\right)}{dt}\right]^i = -\left(\frac{d\boldsymbol{v}_p}{dt}\right)^i = -\frac{\boldsymbol{F}^i}{m_p} \tag{5.3}$$

The $\boldsymbol{a}_{pf}^i$ given by above this equation is bounded, and the resulting $\boldsymbol{v}_{pf}^{i+1}$ may overshoot the terminal velocity $\boldsymbol{v}_{pf}^{\infty}$ if time step Δt is too large. To avoid this situation, two different criteria can be proposed for the time step by involving a new parameter: the velocity distance $\Delta\boldsymbol{u}$. It's defined as the different between current relative velocity and terminal relative velocity given as $\Delta\boldsymbol{u} = \boldsymbol{v}_{pf}^{\infty,i} - \boldsymbol{v}_{pf}$. The first criterion can be described as the following: relative velocity at the end of a step should be closer to the terminal velocity compared with the beginning:

$$\left|\Delta\boldsymbol{u}^{i+1}\right| < \left|\Delta\boldsymbol{u}^i\right| \tag{5.4}$$

Expand this inequation, the following is obtained:

$$\Delta t < 2\frac{\boldsymbol{a}_{pf}^{i}}{\left(\boldsymbol{a}_{pf}^{i}\right)^{2}} \cdot \left(\boldsymbol{v}_{pf}^{\infty,i} - \boldsymbol{v}_{pf}^{i}\right). \tag{5.5}$$

It is considered as a weak criterion because the mode of $\Delta\boldsymbol{u}$ is used. It allows overshooting in velocity which means $\boldsymbol{v}_{pf}^{i+1}$ could locate on the other side of $\boldsymbol{v}_{pf}^{\infty}$ in Fig.5.2. Although this criterion leads to convergence, it introduces the oscillation which requires time to be dissipated. As an improvement, a strong criterion can be proposed to avoid the oscillation (Fig.5.3): $\left|\boldsymbol{a}_{pf}^{i}\right| \Delta t$, which is the increment in $\boldsymbol{v}_{pf}^{i}$, should be less than the projection of $\Delta\boldsymbol{u}^{i}$ on $\boldsymbol{a}_{pf}^{i}$. The mathematical expression is given by

$$\left|\boldsymbol{a}_{pf}^{i}\right| \Delta t < \Delta\boldsymbol{u}^{i} \cdot \frac{\boldsymbol{a}_{pf}^{i}}{\left|\boldsymbol{a}_{pf}^{i}\right|} \tag{5.6}$$

Expanding this inequation, Eqn.5.7 can be obtained.

$$\Delta t < \frac{\boldsymbol{a}_{pf}^{i}}{\left(\boldsymbol{a}_{pf}^{i}\right)^{2}} \cdot \left(\boldsymbol{v}_{pf}^{\infty,i} - \boldsymbol{v}_{pf}^{i}\right) \tag{5.7}$$

It's noted that the right-hand side of Eqn.5.7 is exactly the half of the Eqn.5.5. Assuming the right-side of Eqn.5.7 equals to Δt_d, the weak and strong criteria can be rewritten as Eqn.5.8.

$$\begin{cases} \Delta t < 2\Delta t_d, \quad \textit{weak criterion} \\ \Delta t < \Delta t_d, \quad \textit{strong criterion} \\ \Delta t_d = \frac{\boldsymbol{a}_{pf}^{i}}{\left(\boldsymbol{a}_{pf}^{i}\right)^{2}} \cdot \left(\boldsymbol{v}_{pf}^{\infty,i} - \boldsymbol{v}_{pf}^{i}\right) \end{cases} \tag{5.8}$$

The right hand side terms of the inequations represent the critical time step of DEM, and both of them can be evaluated by Δt_d. Bring Eqn.5.3 into Eqn.5.8, Δt_d can be rearranged as Eqn.5.9 shows.

$$\Delta t_d = -t_p \frac{\boldsymbol{f}^{i}/k_d^{i} + \boldsymbol{v}_{pf}^{i}}{\left(\boldsymbol{f}^{i}/k_d^{i} + \boldsymbol{v}_{pf}^{i}\right)^{2}} \cdot \left(\boldsymbol{v}_{pf}^{\infty,i} - \boldsymbol{v}_{pf}^{i}\right) \tag{5.9}$$

$$t_p = m_i/k_d^{i} \tag{5.10}$$

where, m_i is the mass of particle i. It's noted that t_p is constant part in the expression, and Δt_d equals to t_p exactly when $\boldsymbol{f}^i$ is 0. To demonstrate the validation of the two criteria, a 1D case is used: the background fluid has a constant velocity 0.001 m/s, and the particle starts moving from velocity 0; the densities of fluid and particle are 1000 and 2500 kg/m^3 respectively, fluid viscosity is 0.1 $Pa \cdot s$ and particle diameter is 0.001 m; there is no other forces acting on the particle. As the drag force is the only force, the particle velocity will gradually approach to the fluid velocity. Referring to Eqn.5.9, as k_d is a variable depending on $\boldsymbol{v}_{pf}$, Δt_d is velocity-dependent too. Using the Di Felice model for the drag force, the minimum value of Δt_d can be computed which equals 1.389×10^{-3} s. In total, 5 different time steps are used to simulate the particle motion including 1×10^{-3}, 1.389×10^{-3}, 2×10^{-3}, 2.819×10^{-3} and 3×10^{-3} s. The second and fourth time steps equal to Δt_d and $2\Delta t_d$ respectively. The simulation result is presented in Figure 5.4, and it matches exactly with our expectation.

(1) For the time step 1×10^{-3} s, as it is less than Δt_d, it generated a smooth curve without any oscillation;

(2) For the time step 1.389×10^{-3} s, the particle velocity reached the terminal velocity in one step which matches the definition of the strong criterion;

(3) For the time step 2×10^{-3} s, its value is between Δt_d and $2\Delta t_d$, and the curve shows oscillation at the initial several steps but still converges to the right terminal velocity which proves the validation of the weak criterion;

(4) For the time step 2.819×10^{-3} s, which equals to $2\Delta t_d$, the curve is oscillating around the terminal velocity and the amplitude keeps constant showing a trend of neither divergence nor convergence, which matches exactly with the definition of the weak criterion.

(5) For the time step 3×10^{-3} s, the result diverged in several steps as the amplitude of oscillation accumulated quickly.

According to this case, we can find that the strong criterion is always preferred as it is oscillation free. If $k_d^{\infty,i} \approx k_d^i$ which means the perturbation is mild, the Eqn.5.11 can be obtained, which is often true between two time steps. So, t_p can be used to approximate the critical time step.

$$\Delta t_d \approx t_p \tag{5.11}$$

What's more, for a sphere in Stokes' flow, k_d can be simplified to the expression $3\pi\mu d$ which is a constant. According to Eqn. 5.10, t_p for Stokes flow can be greatly simplified,

$$t_p^S = \frac{\rho_p d^2}{18\widetilde{\mu}} \tag{5.12}$$

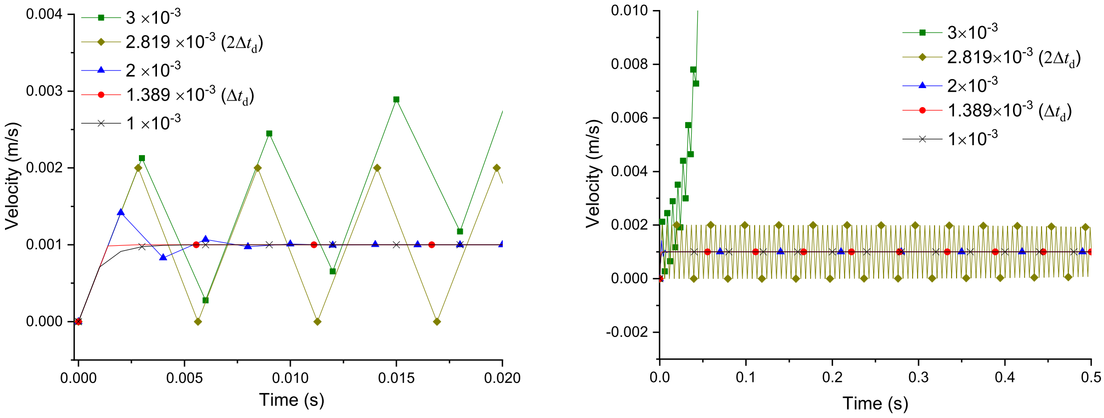

(a) Particle velocity in 0.02 s

(b) Particle velocity in 0.5 s

Fig. 5.4 Evolution of particle velocity: CFD critical time step demonstration

where t_p^S denotes the t_p of Stokes flow, $\widetilde{\mu}$ is apparent mixture viscosity which considers the effect of the surrounding particles. This is the so-called particle relaxation time, which is a characteristic time describing how fast a particle could relax itself to a perturbation. If it's a dilute mixture, $\widetilde{\mu}$ can be approximated by the fluid viscosity. Then, we can see that t_p^S becomes a constant irrelevant to any variables, showing that it is the material feature of the fluid-particle system. So it would be practical to evaluate the magnitude of the critical time step for a dilute mixture by t_p^S. As in most applications, the influence of the volume fraction can not be ignored, t_p is essential for evaluation.

Critical time step of CFD

The above derivation is based on DEM assumptions, when coming to the CFD it would be more complicated. In the latter, the fluid velocity is the unknown variable to be solved, and its value depends on the choice of the time step. Because of the existence of fluid acceleration, the concept of terminal velocity is not applicable anymore. Instead, as will be proved in Section 5.3.2, the particle will approach a terminal acceleration which equals to the fluid acceleration at the equilibrium state. The derivation of the exact critical time step is quite complicated, however, a similar T_p can be obtained referring to Eqn.5.10:

$$T_p = \frac{M_p}{K_{fp}V_{cell}} \tag{5.13}$$

where M_p is total particle mass in cell i. Use $\boldsymbol{a}_f^i$ to denote the fluid acceleration in step i, then the following equation can be obtained according to Eqn.3.15:

$$\boldsymbol{F}_D(t) = K_{fp}V_{cell}(\boldsymbol{u}_f^i + \boldsymbol{a}_f^i t - \langle \boldsymbol{v} \rangle^i) \tag{5.14}$$

where $\boldsymbol{F}_D(t)$ is the total drag force in a certain CFD cell in step i. Here, all the particles in the same cell are treated as a big virtual particle, which is assumed to have a uniform acceleration $\langle \boldsymbol{a} \rangle$ and jerk $\langle \dot{\boldsymbol{a}} \rangle$. Then, following the above discussion, two similar criteria can be deduced.

$$\begin{cases} \Delta t < 2\Delta T_d, & weak\ criterion \\ \Delta t < \Delta T_d, & strong\ criterion \\ \Delta T_d = \frac{\dot{\boldsymbol{a}}_{pf}^i}{(\dot{\boldsymbol{a}}_{pf}^i)^2} \cdot (\boldsymbol{a}_{pf}^\infty - \boldsymbol{a}_{pf}^i) \end{cases} \tag{5.15}$$

where the subscript pf means the difference between fluid and particle. The weak criterion indicates that the particle acceleration should approach the terminal value. While the strong criterion requires that the particle acceleration at the end of a step should not overshoot the terminal velocity. From section 5.3.2, it's known that particle acceleration catches up with the fluid at the equilibrium, which means

$$\boldsymbol{a}_{pf}^\infty = \boldsymbol{a}_f^i - \langle \boldsymbol{a} \rangle^\infty = 0 \tag{5.16}$$

where $\langle \boldsymbol{a} \rangle^i$ denotes the particle acceleration at the beginning of step i. While, for the relative acceleration at the begin of step i can be computed by:

$$\boldsymbol{a}_{pf}^i = \boldsymbol{a}_f^i - \langle \boldsymbol{a} \rangle^i = \boldsymbol{a}_f^i - \frac{\boldsymbol{F}_D(t)|_{t=0} + \boldsymbol{f}^i}{M_p^i} = \boldsymbol{a}_f^i - (\frac{\boldsymbol{u}_f^i - \langle \boldsymbol{v} \rangle^i}{T_p^i} + \frac{\boldsymbol{f}^i}{M_p^i}). \tag{5.17}$$

Here, $\boldsymbol{f}^i$ means the summation of forces other than drag on all particles in the same cell. The relative jerk $\dot{\boldsymbol{a}}_{pf}^i$ is given by:

$$\dot{\boldsymbol{a}}_{pf}^i = \frac{d\boldsymbol{a}_{pf}}{dt}|_{t=0} = -\frac{d\left[\boldsymbol{F}_D(t)/M_p^i\right]}{dt}|_{t=0} = -\frac{\boldsymbol{a}_f^i}{T_p^i} \tag{5.18}$$

which is a constant. Bring Eqn 5.16, 5.17 and 5.18 into Eqn. 5.15, ΔT_d is arranged as:

$$\Delta T_d = T_p^i \frac{\boldsymbol{a}_f^i}{(\boldsymbol{a}_f^i)^2} \cdot (\boldsymbol{a}_f^i - \frac{\boldsymbol{u}_f^i - \langle \boldsymbol{v} \rangle^i}{T_p^i} - \frac{\boldsymbol{f}^i}{M_p^i}) = T_p^i [1 - \frac{\boldsymbol{a}_f^i \cdot \langle \boldsymbol{a} \rangle^i}{(\boldsymbol{a}_f^i)^2}]. \tag{5.19}$$

Again, it is indicated that ΔT_d can be evaluated by the relaxation time T_p^i. If the particle acceleration is comparably small, ΔT_d approximates to T_p^i. However, when $\langle \boldsymbol{a} \rangle^i$ is close to

$\boldsymbol{a}_f^i$, it is noticed that the value of $(1-\frac{\boldsymbol{a}_f^i\cdot\langle\boldsymbol{a}\rangle^i}{(\boldsymbol{a}_f^i)^2})$ will approach to 0. In some cases, it is even possible to become negative, which makes the criteria in Eqn.5.15 never established. This is resulted from the implementation of drag force given in Eqn.3.14 which assumes K_{fp} and $\langle\boldsymbol{v}\rangle$ to be constant in every CFD step. Based on these assumptions, it is inevitable to predict an overshot fluid velocity in these extreme cases. But, it should be stated: the violation of Eqn.5.15 does not necessarily mean the divergence of CFD solver but an overestimated fluid velocity. Once this value is passed to the DEM, no matter how small the DEM time step is, the error is to be inherited by its updated particle velocity which is then returned to the CFD solver. As time pushes forward, this error will accumulate over time dramatically if the CFD criterion is violated. Usually, the unphysical phenomenon is observed from the DEM side: the particle is oscillating with a quickly increasing magnitude. When the particle velocity grows extremely large, it also could lead to the divergence of CFD.

To verify the derivation, the case used in Section 5.2.2 will be expanded involving the CFD solver, and the open-source package *CFDEM* is applied to carry out simulations. The long channel as shown in Figure 5.5 is modelled as the fluid domain. Its length, height and depth are 1 m, 0.1 m and 0.1 m respectively. The fluid flows in the channel at a fixed velocity 0.001 m/s from the left face and then flows out at the right face where the pressure is 0. The other faces are slip walls, so the fluid domain will reach a steady state where the majority space has the same velocity 0.001 m/s. The particle is released at a velocity 0, and the fluid and particle use the material properties as given in the last section. Thus, similarly, the particle velocity will gradually approach the fluid velocity 0.001 s. Here the value of ΔT_d is approximated by T_p^i which gives 1.38×0^{-3} s. For ΔT_d, as there is only one particle in this system, its value equals to Δt_d, which is also 1.38×0^{-3} s. In the simulation, several time steps were used for CFD solver which were 5×10^{-4}, 1×10^{-3}, 1.389×10^{-3}, 2×10^{-3} and 2.819×10^{-3}. On the DEM side, the time step is 10 times smaller than CFD, which is sufficient to satisfy the DEM time step criterion as proved in the last section.

In the running, it was found that CFD converges well in every step and only one case failed because the particle was out of the domain. Therefore, the result of this case will also be presented by the particle motion which is given in Figure 5.6. In the figure, only the time step of CFD is shown in the legend and the corresponding quantities of DEM are one-tenth of them.

(1) Both 5×10^{-4} and 1×10^{-3} cases generate a smooth curve;

(2) When time step equals to ΔT_d, the oscillation is observed in the initial steps;

(3) For the case 2×10^{-3} which is between ΔT_d and $2\Delta T_d$, the oscillation is large but it disappears quickly and converges to terminal velocity;

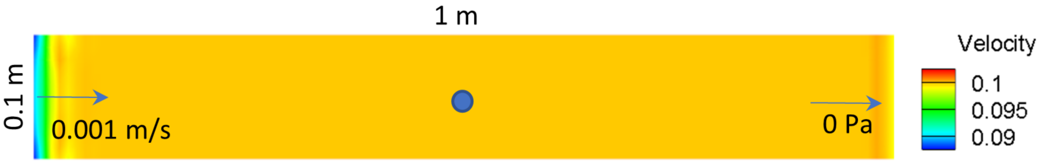

Fig. 5.5 Evolution of particle velocity: CFD critical time step demonstration

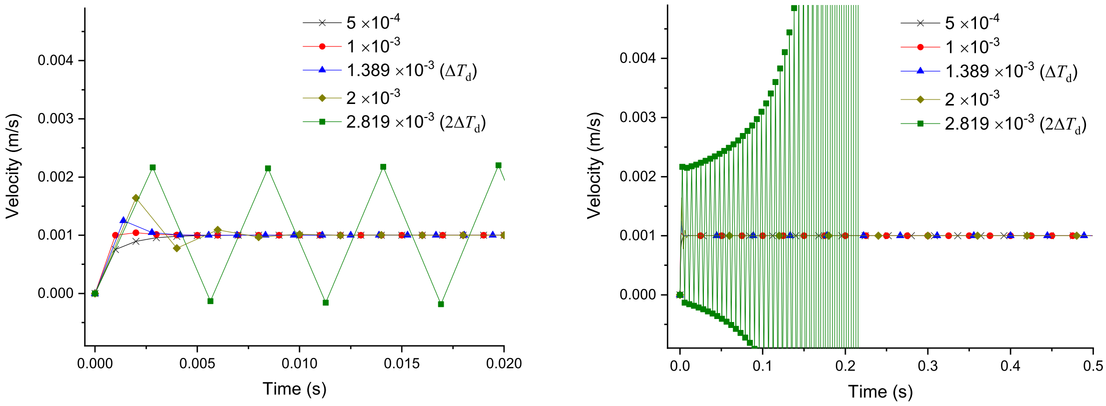

(a) Particle velocity in 0.02 *s*

(b) Particle velocity in 0.5 *s*

Fig. 5.6 Evolution of particle velocity given by different time step sizes

(4) When time step equals to $2\Delta T_d$, the curve keeps oscillating around the terminal velocity, but the amplitude is growing over time which leads to divergence at last;

(5) Comparing the plots in Figure 5.4, the oscillation and divergence start to appear in smaller time step cases in this case.

The above analysis shows that the real ΔT_d is a bit smaller than T_p^i. For the particle, it is accelerated gradually in the whole process. At the same time, when the particle moved to a new position, as it decreases the cross-sectional area, the averaged local fluid field is also accelerated. As the two are in the direction, the value of $(1 - \frac{\boldsymbol{a}_f^i \cdot \langle \boldsymbol{a} \rangle^i}{(\boldsymbol{a}_f^i)^2})$ is less than 1. As a result, the real ΔT_d is always smaller than T_p^i. However, it still strongly proves that T_p^i is a very good parameter to evaluate the maximum time step. What's more, the slight difference between ΔT_d and T_p^i implies that the $\boldsymbol{a}_f \ll \langle \boldsymbol{a} \rangle$.

As a conclusion, to promise the accuracy and numerical stability, the time step criteria given in Eqn.5.15 must be satisfied in determining the CFD time step. The exact value of critical step size is a variable dependent on the fluid and particle state. But, the relaxation time T_p^i is a good parameter to evaluate its magnitude. What's more, it's noticed that if the particle velocities in one cell are close to each other, T_p will degrade to t_p. Thus, t_p^S is also a rough evaluation for the CFD time step if the mixture is dilute. However, for a complicated flow process involving a large group of particles, the flow of both fluid and particles will be in chaos, and a trial is always required to determine the final step size.

5.3 Relaxing scheme

In the last section, the existence of drag-induced time step criteria for both CFD and DEM solvers is demonstrated. From the derivation, we can find that the source of these two criteria is the various unbounded low-order assumptions of drag force implementation. In DEM, the drag force in a step is assumed to be constant, so is the particle acceleration. In CFD, the drag force is assumed to be linear to the fluid velocity change. Although the accuracy is an order higher, the drag force is unbounded neither. So, it is natural to come up with the relaxing scheme: if the drag force implementation is self-bounded by the terminal state, the two step criteria will be gone. In other words, the relaxing scheme will try to recover or approximate the real relaxation process which would take infinite time. And, this is the task of this section to find the solutions for DEM and CFD to realize the relaxing scheme.

The criteria on time step due to drag can be explained in another perspective. As shown in Figure 5.7, the total force $\boldsymbol{F}$ in time step i is a function of relative velocity $\boldsymbol{v}_{pf}$ since $\boldsymbol{f}^i$ is assumed to be constant in both CFD and DEM solvers. Theoretically, all the 3 parameters are 3D vectors, and they can be in different directions. But for the purpose of easier presentation, this simple 1D form is to be used in the discussion of this section. The two variables ($\boldsymbol{F}$, $\boldsymbol{v}_{pf}$) together represent the state of a particle, and the black curve shows the path of a particle when particle velocity grows from 0 to ∞. If $\boldsymbol{v}_{pf}$ becomes 0, the drag force is 0 too, so $\boldsymbol{F}$ equals to $\boldsymbol{f}^i$. Let's assume, at the beginning of step i, the particle state locates on point A, where relative velocity is $\boldsymbol{v}_{pf}^i$ and the total force on the particle is $\boldsymbol{F}^i$. In reality, when a perturbation happened at this point, the particle state will follow the black curve and move to point B where the equilibrium is.

However, taking the DEM as an example, due to the constant $\boldsymbol{F}^i$ assumption, the path of particle state will go horizontally following the path 1 and 2. Again, according to constant assumption, the governing equation of particle motion in the step i can be given by Eqn.5.20 by referring to Eqn.5.3, and $\boldsymbol{v}_{pf}^{i+1}$ can be predicted by Eqn.5.21. If the time step of DEM matches the criterion which means the $\boldsymbol{v}_{pf}^{i+1}$ is less than $\boldsymbol{v}_{pf}^{\infty}$ (as path 1 shows), the predicted particle state ($\boldsymbol{v}_{pf}$, $\boldsymbol{F}$) in next step $i+1$ will not surpass point B. On the opposite, if the time step is too large (like path 2), the point ($\boldsymbol{v}_{pf}$, $\boldsymbol{F}$) in the figure will be on the other side of point B, which can cause oscillation or even divergence because of the unphysical overshooting. So, based on Fig.5.7, the drag-induced time step criterion for DEM can be interpreted in another way: the particle state should move within the range bounded by point A and B.

Following the thought of trace, different methods are to be proposed for CFD and DEM solvers. The key idea of both is to find an appropriate bounded path to relax the particle in Fig.5.7.

$$m_p \frac{d\boldsymbol{v}_{pf}}{dt} = \boldsymbol{F}_d^i + \boldsymbol{f}^i = m_p \boldsymbol{a}_p^i, \quad 0 < t < \Delta t \tag{5.20}$$

$$\boldsymbol{v}_{pf}{}^{i+1} = \boldsymbol{v}_{pf}{}^{i} - \boldsymbol{a}_p^i \cdot \Delta t \tag{5.21}$$

5.3.1 DEM solution

As shown in Fig.5.8, obviously the Path 3 is a perfect choice for the relaxing scheme: in time step i, the particle state follows a linear path from A towards B. It assumes that the increment of $\boldsymbol{F}$ (also $\boldsymbol{F}_d$) is linear to the increment of $\boldsymbol{v}_{pf}$. According to it, the particle state at any point on Path 3 (like D) can be given by:

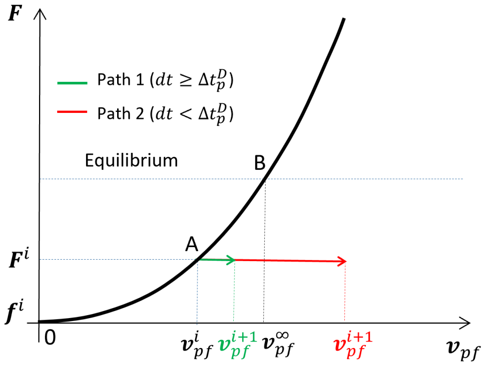

Fig. 5.7 unbounded assumption

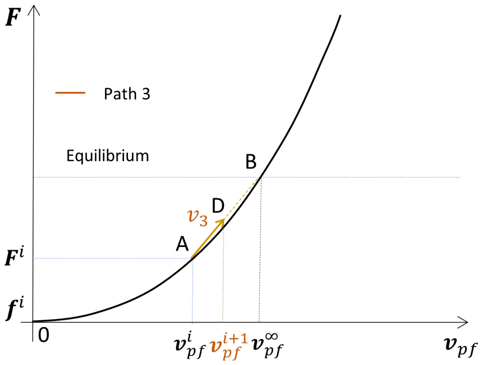

Fig. 5.8 two-sides-bounded assumption

$$\boldsymbol{F}_d - \boldsymbol{F}_d^i = \boldsymbol{K}_d \left(\boldsymbol{v}_{pf} - \boldsymbol{v}_{pf}^i \right) \tag{5.22}$$

where $\boldsymbol{K}_d^i$ is a transfer matrix in step i which indicates the linear relationship between two increments. Bring the particle state at point B the above equation, Eqn.5.23 is obtained:

$$\boldsymbol{F}_d^{\infty,i} - \boldsymbol{F}_d^i = \boldsymbol{K}_d \left(\boldsymbol{v}_{pf}^{\infty,i} - \boldsymbol{v}_{pf}^i \right) \tag{5.23}$$

Then the DEM governing equation Eqn.5.1 then can be rewritten as Eqn.5.24:

$$m_p \frac{d\boldsymbol{v}_p}{dt} = \boldsymbol{F}^i + \boldsymbol{K}_d \left(\boldsymbol{v}_{pf} - \boldsymbol{v}_{pf}^i \right) \tag{5.24}$$

Supposing the case is 3D, $\boldsymbol{K}_d^i$ is a 3×3 matrix containing 9 unknown elements. But Eqn.5.23 provides only 3 equations, which is not enough to solve $\boldsymbol{K}_d$. Theoretically, there are numerous solutions for $\boldsymbol{K}_d^i$ since there are only two vectors $(\boldsymbol{F}_d^{\infty,i} - \boldsymbol{F}_d^i)$ and $(\boldsymbol{v}_{pf}^{\infty,i} - \boldsymbol{v}_{pf}^i)$, and the information of a third dimension is missing. So, to make $\boldsymbol{K}_d^i$ solvable, the original assumption is further modified as

$$\boldsymbol{F}_d = \boldsymbol{K}_d \boldsymbol{v}_{pf} \tag{5.25}$$

It means that the drag force can directly be transferred from relative velocity by $\boldsymbol{K}_d$. Thus, combing with Eqn.**??** into Eqn.5.25, the following two equations are obtained

$$\begin{cases} \boldsymbol{F}_d^{\infty,i} = k_d^{\infty,i} \boldsymbol{v}_{pf}^{\infty,i} = \boldsymbol{K}_d \boldsymbol{v}_{pf}^{\infty,i} \\ \boldsymbol{F}_d^i = k_d^i \boldsymbol{v}_{pf}^i = \boldsymbol{K}_d \boldsymbol{v}_{pf}^i \end{cases} \tag{5.26}$$

where $k_d^{\infty,i}$ is the coefficient k_d at point B in step i. The two equations means that k_d^i and k_d^∞ are two eigenvalues of $\boldsymbol{K}_d$, and $\boldsymbol{v}_{pf}^i$ and $\boldsymbol{v}_{pf}^\infty$ are two eigenvectors of $\boldsymbol{K}_d$. In addition, the drag force and relative velocity are in the same direction which means the 4 vectors $\boldsymbol{v}_{pf}^i$, $\boldsymbol{v}_{pf}^\infty$, $\boldsymbol{F}_d^i$ and $\boldsymbol{F}_d^\infty$ are in the same plane. Thus, according to the linear assumption stated at the beginning, the relative velocity and drag force on the proposed path 3 should be in the same plane too. All that information indicates the third eigenvector of $\boldsymbol{K}_d$ does not contribute to the final solution, which is to be ignored.

Bring Eqn.5.2 and Eqn.5.25 into Eqn.5.1, $\boldsymbol{F}^i$ can be expanded as

$$\boldsymbol{F}^i = \boldsymbol{F}_d^i - \boldsymbol{f}^i = \boldsymbol{F}_d^i - \boldsymbol{F}_d^{\infty,i} = \boldsymbol{K}_d \left(\boldsymbol{v}_{pf}^i - \boldsymbol{v}_{pf}^{\infty,i} \right) \tag{5.27}$$

Bring it into Eqn.5.24, the governing equation can be rewritten as:

$$m_p \frac{d\boldsymbol{v}_p}{dt} = \boldsymbol{K}_d \left(\boldsymbol{v}_{pf} - \boldsymbol{v}_{pf}^{\infty,i} \right) \tag{5.28}$$

Using the eigenvalues and eigenvectors, the solutions for particle velocity and displacement can be obtained:

$$\boldsymbol{v}_p(t) = \boldsymbol{v}_f^i - e^{-t/t_p^i} \cdot \boldsymbol{v}_{pf}^i - \left(1 - e^{-t/t_p^{\infty,i}}\right) \boldsymbol{v}_{pf}^{\infty,i} \tag{5.29}$$

$$\Delta \boldsymbol{r}(t) = \boldsymbol{v}_f^i t - t_p \left(1 - e^{-t/t_p^i}\right) \cdot \boldsymbol{v}_{pf}^i + t_p \left[\left(1 - e^{-t/t_p^{\infty,i}}\right) - \frac{t}{t_p} \right] \boldsymbol{v}_{pf}^{\infty,i} \tag{5.30}$$

where t is duration counting from the beginning of step i, and $\Delta\boldsymbol{r}$ is the particle displacement in step i. It indicates that particle velocity is the combination of fluid velocity, initial relative velocity and terminal relative velocity. If t is replaced by Δt, the left hand sides of the two equations represent $\boldsymbol{v}_p^{i+1}$ and $\Delta\boldsymbol{r}^i$. If t is 0, $\boldsymbol{v}_p$ equals to $\boldsymbol{v}_p^i$ and $\Delta\boldsymbol{r}$ is 0. If t is far larger (such as 3 times) than t_p^i and t_p^∞, $\boldsymbol{v}_p$ approximates to $\boldsymbol{v}_p^\infty$. So, this solution matches very well with the initial purpose of the relaxing scheme. In addition, it's noticed that the parameter t_p shows up in the index of exponential term, and it acts as a scale describing how fast the particle could relax itself to the equilibrium state. This is in accordance with the derivation in Section 5.2.2.

At last, there is also an inevitable compromise in applying this method. As the Eqn.**??** indicates, theoretically, the drag force is always in the same direction of relative velocity. However, according to the assumption Eqn.5.25, this condition is satisfied only on two boundary points A and B because the number of eigenvector in one plane is no more than 2. For any point in between, a non-zero angle exists between approximated drag force and relative velocity. However, as the time step is small, such an error is very small. And, this method has a high-order accuracy which will be verified by a case study in the later section.

5.3.2 CFD solution

As given in Section 3.3.1, the particle velocity $\langle\boldsymbol{v}\rangle$ and K_{fp} are assumed to be constant for drag force term in CFD. Its limitation on the time step size Δt can be analyzed by the aid of Fig.5.9. Because the fluid-particle interaction is implemented according to all the particles in each FVM cell, the meanings of $\boldsymbol{v}_{pf}$, $\boldsymbol{f}$ and $\boldsymbol{F}$ are different with those in Fig.5.7 and Fig.5.8. Here, $\boldsymbol{F}$ denotes the total force on all particles in the cell, $\boldsymbol{f}$ is the total force excluding drag on all particles and $\boldsymbol{v}_{pf}$ is relative velocity given by $\boldsymbol{u}_f - \langle\boldsymbol{v}\rangle$. Still, point A is used to represent the initial particle state in step i and B is used for the equilibrium state. The new point C is for the predicted state at the end of step i, and the point C' is the intersection of path AC and equilibrium line. According to Eqn.3.14, the particle state locates on the line linking point A and the origin, and K_{fp} equals to the slope of this line. Because $\langle\boldsymbol{v}\rangle$ is constant, the increment ($\Delta\boldsymbol{v}_{pf}$) of $\boldsymbol{v}_{pf}$ equals to the increment ($\Delta\boldsymbol{u}_f$) of $\boldsymbol{u}_f$. The direction of $\Delta\boldsymbol{u}_f$ is determined by the momentum equation Eqn.3.2. Concluded from above information, two issues appear.

(1) The drag force term $\boldsymbol{R}_{pf}$ is unbounded. As Eqn.3.14 implies, if Δt is too large, the $\boldsymbol{u}_f$ may change too much and lead to an unreasonable $\boldsymbol{R}_{pf}$. What's more, if K_{fp} is very large such as large fluid viscosity or particle volume fraction, $\boldsymbol{R}_{pf}$ will be very sensitive to the change in $\boldsymbol{u}_f$. The unbounded issue can lead to divergence;

(2) The influence of $\boldsymbol{f}$ is not considered. $\boldsymbol{f}$ is a very important parameter because it determines where the equilibrium line is in Figure 5.9. As the direction of $\Delta\boldsymbol{u}_f$ is random, it could go further from the equilibrium line. And, the further the distance is, the larger the particle acceleration will be in the next step. In this case, if Δt is too large, the ignorance of $\boldsymbol{f}$ will bring random error into $\boldsymbol{R}_{pf}$, which means the accuracy of $\boldsymbol{R}_{fp}$ is weakened.

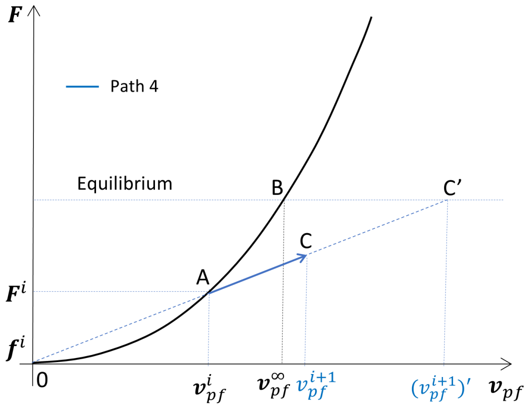

Fig. 5.9 force-bounded assumption

It's noted that the above two issues can be solved together by modifying the constant $\langle \boldsymbol{v} \rangle$ assumption: the particle group is treated as one bigger virtual particle which is allowed to relax its motion while fluid velocity changes. So the topic comes back to particle relaxation again. Similar to the idea of terminal velocity, the virtual particle would always gradually converge to a certain state if time is long enough. Such convergence could mean constant velocity, acceleration or other variables describing the particle state, which can be expressed mathematically by

$$\lim_{t \to \infty} \phi = \phi_{const} \tag{5.31}$$

where ϕ denotes the converged variable, and $\phi_c onst$ is the constant ϕ converges to. This point will be demonstrated for the CFD case as blow. Let's assume that the fluid velocity changes linearly within each step which gives:

$$\boldsymbol{a}_f^i = \frac{\boldsymbol{u}_f^{i+1} - \boldsymbol{u}_f^i}{\Delta t} \tag{5.32}$$

where $\boldsymbol{a}_f^i$ denotes fluid acceleration in time step i and $\boldsymbol{u}_f^{i+1}$ denotes the predicted fluid velocity of next step $i+1$. Then, theoretically, the governing equation of the virtual particle at the equilibrium state can be written as:

$$M_p^i \boldsymbol{a}_p(t) = K_{fp}\left(\boldsymbol{v}_{pf}\right) V_{cell} \boldsymbol{v}_{pf} + \boldsymbol{f}^i \tag{5.33}$$

$$\boldsymbol{v}_{pf} = \boldsymbol{u}_f - \langle \boldsymbol{v} \rangle^i + \int_0^t \left(\boldsymbol{a}_f^i - \boldsymbol{a}_p(t) \right) dt \tag{5.34}$$

where t is the time from the beginning of step i. To promise a converged terminal state, the following condition should be satisfied

$$\lim_{t \to \infty} \int_0^t \left(\boldsymbol{a}_f^i - \boldsymbol{a}_p(t) \right) dt = const \tag{5.35}$$

Otherwise, the relative velocity will become infinite which in turn makes $\boldsymbol{a}_p$ on the left side of Eqn.5.33 growing infinitely. That is impossible because $\boldsymbol{a}_p$ can't surpass the value of $\boldsymbol{u}_f^i$. One essential but not sufficient condition for Eqn.5.35 is given as:

$$\lim_{t \to \infty} \boldsymbol{a}_p = \boldsymbol{a}_f^i. \tag{5.36}$$

It means that at the terminal state, the particle acceleration will approach the fluid acceleration. Bringing this result back into Eqn.5.33, the converged drag force can be computed:

$$\boldsymbol{F}_D^\infty = M_p^i \boldsymbol{a}_f^i - \boldsymbol{f}^i. \tag{5.37}$$

The constant drag force at terminal stage also means a constant terminal velocity which is given by:

$$\boldsymbol{v}_{pf}^\infty = \frac{\boldsymbol{F}_D^\infty}{V_{cell} K_{fp}(\infty)} \tag{5.38}$$

The above discussion demonstrates that: in a fluid field of constant acceleration, the particle will approach the same acceleration if time is large enough. Knowing this point, the CFD solution for the relaxing scheme can be formulated based on the following 3 assumptions.

(1) The fluid velocity $\boldsymbol{u}_f$ changes linearly from $\boldsymbol{u}_f^i$ to the predicted $\boldsymbol{u}_f^{i+1}$ in the step i, which means the first-order scheme is used for transient term in Eqn.3.2.

(2) The position of the virtual particle doesn't change in one step. That means $\langle \boldsymbol{v} \rangle$ is only used to bound the drag force term $\boldsymbol{R}_{fp}$ but won't affect the DEM result.

(3) If Path 3 was applied, the mapping process of CFD and DEM has to be repeated iteratively to update the K_{pf}^∞. Thus, in this work, the Path 4 is used and the constant scalar K_{pf} is adopted to simplify the coupling.

Referring to the Fig.5.9, these assumptions allow the virtual particle to move the Path 4 which will start from Point A and approach to the Point C'. Certainly, a significant error could be observed in the value of $(\boldsymbol{v}_{pf}^{i+1})'$ because the relative velocity is unbounded. But, unfortunately, $\boldsymbol{v}_{pf}^\infty$ is unavailable because the determination of K_{fp}^∞ is such a tough work.

So, actually the Point B is unknown and only Point C' is available to us. In conclusion, the Path 4 for relaxing scheme provides a solution with self-bounded drag force. The governing equation of the virtual particle in step i is given by

$$M_p^i \frac{d\langle \boldsymbol{v} \rangle}{dt} = \left(K_{fp}^i V_{cell}\right)\left(\boldsymbol{u}_f^i + \boldsymbol{a}_f^i t - \langle \boldsymbol{v} \rangle\right) + \boldsymbol{f}^i \tag{5.39}$$

Accordingly, Eqn.5.40 and 5.41 are the boundary conditions given by $\boldsymbol{F}_D$ and $\langle \boldsymbol{v} \rangle$

$$\boldsymbol{F}_D^i = \left(K_{fp}^i V_{cell}\right)\left(\boldsymbol{u}_f^i - \langle \boldsymbol{v} \rangle^i\right) \tag{5.40}$$

$$\boldsymbol{v}_{pf}^i = \boldsymbol{u}_f^i - \langle \boldsymbol{v} \rangle^i \tag{5.41}$$

where $\boldsymbol{F}_D^i$ denotes the total drag force of all particles in the cell in step i. Then, the solution of Eqn.5.39 can be given by:

$$\langle \boldsymbol{v} \rangle = \langle \boldsymbol{v} \rangle^i e^{-t/T_p^i} + \left(1 - e^{-t/T_p^i}\right) \frac{\boldsymbol{f}^i}{\left(K_{fp}^i V_{cell}\right)} + \left[t - T_p^i \left(1 - e^{-t/T_p^i}\right)\right] \boldsymbol{a}_f^i. \tag{5.42}$$

The parameter T_p^i is given by Eqn.5.13. Apparently, T_p is a also key parameter to evaluate the relaxing rate of particle group. Bring the solution into Eqn.3.14 and replace $\boldsymbol{a}_f^i$ by Eqn.5.32, $\boldsymbol{R}_{fp}$ is obtained by

$$\boldsymbol{R}_{fp} = \frac{1}{V_{cell}} \left[e^{-t/T_p^i} \boldsymbol{F}_D^i - \left(1 - e^{-t/T_p^i}\right) \boldsymbol{f}^i + M_p^i \left(1 - e^{-t/T_p^i}\right) \frac{\boldsymbol{u}_f^{i+1} - \boldsymbol{u}_f^i}{\Delta t}\right] \tag{5.43}$$

As this equation shows, $\boldsymbol{R}_{fp}$ is a function of initial total drag force $\boldsymbol{F}_D^i$, the total force $\boldsymbol{f}^i$ on particles (excluding drag force) and the acceleration of fluid $\boldsymbol{a}_f^i$. The term contains $\boldsymbol{u}_f^{i+1}$ can be treated in two ways. Firstly, it can be the value from the last iteration, which is a semi-implicit scheme. Secondly, it can be moved to the left-hand side of the momentum equation for velocity prediction, which is an implicit scheme. As Eqn.5.44 proves, $\boldsymbol{R}_{fp}$ will converge a certain value when t approaches to infinite. And when t equals to $3T_p^i$, $\boldsymbol{R}_{fp}$ will reach 95% of the converged value.

$$\lim_{t \to \infty} \boldsymbol{R}_{fp} = \frac{1}{V_{cell}} \left(-\boldsymbol{f}^i + M_P^i \frac{\boldsymbol{u}_f^{i+1} - \boldsymbol{u}_f^i}{\Delta t}\right) \tag{5.44}$$

Referring to the definition of $\boldsymbol{R}_{fp}$ in Eqn.3.14, the drag force $\boldsymbol{F}_D^{\infty}$ equals to $\boldsymbol{R}_{fp}V_{cell}$ which gives exactly the same result as Eqn.5.37. It demonstrates that the Point C' locates on the equilibrium line in Fig.5.9 which means the drag force is bounded by the accurate value. It proves that this solution satisfies the initial purpose.

5.4 Verification of the relaxing scheme implementations

Although the analytical solutions have been derived for both solvers, the verification is essential to show the improvement on maximum time step and investigate the possible error introduced. The work will start from the DEM part as it is easier in terms of solution implementation and result presentation. Because the fluid field is given explicitly in the DEM solver, instead of involving the CFD solver, several explicit expressions will be used to provide the fluid information. According to this idea, two different cases are designed for the two purposes respectively, which approves great performance of the relaxing scheme. Next, the solution for the CFD solver will be investigated by two different CFD-DEM codes which are the open-source package CFDEM and our in-house code. In the beginning, a case will be designed and run by CFDEM to determine the critical time step. Next, the same case will be run by our in-house code with the relaxing scheme implemented in both solvers. Comparing the two results from different codes, the relaxing scheme for the unresolved CFD-DEM approach works perfectly. In this discussion, the Di Felice drag model is also used for all cases.

5.4.1 Validation of solution for DEM solver

As mentioned, the DEM is the only involved solver in this section. To demonstrate the feasibility of the solution given in Eqn.5.29 and 5.30, a 1D case is used to approve the accuracy and a 3D case is used to show the potential in enlarging time step. Because the drag force is the only focus of this study, only one particle will be considered to avoid any possible particle collision. All the other forces will be represented by one force and will be given by explicit expression too. We can imagine that this particle is moving in a changing background fluid field and a certain external force is applied to it at the same time. Because this scenario is very simple, a code is developed to generate the particle trajectory from both the explicit scheme and the relaxing scheme. And the comparison will be done for the history of both particle velocity and position. For the explicit scheme, the former is obtained by solving the Eqn. 3.5 and the latter is integrated by the Euler scheme. While, for the relaxing scheme, the Eqn. 5.29 and 5.30 are used to update the particle velocity and position respectively.

In case one, the background fluid is constant as given in Table 5.1. The particle flows freely in the fluid and initial $\boldsymbol{v}_p$ is 0. Besides the drag force, there are no other fores acting on the particle. According to Eqn.5.10, the relaxation time t_p is $0.156\ s$. Under such condition, it's known that the particle will start acceleration to approach to the fluid velocity. As shown in Figure 5.10, 6 different time steps were used in the simulations of both schemes. Four ($0.0001\ s$, $0.001\ s$, $0.01\ s$, $0.1\ s$) were below the t_p, one ($0.01\ s$) was above t_p, and one ($0.2\ s$) was in between.

In Figure 5.10a from the explicit scheme, it is implied that a converged solution can be achieved for particle velocity when the time step is less than $0.01\ s$. The curve approaches the value $0.001\ m/s$ as expected, which is the fluid velocity. When the time step is $0.1\ s$ which is close to t_p, it shows a significant difference at the initial stage compared with the converged curve. However, it still approaches fluid velocity. For the time step $0.2\ s$ whose is between t_p and $2t_p$, the oscillation is observed as expected, which shows a trend of approaching the fluid velocity too. When coming to the Figure 5.10b using the relaxing scheme, great improvement can be observed. First, the relaxing scheme gives the same converged curve compared with the explicit scheme. It is not surprising to see that the 6 results all approach the terminal velocity as it is an embedded condition. Second and most importantly, all data points from 6 time steps are located on the converged curve. Especially for time step $0.1\ s$ and $0.2\ s$, their results fit perfectly on the converged curve. It proves that the solution given by Eqn. 5.29 has great accuracy to approximate the particle relaxation procedure. In terms of enlarging the time step, this simple case shows a growth of 100 times.

Similar conclusion can be obtained when comparing curves of particle position in Figure 5.10c and 5.10d. For the Euler scheme, the converged solution is achieved again when the time step is less than $0.01\ s$. And when the time step is $1\ s$, the particle has an extremely large displacement because of the greatly overshot velocity. However, the solution based on the relaxing method generates consistent results for all time steps, which proves its great advantages again.

Table 5.1 Configuration of 1D case for DEM solution verification

Parameter	$\boldsymbol{u}_f\ (m/s)$	$\mu\ (Pa \cdot s)$	$\rho_f\ (kg/m^3)$	$\rho_p\ (kg/m^3)$	$d\ (m)$	$t_p\ (s)$
Value	0.001	5×10^{-3}	1000	2500	0.001	0.156

Because Case 1 is very simple, to show the full potential of the relaxing scheme, a more complicated 3D case is designed as presented in Table 5.2. The fluid velocity, external force and fluid viscosity are given by random functions of time. The former two vectors are expressed by the multiply of a scalar function and a constant vector. The other parameters are all constant. The particle has a initial velocity $(-0.1, 1.05, 0.0)\ m/s$ from position $(0, 0, 0)\ m$.

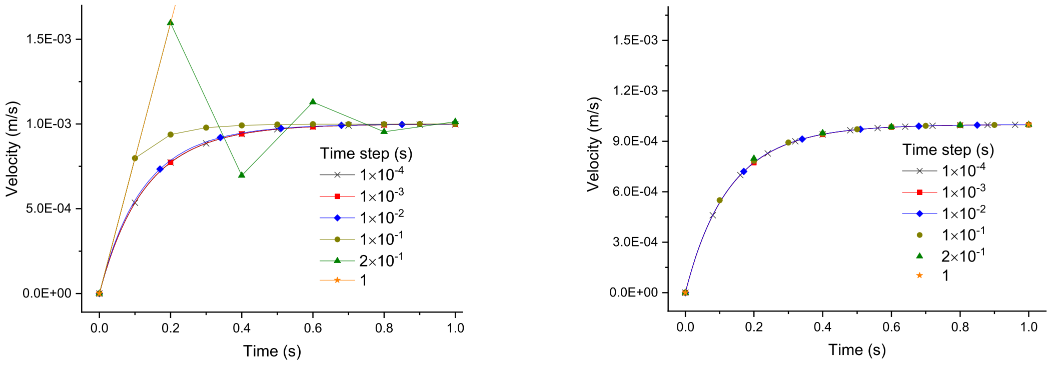

(a) Velocity history: explicit scheme (b) Velocity history: relaxing scheme

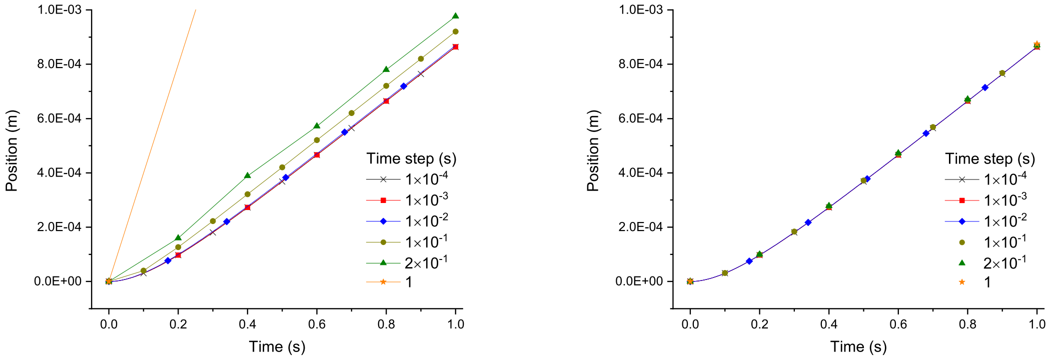

(c) Position history: explicit scheme (d) Position history: relaxing scheme

Fig. 5.10 case 1: 1D Comparison of velocity and position

In total, 1 s is simulated, and the corresponding relaxation time varies from $0.00028 \sim 0.14$ s due to the time-dependent viscosity. A similar comparison between particle velocity and position is presented in Figure 5.11 and 5.12, and the following points can be concluded.

(1) For explicit scheme, only time step 1×10^{-6} and 1×10^{-5} s provide converged curves. Although time step 1×10^{-4} s is less than the minimum t_p, the corresponding curve still diverged at time 0.982 s. That means the critical time step Δt_p^D is between 1×10^{-4} s and 1×10^{-5} s. However, t_p is still a good starting guess for the critical time step. When the time step becomes larger, the divergence appears earlier on the curve.

(2) For the relaxing scheme, every time step gives a converged result. For 4 curves with time step below 1×10^{-2} s, no gap can be observed visually between any two of them. While, for the time step 1×10^{-2} s, a slight difference is visible. When coming to the time step 1×10^{-1} s, the difference is enlarged significantly. Such an error is introduced by the coarse sampling on the time dimension when the time step is large, which is the inherent limitation of the numerical method.

(3) Comparing the two schemes, it's obvious that the relaxing scheme gives the same result as the explicit scheme, which approaches the accuracy. In addition, the relaxing scheme

gives an acceptable result for a large time step 1×10^{-2} s which is 100 times larger than the explicit scheme. Or we can say the relaxing method has pushed the time step to the upper limit of the numerical method.

Table 5.2 Configuration of 3D case for DEM solution verification

Parameter	$\boldsymbol{u}_f$ (m/s)	μ $(Pa \cdot s)$	$\boldsymbol{f}$ (N)	ρ_f (kg/m^3)	ρ_p (kg/m^3)	d (m)	α_f	t_p (s)
Value	$0.01 \cdot (1,1,1) + sin(\pi(t-0.5)) \cdot (0.61,-0.73,0.3)$	$0.1 + 9.9t + 40t^2$	$1.34m(t-1) \cdot (2.3,7,-1.2)$	1000	2500	0.01	0.5	$2.8 \times 10^{-4} \sim 0.14$

5.4.2 Validation of solution for CFD solver

Case setup and critical time step

In this section, a square-sectional bent pipe will be used to demonstrate the performance of the solution for the CFD solver. Its dimension is presented in Figure 5.13. A thick fluid with high viscosity is flowing into the pipe from the bottom at a fixed velocity 0.1 m, and the top right face has a fixed pressure. All the other boundaries are no-slip walls. The configuration of this case is concluded in the Table 5.3. Firstly, as a test, a pure CFD simulation was run by $OpenFOAM$ and a steady flow was achieved as shown in Figure 5.14.

Table 5.3 Configuration of square-section bent pipe

Parameter	ρ_f (kg/m^3)	μ $(Pa \cdot s)$	Velocity inlet (m/s)	Pressure outlet (Pa)	ρ_p (kg/m^3)	d (m)	T_p (s)
Value	1000	10	0.1	0	2400	0.001	1.37×10^{-5}

Then, in a new case, a small particle of size 0.001 m is placed at the position (0.1 m, 0.1 m, 0.5 m) which is the center of the vertical part of the pipe. This case was run by the $CFDEM$ repeatedly with different time steps to investigate the failure caused by the CFD solver. For DEM, t_p can be computed easily which is 1.37×10^{-5} s. And in this case, because there is only one particle, T_p equals to t_p which is also 1.37×10^{-5} s. A batch of combinations (CFD / DEM) of time steps was designed, and the simulations were carried out by $CFDEM$. The result is represented by the particle trajectory in Figure 5.15 including the sub-figures for the history of particle X coordinate and Z coordinate. The two cases (1×10^{-5}, 1×10^{-6}) and (1×10^{-5}, 1×10^{-5}) were run at the beginning, and they gave the converged result, which approves again the derivations in Section **??**. In the next 3 cases, to avoid any stability concern from the DEM side, the smaller time step 1×10^{-6} was used.

When the CFD time step grows larger than $2T_p$, the divergence started to appear from the case 5×10^{-5} as expected. This case shows that the time step choice of $CFDEM$ is limited by the drag-induced time step criteria.

Validation of the relaxing scheme

The last section shows how the simple implicit drag force implementation failed in the bent pipe case. As a comparison, an in-house code, where the solutions of relaxing scheme are implemented for CFD and DEM solvers, will be used to run the same bent pipe case. But, before carrying out that simulation, the performance of this code should be validated which can be done by comparing the $CFDEM$. For this purpose, the case is designed as: step sizes (1×10^{-5}, 1×10^{-5}) are used and the total simulated time is 5 s during which the particle was transported from vertical pipe to top horizontal part. The particle trajectory given by two codes is plotted in Figure 5.16a. In addition, because the relaxation time is so small, the particle trajectory followed the streamline of the steady flow in the whole process as shown in Figure 5.16b. In conclusion, the perfect match of the simulation results demonstrates the validation of our in-house code.

Then, another 4 cases were carried out: both CFD and DEM solvers used the same time step including 10^{-4}, 10^{-3}, 10^{-2} and 1×10^{-1} s. The result of the 4 cases is still presented by the particle trajectory in X and Z directions (Figure 5.17). Besides, as a validation of accuracy, the converged result given by $CFDEM$ is plotted together. There is a significant difference observed in the case 10^{-1} s, but the other 4 curves match each other very well. For the case 10^{-1} s, the difference started to grow when the particle entered the bent part. Due to the large time step of this case, the fluid velocity was refreshed at a low frequency in the DEM solver so that the particle moved gradually away from the original streamline. So, this error is from the intrinsic limitation of the numerical method but not the relaxing scheme. In conclusion, the result in Figure 5.17 strongly approves that the relaxing scheme removes the drag-induced critical time step Δt_f^D without sacrificing the accuracy.

5.5 Further investigation: fresh SCC

In the framework of the CFD-DEM approach, the SCC is treated as a mixture of mortar and coarse aggregate. As a Bingham fluid, the mortar brings severe difficulty into the simulation because of the drag-induced step criteria. As given in Eq.3.17, it is implemented based on the assumption of apparent viscosity. For example, if μ, τ_0 and γ_c are 10 $Pa \cdot s$, 10 Pa and 0.001 respectively, the relationship between shear rate and apparent viscosity can be plotted in Fig 5.18. It shows that the maximum $\tilde{\mu}$ is 10000 when the shear rate is below γ_c. Above that, it gradually will approach the value of μ while the shear rate increases. As a conclusion, the apparent viscosity varies in the range of $10 \sim 10010$ $Pa \cdot s$. The shear rate is a changing field, so does viscosity. According to this study, the area with large viscosity affects the numerical stability greatly. If there is a non-slip wall or the fluid is close to the static state, the critical time step can be as small as 1×10^{-7} s. However, due to the high viscosity, the concrete shows quite a high stiffness which means it deforms slowly. Considering the large fluid deformation in the whole flow process, the high computation cost seems extremely unworthy. This situation proves again the benefit of the relaxing scheme as it enables a larger time step.

To show the performance of the relaxing scheme, a case of concrete flow is designed as shown in Fig. 5.19. In a long channel of $0.54m \times 2m \times 0.15m$, there are 3 rectangle rebars placed in the middle crossing the whole channel. Its size of the cross-section is 0.012 m and the interval between rebars or between rebar and boundary is 0.041 m. In the CFD domain, the left side of the channel is set to be velocity inlet with a constant value 2 m/s, the right is set as pressure outlet which has a fixed value 0, and the others are all non-slip walls. At the beginning of this case, a total of 1313 particles were distributed randomly in a rectangle area which was 0.1 m away from the left boundary face. As shown in Fig.5.19b, there are 5 types of particles with different sizes including 0.007, 0.009, 0.011, 0.015 and 0.019 m. They were generated based on two parameters: the number ratio are fixed as $5:5:1:1:1$ and the volume fraction 0.3 in the packing area. When the simulation began, the particles were driven downstream by the inletting concrete and came across the 3 rebars. The material properties are listed in Table 5.4. In such a scenario, compared with the time consumed by the CFD solver, the cost of the DEM solver is very small and can be ignored. So, the time step of the CFD solver is determinant in terms of the simulation efficiency. In the following discussion, the time step of CFD will be the focus of the discussion. As a comparison, two simulations with different step sizes were carried out. The first one based on the relaxing scheme used 1×10^{-5} s and 1×10^{-6} s respectively for CFD and DEM. The other one using the classic scheme [47] was set to be 1×10^{-7} s and 1×10^{-7} s respectively. For the latter, it is worth to mention that a time step combination 1×10^{-6} s and 1×10^{-6} s was tried before the final determination. As expected, it failed due to the same particle oscillation phenomenon depicted in Chapter 5.2.1.

The results of the two cases are plotted contrastively in Fig. 5.20, which compares the particle distribution at different instances. Firstly, the case with a relaxing scheme ran stably in its simulation and generated a smooth result as shown in Fig.5.20b. Secondly, comparing the corresponding graphs of the two cases, a similar distribution pattern can be observed. At the time 0.3 s, the two graphs are superficially identical. After the particle group reached the rebars, a difference occurred on the flow front which shows that the particles in the middle

Table 5.4 Material properties of concrete workability tests

Aggregate Parameters	Value	Fluid Parameters	Value
Diameter (mm)	$7, 9, 11, 15, 19$	Density (kg/m^3)	2250
Number ratio	$5:5:1:1:1$	Viscosity ($Pa \cdot s$)	10
Aggregate volume fraction	0.3	Yield stress (Pa)	10
Density (kg/m^3)	2750	Critical shear rate	0.001
Young's Modulus (Pa)	5.0×10^6		
Restitution Coefficient	0.3		
Friction Coefficient	0.5		
Poisson's Ratio	0.49		

move faster in Fig.5.20b. Viewing from the overall pattern, the particles in the Fig.5.20a disperse in a larger space. However, the particles left after the rebars have a very close distribution. The fluid field is non-steady in the domain, so, normally, obvious differences are observed between the two cases. Their time steps differ too much, so is their frequency of field exchange between CFD and DEM. What's more, the collision between particles and rebars exaggerates such difference to some extent. So, it is never expected to obtain two identical results. Nevertheless, the smooth simulation process of the relaxing case and the similarity between the two cases together demonstrate that the relaxing scheme can enlarge the time step by 100 times for CFD and 10 times for DEM. It is worth mentioning that the step size of DEM is now controlled by the step criterion of particle contact which is 1×10^{-6} s, which means the relaxing scheme has increased the time step to its limit.

5.6 Conclusions

In the perspective of particle motion, the drag force can be treated as a kind of damping since it always tends to diminish the relative fluid-particle motion and reach a certain state of equilibrium. However, in the unresolved approach, the implementation of drag force is unbounded for both CFD and DEM solvers. Thus an extra time step criterion is introduced consequently for each of them, which is inherent to bound the drag force.

Given the above knowledge, the quantitative time step criteria are derived for both CFD and DEM solvers, they are verified individually by case study. In the next step, the relaxing scheme, which recovers the relaxation process, is proposed to remove the drag-induced criteria. To implement this scheme in both solvers, the particle velocity in the drag force term is assumed to be a dependent variable. In this way, self-bounded solutions for particle velocity can be obtained for the two solvers, which promises the boundness in drag force terms. The performance of the two implementations of the relaxing scheme is verified individual by case study, which proves that the time step drag-induced time step can be removed without sacrificing the accuracy. At last, the relaxing scheme is applied in a complicated case involving, and the result is compared with the one from the original scheme. Again, the relaxing scheme shows that it can provide the same result with a much larger time step. As a versatile scheme, it generally can be applied to all kinds of situations. Especially, the scheme makes it possible to simulate the cases smoothly, which encounters the extreme small relaxation time for example high viscosity, high particle volume fraction, high relative velocity and small particle size. And the L box test simulation of fresh concrete is given as an example of demonstration, which is almost impossible to run without the relaxing scheme.

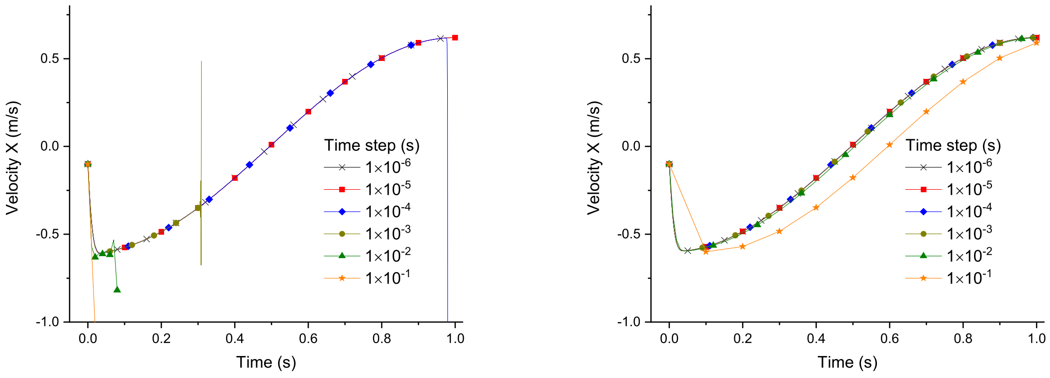

(a) Velocity in X direction: explicit scheme (b) Velocity in X direction: relaxing scheme

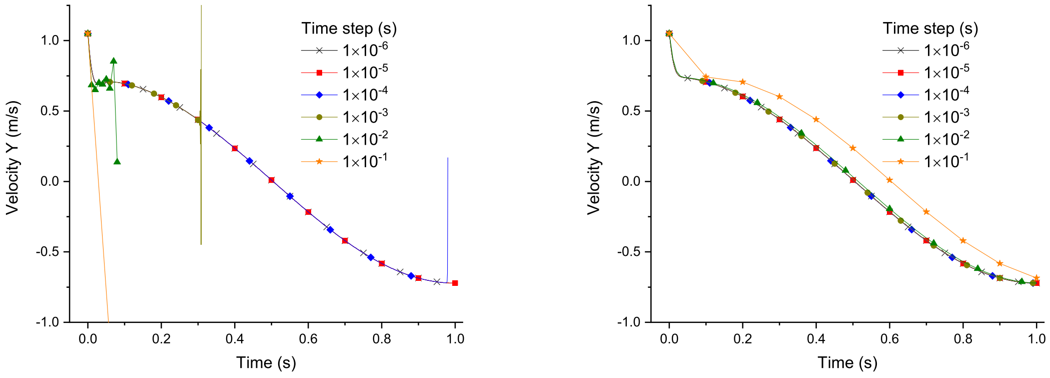

(c) Velocity in Y direction: relaxing scheme (d) Velocity in Y direction: explicit scheme

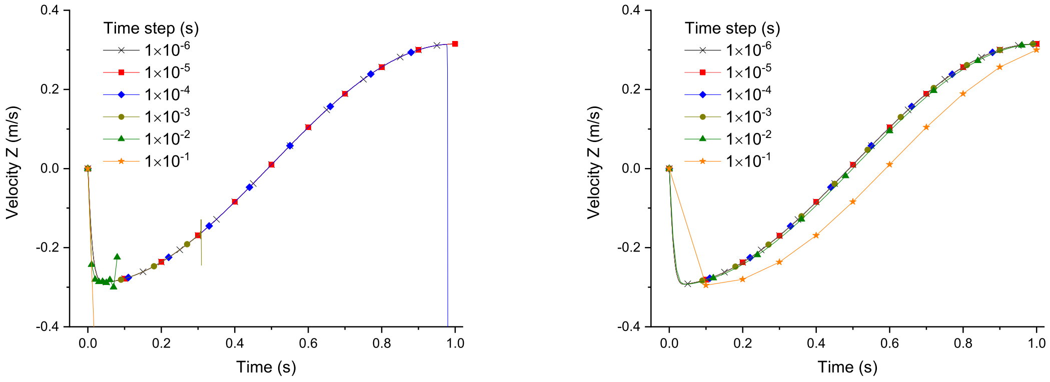

(e) Velocity in Z direction: explicit scheme (f) Velocity in Z direction: relaxing scheme

Fig. 5.11 case 2: 3D comparison of particle velocity

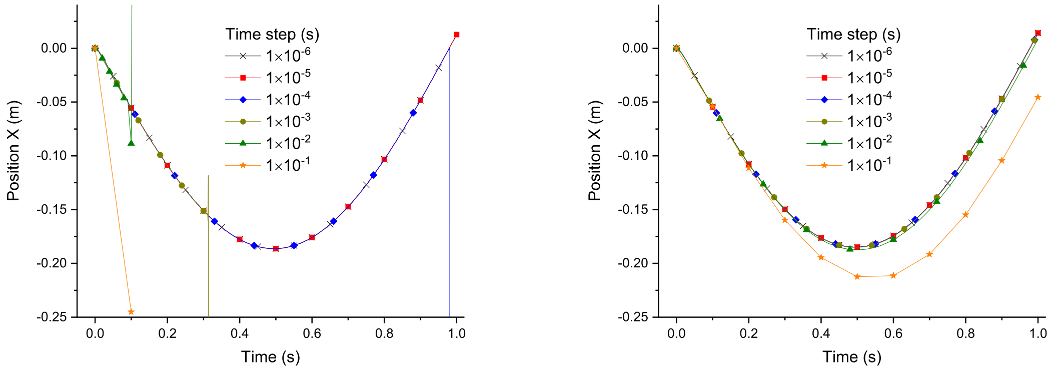

(a) Velocity in X direction: explicit scheme (b) Velocity in X direction: relaxing scheme

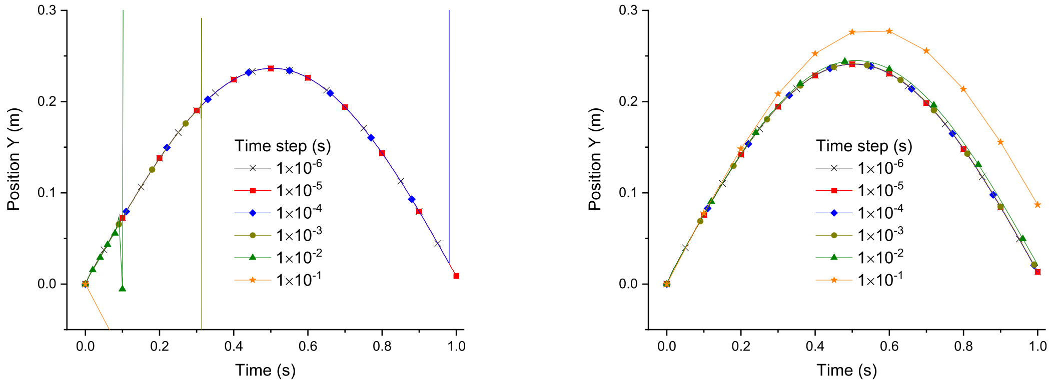

(c) Velocity in Y direction: explicit scheme (d) Velocity in Y direction: relaxing scheme

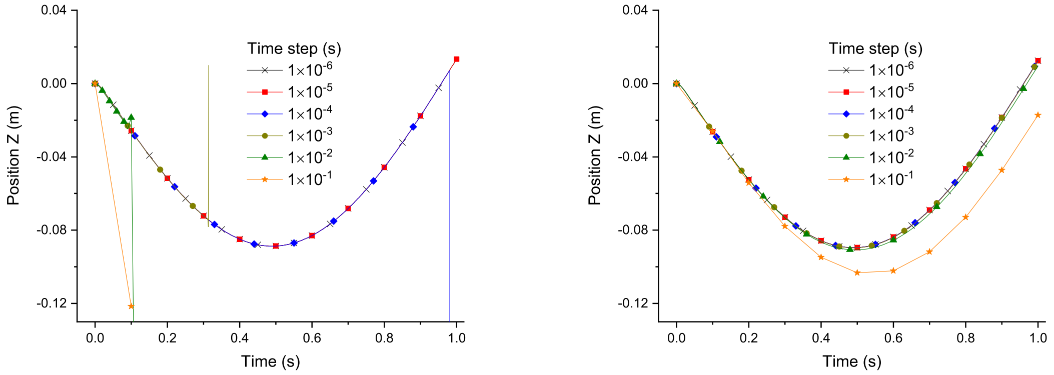

(e) Velocity in Z direction: explicit scheme (f) Velocity in Z direction: relaxing scheme

Fig. 5.12 case 2: 3D of particle position

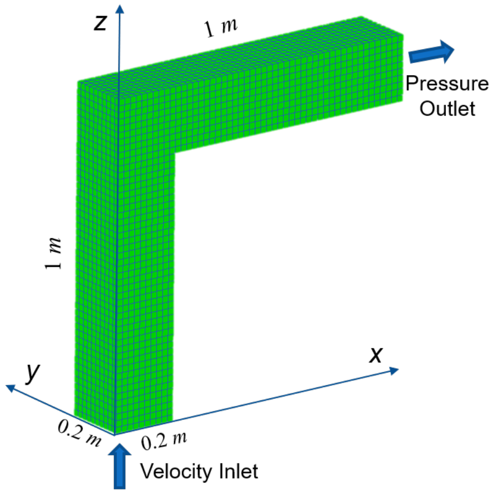

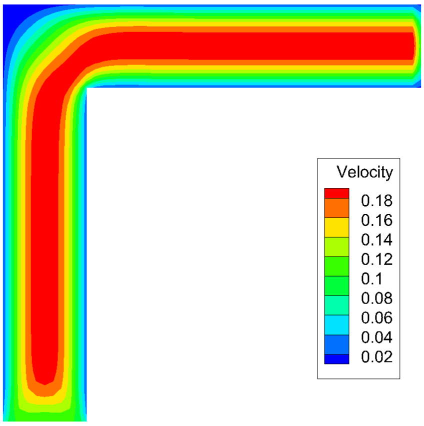

Fig. 5.13 Square-sectional bent pipe Fig. 5.14 Steady field of the middle section

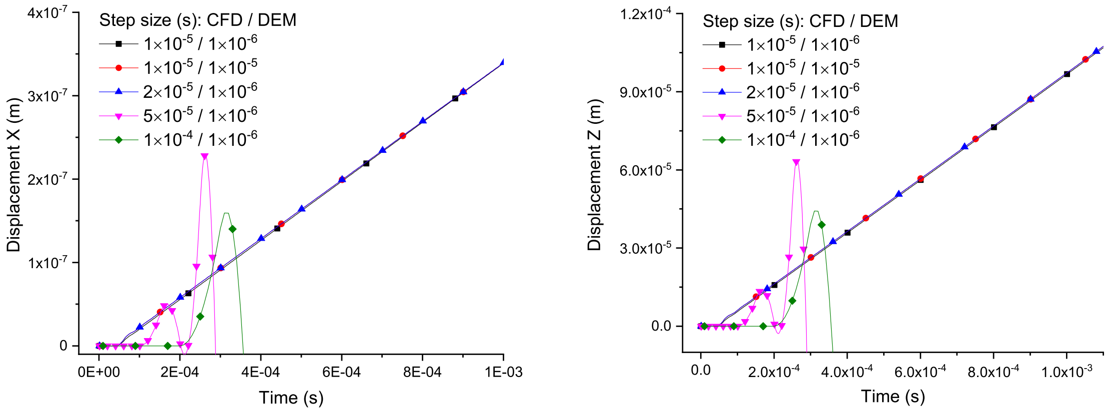

(a) Displacement in X direction (b) Displacement in Z direction

Fig. 5.15 History of particle displacement: numerical stability and time step in CFDEM

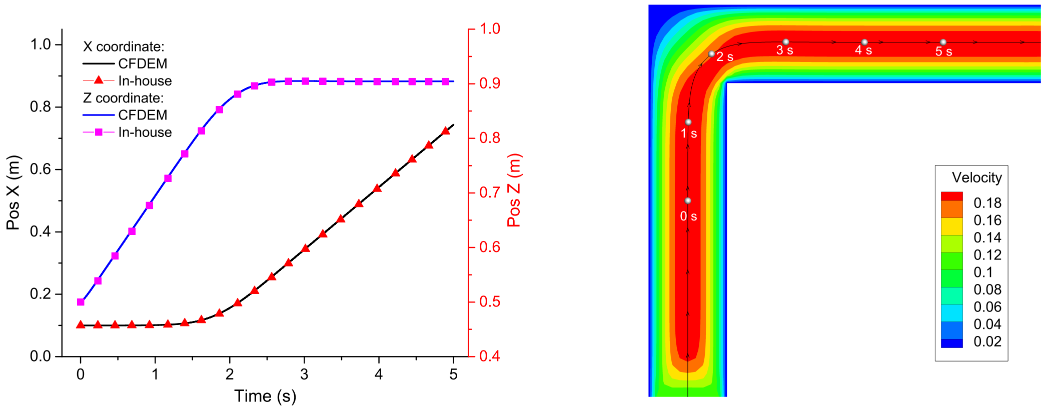

(a) Particle trajectory: CFDEM VS in-house code (b) Particle trajectory and steady flow streamline

Fig. 5.16 Particle motion in 5s for case (10^{-5}, 10^{-5})

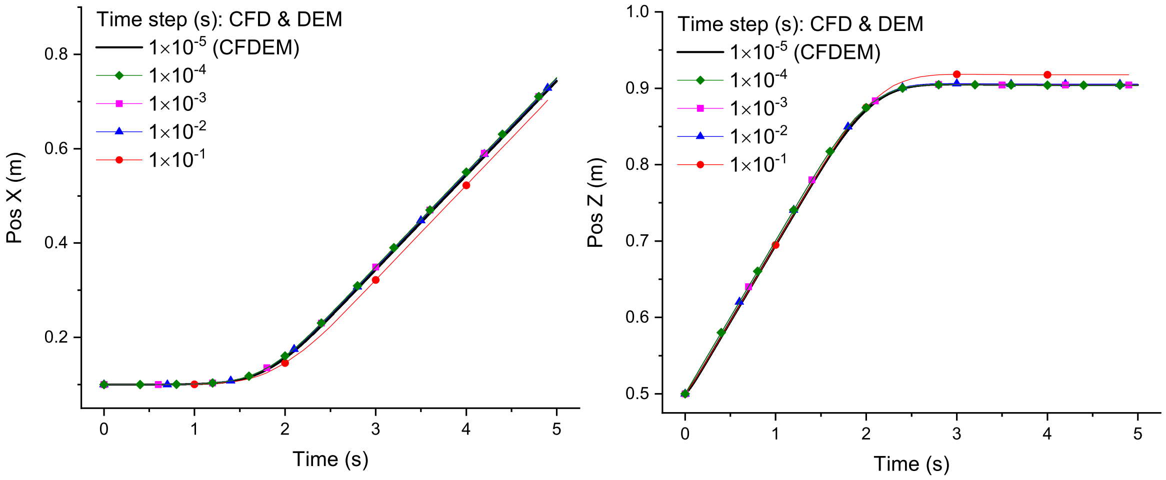

(a) X coordinate of particle position

(b) Z coordinate of particle position

Fig. 5.17 Particle trajectory: CFDEM VS in-house code

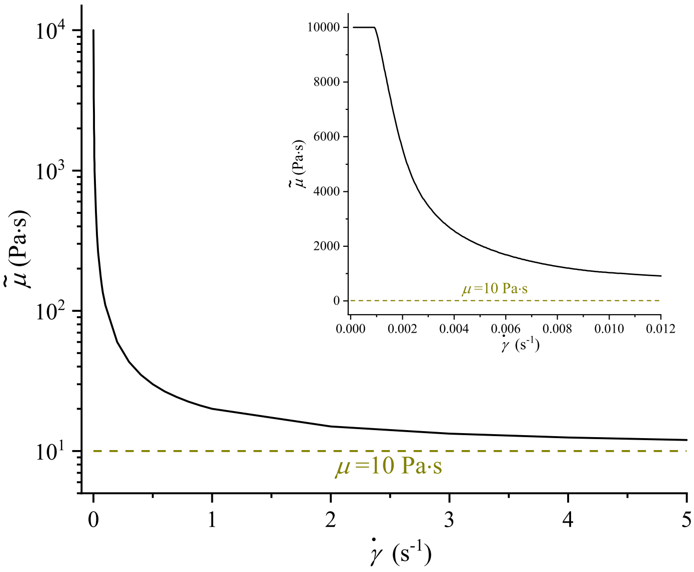

Fig. 5.18 Bingham model: apparent viscosity VS shear rate

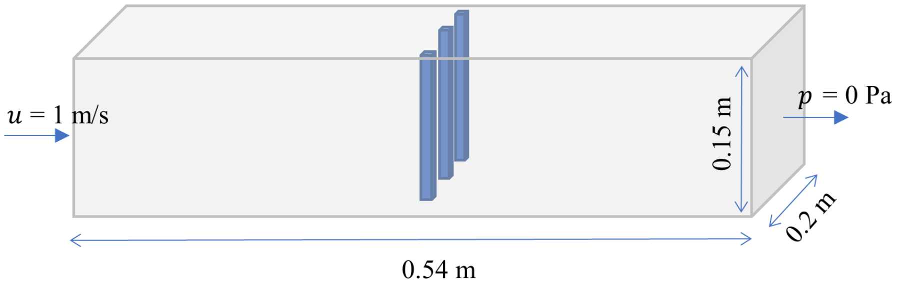

(a) 3D view

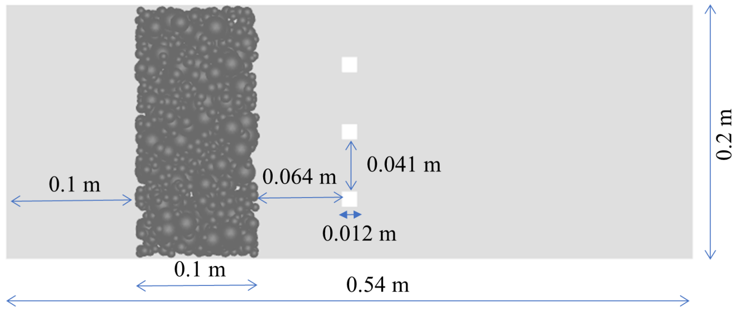

(b) Top view

Fig. 5.19 Geometry and initial setup

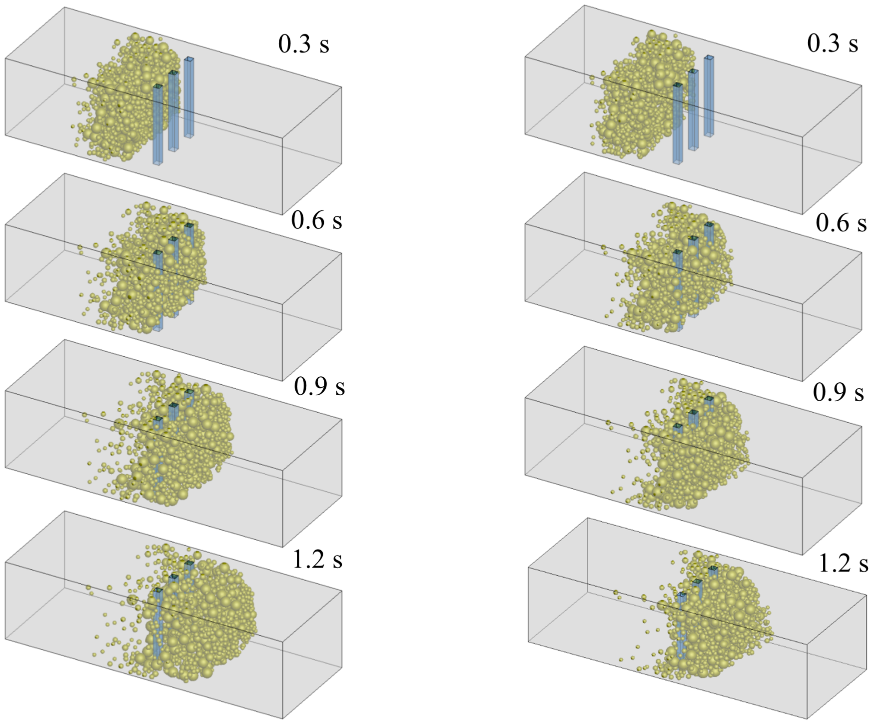

(a) Original scheme: $1 \times 10^{-7}\ s$

(b) Relaxing scheme: $1 \times 10^{-5}\ s$

Fig. 5.20 Result comparison: original scheme VS relaxing scheme

Chapter 6

Simulation of workability tests by the VOF-DEM method

6.1 Introduction

Chapter 4 and 5 introduced the two important difficulties faced in the flow simulation of fresh concrete. The former implemented the VOF model to enable the multiphase flow and developed an improved mapping scheme for the coupling stage. The latter chapter analyzed the time step criteria due to drag force coupling and derived analytical solutions for both CFD and DEM solvers to remove these criteria. The two chapters solved the major challenges for the concrete simulation and the solutions have been implemented in our in-house code. So the focus of this chapter will be the performance of the code, and the concrete workability tests are to be used for demonstration. In the first part, the V Funnel, slump flow and L box tests are given as examples. As shown in Chapter 2, the slump flow test and V funnel tests are reliable and robust in determining concrete rheology. While the L box test is used to test the passing ability of concrete through a row of rebars. Since the aggregate will be modeled in the framework of the unresolved CFD-DEM, it is an important test for observing the impact of aggregate properties. All the 3 tests are standard workability tests for SCC. In the second part, a parametric study is done based on the L box test, which investigates the influence of particle gradation and fluid properties. At last, the code performance is to be concluded and the outlook for further research will be given.

6.2 Simulation configuration of workability tests

In Chapter 2, 4 workability tests were simulated by pure CFD. Here, the slump flow and V funnel are continued to be used. In addition, the L box test is also introduced. Due to the unaffordable computation cost, for each test, only one result will be presented, which means 3 cases in total. The material properties for them are the same and listed in Table 5.4. The gradation of coarse aggregate is considered and 5 levels of particle size are set which varies from $7 \sim 19$ *mm*. The number ratio among different levels is set as $5:5:1:1:1$ and the exact particle number used in every case is computed individually based on the same global aggregate volume fraction 0.3. Its density is 2750 kg/m^3. The other parameters for particle contact including Young's modulus, restitution coefficient, friction coefficient and Poisson's Ratio are 5.0×10^6 *Pa*, 0.3, 0.5 and 0.49 respectively. On the CFD side, there are two fluid phases which are air and mortar. The former is the Newtonian fluid while the latter is a Bingham fluid. The air properties are the same as in the previous cases. The viscosity and yield stress of the mortar are 10 $Pa \cdot s$ and 10 *Pa*. The mortar density is set to be 2250 kg/m^3, which makes the apparent density of the concrete mixture to be 2400 kg/m^3. While the detail of the L box will be introduced in later discussion.

Table 6.1 Material properties of concrete workability tests

Aggregate Parameters	Value	Fluid Parameters		Value
Diameter (mm)	$7, 9, 11, 15, 19$	Mortar	Density (kg/m^3)	2250
Number ratio	$5:5:1:1:1$		Viscosity ($Pa \cdot s$)	10
Aggregate volume fraction	0.3		Yield stress (Pa)	10
Density (kg/m^3)	2750		Critical shear rate	0.001
Young's Modulus (Pa)	5.0×10^6	Air	Density (kg/m^3)	1.225
Restitution Coefficient	0.3		Viscosity ($Pa \cdot s$)	0.000018
Friction Coefficient	0.5			
Poisson's Ratio	0.49			

6.3 Apparent rheology: V Funnel test and slump flow test

The geometry and mesh of the V funnel test have been presented in Fig.2.2 and Fig.2.6, so the same configuration will be followed in this case. The stepping scheme of fresh SCC has been discussed in Chapter 5.5, and the same setup is to be used which is 1.0×10^{-4} *s* for CFD and 1.0×10^{-6} *s* for DEM. In total, a duration of 4.5 *s* was simulated and the result is shown in Fig.6.1. It can be seen that the whole bulk of concrete was discharged at about 4.5

s. Fig.6.2 is the frame taken at time 3.7 s when the funnel can be seen through. So, according to the definition of V funnel discharging time t_n, its value is given as 3.7 s.

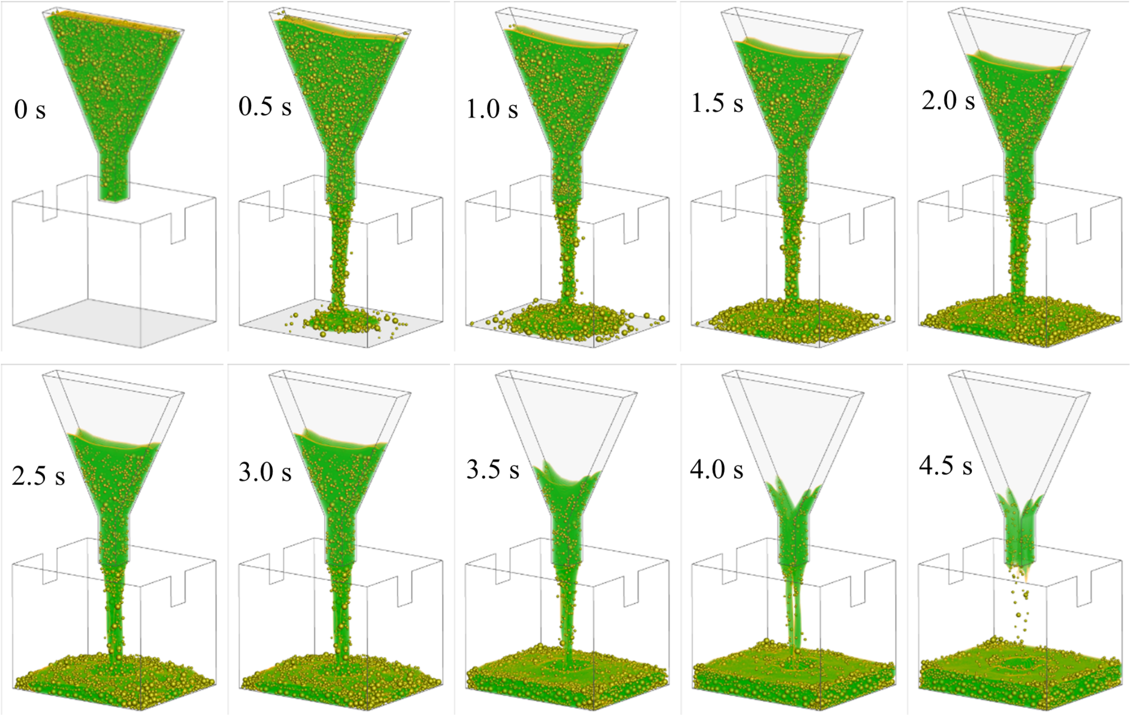

Fig. 6.1 Simulation result of V Funnel test

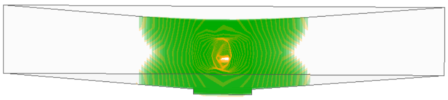

Fig. 6.2 Seeing through the funnel at 3.7 s

Similarly, the slump flow case follows the geometry and mesh in Fig.2.1 and Fig.2.5. Its stepping scheme is also 1×10^{-4} s for CFD and 1.0×10^{-6} for DEM. The case was run for 2 s, and its result is presented in Fig.6.3. It gives a similar phenomenon as the pure CFD simulation given in Chapter 2.2. The spreading developed very fast within 0.25 s, then slowed down quickly after that and stopped at 2 s. The difference lies in the unsymmetric pattern of the spread which is resulted from the randomly generated particles and the chaotic collisions between them. The final diameter D is measured from the Fig.6.4 which gives 0.53 m.

As a conclusion, for the fresh concrete material given in Table 6.1, the discharging time of V funnel and spreading diameter of slump flow test are 3.7 s and 0.53 m respectively. Referring to the Fig.2.37, the equivalent viscosity and yield stress of the concrete or the

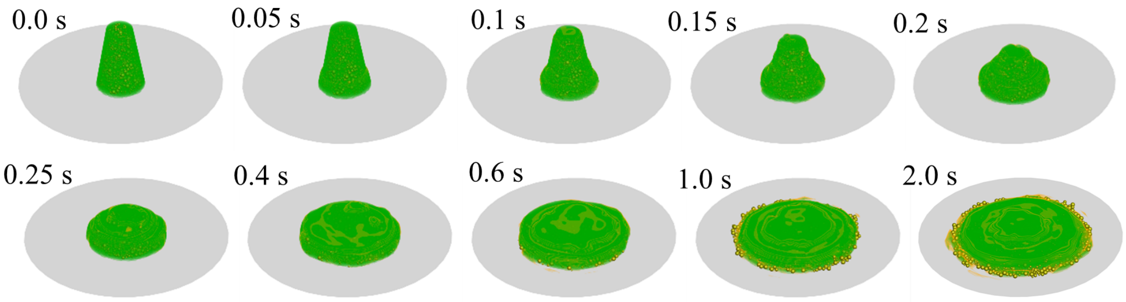

Fig. 6.3 Simulation result of slump flow test

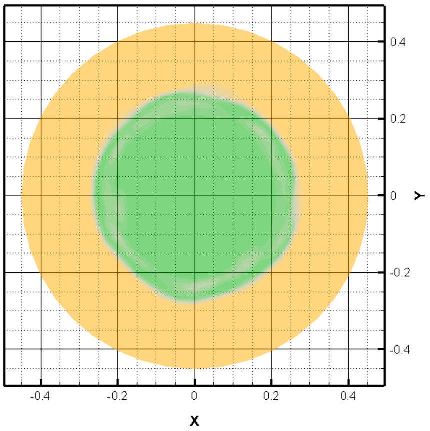

Fig. 6.4 Final diameter of concrete parameter

mixture of mortar and aggregate can be read as 20 $Pa \cdot s$ and 100 Pa respectively. Compared with the mortar, the former is increased by 2 times and the latter is by 10 times.

6.4 Parametric study: L box test

As shown Figure6.5, the L box test is designed to evaluate the passing ability of SCC specifically. At the beginning of the test, the vertical part is filled with fresh concrete which is held still by a gate. Once the test starts, the gate will be taken off in one instance and the concrete is allowed to flow into the horizontal part. In this process, it will come across 3 rebars not far from the gate. For numerical simulation, an enclosed domain covering the L box is designed. To get a structured mesh as shown in Fig.6.6, the rectangle section are used for rebars. In total, there are 8842 cells and the minimum size is rebar size 12 *mm*.

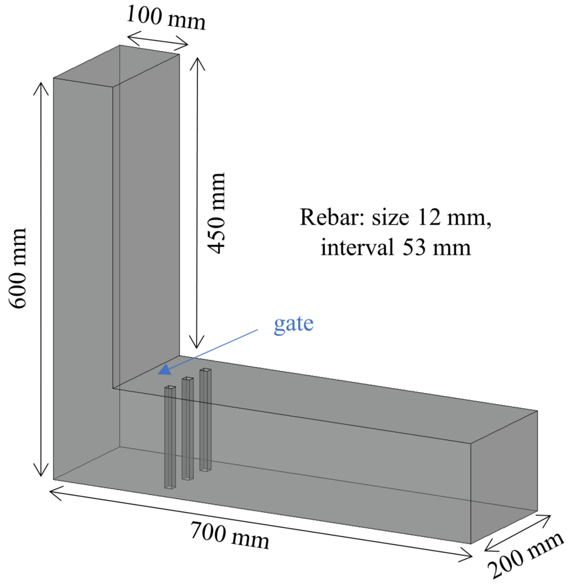

Fig. 6.5 L box apparatus

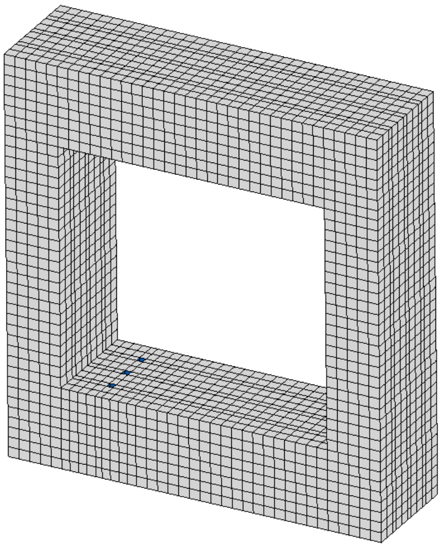

Fig. 6.6 Numerical model and mesh

In this section, 3 factors including the particle gradation, the existence of particles and the existence of rebars are chosen to investigate the flow behaviour in the L box test. To this end, 5 cases in total are designed as shown in Table 6.2. In the following, the 3 aspects will be explained in detail.

Table 6.2 Summary of L box cases

	Gradation	**Number of rebar**	**Aggregate Volume fraction**
Case 1	Gradation 1	3	0.3
Case 2	Gradation 2	3	0.3
Case 3	Gradation 3	3	0.3
Case 4	Gradation 3	0	0.3
Case 5	No aggregate	3	0

Impact of gradation

To study the influence of aggregate gradation, 3 levels are designed for comparison which includes the Case 1, Case 2, Case 3. They share the same aggregate volume fraction 0.3, and all have 3 rebars. The gradation design is given in Table 6.3. Gradation 1 has only one type particle, gradation 2 has 3 types and the gradation 3 has 5 types. Their diameters and the number ratio in different gradations can be found in the table. The total number of particles in 3 cases is 6875, 5400, 5278 respectively. In the initialization of the 3 cases, the particles were generated randomly as shown in Fig.6.7. In the simulation, the 3 cases were run for 1.4 *s* and their results are presented in Fig.6.7a to Fig.6.7c. Superficially, we can observe that the 3 cases generate the very same similar result. For all graphs at the same time, the fluid profile is very close. Their fluid front all reached the right end of the L box at the time 1.4 *s*. After the fluid front passed the rebars, an abrupt level drop can be seen at the position of the 3 rebars. To more precisely capture the difference, the L box mesh is used to assist the comparison between cases. Fig.6.11 presents the mortar profile at the time 0.1 *s* (before the rebars) and time 1.0 *s* (passing the rebars), and ignores the particles in the domain to provide a better view. At the moment of the former, the 3 graphs are very similar but the Case 1 is a bit delayed. While, at the latter, Case 1 shows a clear difference with the other two. In the vertical part, there is a deeper pit on the fluid surface. In the horizontal part, the fluid front is 2 cells ahead. As we know, the aggregate with better-designed gradation could reach a higher maximum packing density. The Gradation 1 should have a lower possibility to reach a high particle volume fraction compared with the other 2 cases. In other words, the former theoretically should go through fewer particle collisions which will indicate less energy dissipation and larger flow velocity. But the Case 2 and Case 3 shows great similarity at both moments and the difference is hard to recognize. As a conclusion, it can be explained in another way: as the concrete in Case 1 flows faster than the two cases, it indicates the former has a smaller viscosity; the concretes of the Case 2 and 3 have similar rheology.

Table 6.3 Gradation of aggregate

	Diameter (mm)	**Number ratio**	**Total number**
Gradation 1	10	1	6875
Gradation 2	8, 13, 17	6 : 1 : 1	5400
Gradation 3	7, 9, 11, 15, 19	5 : 5 : 1 : 1 : 1	5278

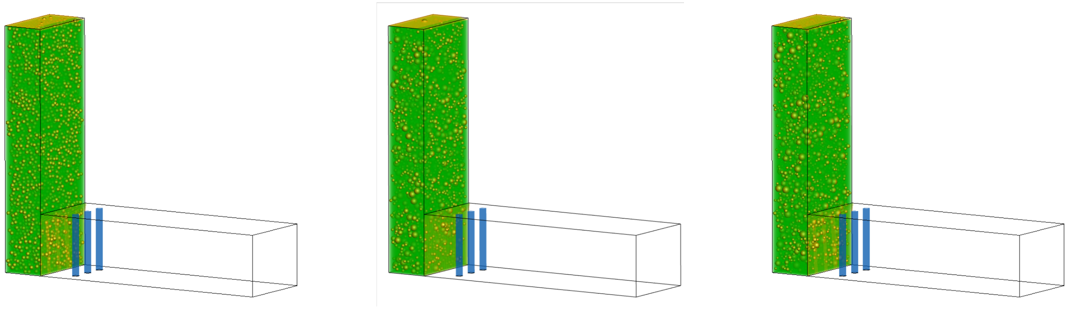

(a) Case 1

(b) Case 2

(c) Case 3

Fig. 6.7 The initial configuration of 3 cases

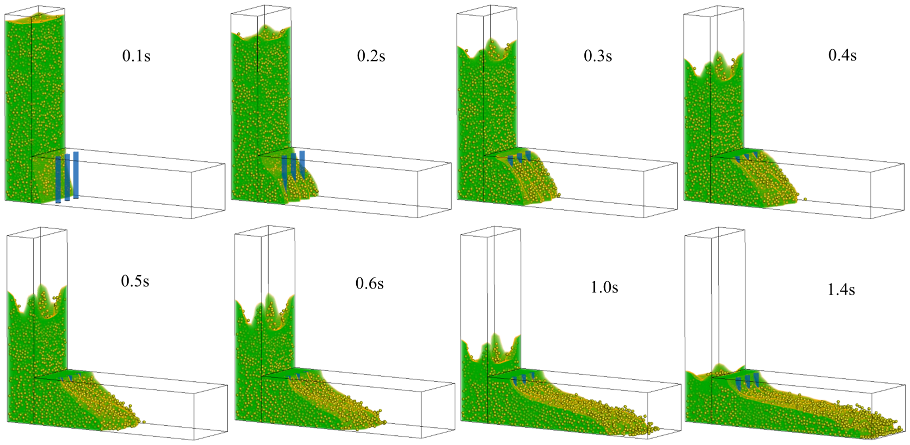

Fig. 6.8 Flow history of Case 1

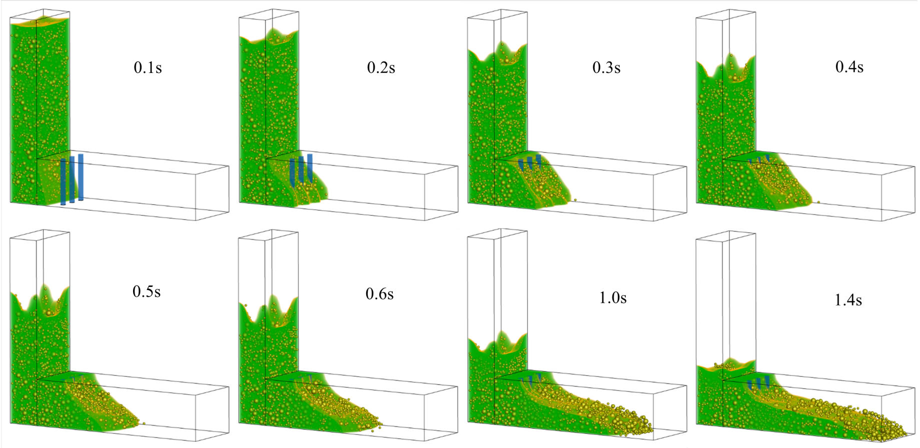

Fig. 6.9 Flow history of Case 2

Existence of rebar

In the L box, the existence of rebar is a major factor affecting the concrete flow behaviour. To demonstrate its influence, the Case 1 and 4 are used for comparison. The two cases use the same gradation 3 and the same aggregate volume fraction 0.3, but the latter has no rebar. The simulation result of the latter is presented in Fig.6.12 which also covers a duration 1.4 s. Compared with the result of Case 1 in Fig.6.10, the mixture of Case 4 flows much faster as the fluid front reached the right end at the time 1.0 s which is 0.4 s earlier. Besides, without the rebars, the fluid profile shows high smoothness. Especially the slope of running fluid front, the abrupt level rising on the right side the of rebars due to retardation is gone. This comparison shows that the existence of the rebars has a greater influence on the concrete flow behaviour.

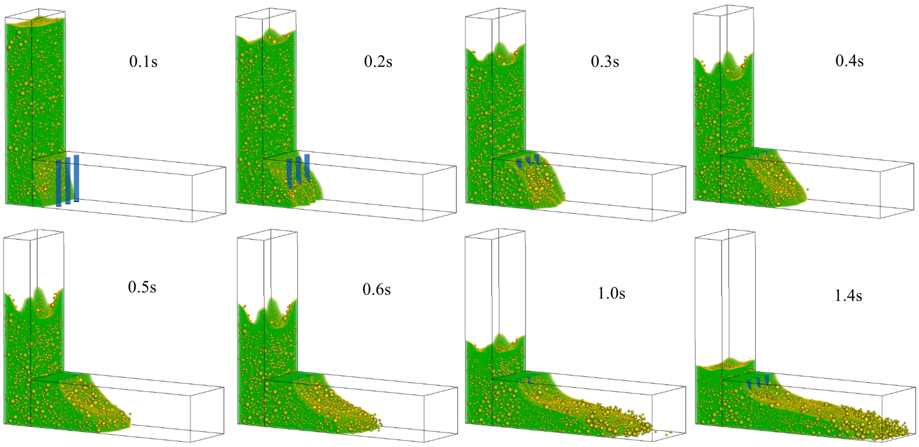

Fig. 6.10 Flow history of Case 3

Existence of particles

This section aims to show how the existence of the particles affects the fluid flow. In other words, the difference between pure CFD and CFD-DEM will be investigated. In Case 5, there is only pure mortar without the aggregate, but the 3 rebars are kept. Its result is presented in Fig.6.13. As expected, we can see that the fluid flows much faster than Case 1 $\sim$ 3. It is even faster than the Case 4 as the fluid front reached the right end before 1.0 s. It is understandable since the CFD-DEM introduces the friction between particles which is an extra source of energy dissipation. The apparent viscosity of the mixture is of course larger than the pure fluid. In addition, we can also observe the profile of the fluid surface is quite smooth around the rebars. It indicates that the sudden drop in Case 3 is caused by particle collisions. Compared with the result of Chapter 6.4, the existence of the particles has a greater influence on the concrete mixture flow compared with the rebars.

6.5 Conclusion and outlook

The focus of this chapter is the simulation of the concrete workability test by our in-house CFD-DEM code. The concrete is treated as a mixture of flowable mortar and coarse aggregate. For all cases, the same mortar properties are used. The aggregate is modelled by sphere for simplification. For the mixture of them, the aggregate is set to be 0.3 and a bulk density 2400 kg/m^3 is preserved. Based on this setup, the V funnel test and slump flow test were carried out in Chapter **??**. Referring to the relation chart between workability tests and concrete rheology given in Fig.2.37, the apparent viscosity and yield stress are obtained.

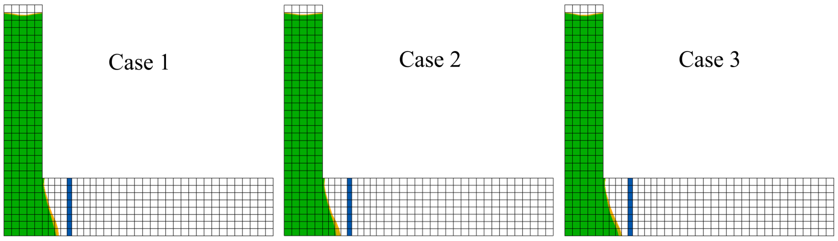

(a) Time 0.1 s

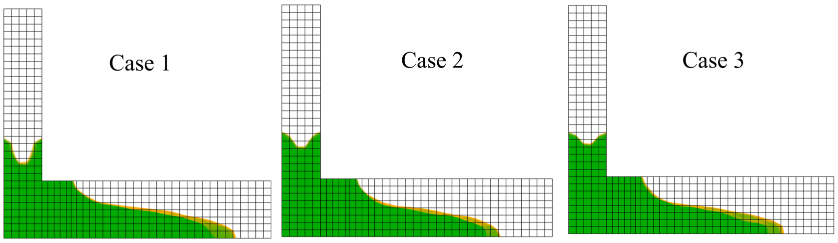

(b) Time 1.0 s

Fig. 6.11 Comparison of the fluid profile in 3 cases

In Chapter 6.4, the L box test is used to demonstrate the influencing factors in concrete flow including the particle gradation, the existence of rebar and particles. The simulation result shows that: (1) the mixture with several particle sizes flows slower than the case with uniform particles; (2) the existence of 3 rebars delays the mixture flow greatly and create a significant level difference between the two sides of the rebars; (3) the existence of particles in the mixture greatly slows the fluid flow. Theoretically, a slower motion means that the bulk mixture is "thicker" which shows the rheological properties of the concrete. However, the corresponding relation between the material properties of the bulk mixture and its components including mortar and aggregate is still a big question that requires further effort.

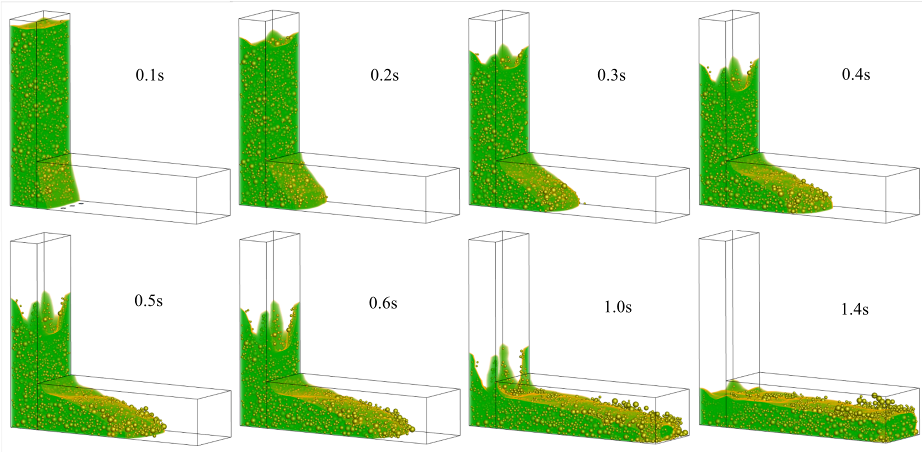

Fig. 6.12 Flow history of Case 4

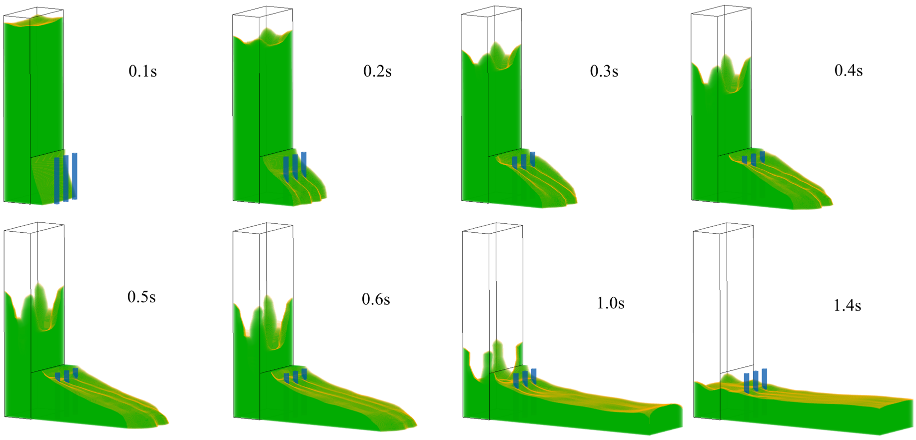

Fig. 6.13 Flow history of Case 5

Chapter 7

Conclusions and outlook

7.1 Conclusions

Nowadays, the SCC is playing a more and more important role in modern construction because of its great flexibility applicability. Contrary to its popularity, the mechanism of its flow behaviour is not studied sufficiently yet. In real applications, many crucial issues are challenging both research and industry communities as the various defects are found in deep foundation construction. The purpose of this whole thesis is to develop a numerical technique to study the mechanism in defect occurring. The content can be divided into 3 parts: literature review in Chapter 1, the preliminary study in Chapter 2 and the further investigation in Chapter 3 to 6.

In the literature review, the material rheology and the concrete flow simulation are the focus of interest. Accepted by most researchers, the fresh concrete is a classic Bingham fluid. Despite this consensus, there is no widely agreed direct solution to obtain the concrete rheology due to the complexity of the concrete material. So, it is the first challenge faced in this study. Further, in terms of concrete flow simulation, the research work on this topic is so limited. In the literature, the concrete is either treated as a continuous fluid or a discontinuous material. The former was solved by the CFD, the latter was simulated by DEM, and a method in between was rare. In the real application, the size of coarse aggregate, the CFD mesh size and the rebar size are very close. The result of pure CFD or pure DEM solution would lose the important feature on the other side. So, a CFD-DEM method is strongly desired to track the local interaction at the scale of particle size. The phenomena such as segregation, filtration and blockage due to rebars are often related. Given the available solutions and computation resources, the mesh-based unresolved CFD-DEM approach is chosen as the basis to develop our method for concrete flow simulation.

In the preliminary study, the concrete was treated as a homogeneous fluid and the commercial software Fluent is used to analyse its flow behaviour. This work has been expatiated in Chapter 2 which achieved two major tasks. Firstly, by a systematic parametric study, a relation chart was generated which correlates the robust workability tests with the rheological parameters. It allows fast acquisition of the numerical-suited properties from on-site workability tests. As a result, this indirect solution solves the first challenge raised in the literature review. In the second part of this chapter, the simulation of a diaphragm wall was carried out as an example to apply the relation chart. According to the on-site workability tests of the commercial concrete, the parameters of each truck were obtained. Based on it, the diaphragm wall construction with heterogeneous SCC was simulated. As a comparison, the same process was repeated using the homogeneous SCC. As the result showed, the distribution of different batches of concrete in the diaphragm wall was captured by the multiphase model. Comparing the phase distribution of the two cases, a very similar pattern appeared on the right-half wall but a significant difference was on the left, which could be due to the large concrete yield stress or its large variation on the left. In conclusion, the homogeneous fluid assumption can model the bulk flow of fresh SCC and can be used to track the concrete distribution in real applications. But it can not help with research on the scale of particle size which is of vital importance.

In a further study, the framework of the unresolved CFD-DEM approach was introduced to our study to address the second challenge. It treated the fresh SCC as a mixture of mortar and coarse aggregate. Because the size of the latter is close to the rebar size and the cell size of the CFD mesh, the DEM method is preferred to model the aggregate and solve its trajectory explicitly. The coupled CFD-DEM solution has the great advantage to provide the interacting details among particles or between particles and fluid. In Chapter 3, the formulation of the unresolved CFD-DEM approach was expatiated, based on which our in-house CFD-DEM code was developed. Before applying it, the validation was carried out by comparing with the sophisticated software by 3 steps. In the first step, the *OpenFOAM* was used to validate the CFD solver and the embedded Bingham model by the two cases lid-driven cavity and bent pipe flow. In the second step, the DEM solver was validated by the *LIGGGHTS* by the case of slope failure. In the third step, the coupling between CFD-DEM was validated by comparing with the software *CFDEM* in the simulation of a slope failure in a viscous fluid. The above cases together demonstrate the validation of our in-house CFD-DEM code.

In Chapter 4, two major functionalities were listed which were essential to realize the SCC flow simulation functionalities: a multiphase model for the three-phase system; a versatile mapping scheme to conserve the particle volume, be stable for the interface passing process, be compatible with the various particle sizes and a random CFD mesh. In the real application, the three-phase system is composed of air, mortar and aggregate. To achieve it, the VOF model was introduced and implemented in our in-house code. To validate the new CFD soler, a dam break case was designed for result comparison which proved a success. After that, a literature review was done for the mapping scheme between CFD and DEM. It was found that most of the current research focuses on the mapping of volume fraction and the rest parameters were rarely mentioned. It was sufficient for them because they were working on a two-phase system including one fluid phase and a discrete phase. In this study, due to the great difference between air and concrete, the mapping scheme for all parameters would be analyzed systematically. According to the belonging of a parameter, a different mapping scheme was applied. For example, for the parameters belonging to the space dimension such as the volume fraction, the distance-based $statistickernel$ method is used to generate a smooth field in the CFD domain which will be of great favor for the numerical stability. This method is independent of the size ratio of cell size to particle diameter. While, for the fluid-particle interacting forces, the material field should be weighted in distributing the computed forces such as a particle straddling on the interface of two phases. The mapping schemes for all parameters were implemented in the in-house code and 3 cases were designed to test the performance. In the first two cases, the scenario was about the particle falling from air into the water which was used to test the performance of our mapping scheme. The first case has a relatively coarse mesh and a group of particles, but the second has a relatively small cell size and a large particle. Both cases showed a stable simulation, a smooth result and the volume conservation of phases, which proves the validation of our mapping scheme. In the third case, the fluid-particle torque due to relative angular velocity was implemented according to the given principle for force mapping. In this case, a fixed particle, which was straddling on the interface of air and water, was rotating at a fixed angular velocity. It created a vortex on the water surface as expected which proves the feasibility of the mapping scheme. In conclusion, the chapter implemented the VOF model to enable the simulation of a three-phase system and improved the mapping scheme to promise a smooth performance in the so-called VOF-DEM method.

In Chapter 5, the major difficulty to realize an effective simulation of SCC flow was addressed and solved. Due to the force coupling between CFD and DEM, extra step criteria were induced. This chapter focused on the formulation for drag force and ignored other secondary forces like lift force and virtual mass force. It started with the derivation of the drag-induced critical time step for both DEM and CFD both of which were demonstrated by the software $CFDEM$ quantitatively. It was pointed out that when the fluid viscosity was very large such as honey, lava and SCC, both critical time steps would be extremely small which makes computation cost unaffordable. To overcome this difficulty, the so-called relaxing scheme was proposed. Instead of the assumptions with a low order of accuracy, it tries to provide the whole relaxing process of a particle by an analytical expression so that the time step criterion will be gone. Following this scheme, two different solutions were derived for DEM and CFD respectively. In the cases where there was only one particle, the two solutions of the relaxing scheme could perfectly improve the time step by 100 times for both DEM and CFD without sacrificing the accuracy. In the last, the SCC was used as the material where fluid was the mortar and particles were for aggregate. The relaxing scheme again was able to increase the time step by 100 times. However, due to the complexity of this case, an identical was not available and also was not expected from the upscaled relaxing scheme. The similarity between the results from the original scheme and the relaxing scheme successfully demonstrates the great advantage of the latter as it updates the time step size of concrete simulation to an acceptable value.

Based on the achievements of Chapter 4 and 5, a series of SCC workability tests were carried out by our improved in-house in the Chapter 6. All the cases shared the same mortar and aggregate properties. In the first part, the V funnel and slump flow tests were carried out. According to the measured indices of the two tests, the apparent Bingham parameters of the concrete mixture were obtained by referring to the relation chart in Chapter 2.2. In the second, a parametric study was carried out using the L box test. The influence of aggregate gradation, the existence of rebars and the aggregate were analyzed. The result showed that the existence of the last is the most influential, the middle is secondary and the first is least important. The results of the above cases demonstrate that our in-house code of the VOF-DEM method is ready to study the mechanism of SCC flow on the scope of aggregate scale.

7.2 Future work

The main task of this study is to establish the framework of numerical technique for fresh SCC flow. The goal has been successfully achieved in this thesis, however, more interesting questions come out. Due to the limited time of my PhD, they cannot be covered in this thesis but will be my future study.

The validation of the single-fluid-phase unresolved CFD-DEM approach has been carried out by many researchers like Kloss et al. [47] and Peng et al.[67]. However, the validation for the VOF-DEM method is rare and can't cover the complicated concrete flow which has the shear-dependent apparent viscosity and the material discontinuity because of the multiphase flow. As we know, the models for the fluid-particle forces listed in Table 3.6 are derived based on Newtonian fluid. So, the accuracy of these models should be verified experimentally for Bingham fluid. In addition, although the proposed smooth mapping scheme works well in our case study, its accuracy in difficult scenarios is not considered yet. For example, assume a particle is close to the interface: if a particle moves from a dense fluid into a thin one, or if a particle is moving in one phase but close to the interface where the velocity gradient differs greatly on the other side. Besides, in some cases, many other fluid-particle forces need to be considered such as the surface tension, capillary force and the Magnus effect. In conclusion, the cooperation between our mapping scheme and the VOF-DEM method should be quantitatively tested in more cases.

Chapter 5 introduced the relaxing scheme for drag force whose function is to release the drag-induced step criteria for both CFD and DEM solvers. This scheme has great potential to provide a deeper insight into the multi-scale problem. Originally, the CFD domain and DEM domain are solved separately sharing only limited momentum data. However, the relaxing scheme shows the potential to introduce the full particle contact information into the CFD governing equations. For example, if the lift forces are implemented according to the relaxing scheme, the particle rotation could also be involved in the CFD. Since the CFD governing equations could cover the whole mechanical fields of both CFD and DEM domains, it provides a great opportunity to reach a higher level of coupling between fluid and particles. For example, the cement paste, which is the mixture of water and cement, behaves stably like a homogeneous Bingham fluid. In this case, an ideal CFD-DEM approach should be able to upscale the particle-level phenomenon to the mixture level. Unfortunately, such a topic is rarely discussed in the literature and there is a great gap to be overcome for current approaches. However, the relaxing scheme shows the potential to contribute.

The work of Chapter 4 and 5 can be viewed from another perspective. As shown in Fig. 7.1, the improved mapping scheme extends the upper bound of the unresolved approach since it also works for large particles. At the same time, the lower bound is also extended by the relaxing scheme. Besides large viscosity, small particle size also results in small critical time step. So, by applying the relaxing scheme, the unresolved CFD-DEM approach can simulate the cases with very small particles. In conclusion, this thesis has improved the capacity of the unresolved CFD-DEM approach to a wider range which requires the proof of more case studies in the future.

Last but not least, the numerical technique established in this thesis already shows the great potential to assist the real practices. For the different purposes of investigation, simulation strategies can be chosen differently. For example, if the overall flow pattern of a large amount of concrete is the concern such as a full-scale pile construction, the pure CFD method is preferred because it is sophisticated and saves the simulation cost greatly. While, if the scope of interest is close to the aggregate scale such as the blockage, the CFD-DEM

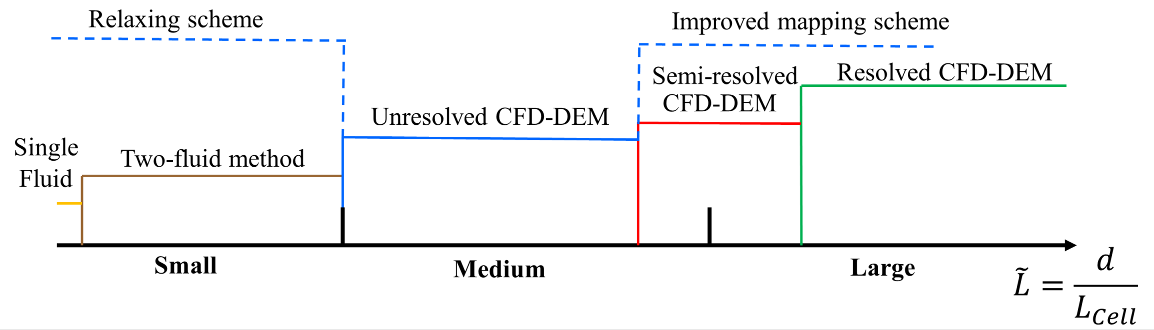

Fig. 7.1 Extension of the unresolved CFD-DEM approach

approach should be applied. Besides, defects could also come from the scale of the sand (settlement of sand) or cement particles (bleeding). By changing the material properties, the framework of the unresolved CFD-DEM approach can be easily applied to the two problems. In a word, the numerical method developed in this thesis is ready to study the flow of cement-based materials and provides a better understanding of the various defects in the real SCC application.

References

[1] AL-Rubaye, M., Kulasegaram, S., and Karihaloo, B. L. (2017). Simulation of self-compacting concrete in an l-box using smooth particle hydrodynamics. *Magazine of Concrete Research*, 69(12):618–628.

[2] Alyhya, W., Kulasegaram, S., and Karihaloo, B. (2017). Simulation of the flow of self-compacting concrete in the v-funnel by sph. *Cement and Concrete Research*, 100:47–59.

[3] Anderson, T. B. and Jackson, R. (1967). Fluid mechanical description of fluidized beds. equations of motion. *Industrial & Engineering Chemistry Fundamentals*, 6(4):527–539.

[4] Badry, F., Kulasegaram, S., and Karihaloo, B. L. (2016). Estimation of the yield stress and distribution of large aggregates from slump flow test of self-compacting concrete mixes using smooth particle hydrodynamics simulation. *Journal of Sustainable Cement-Based Materials*, 5(3):117–134.

[5] Balasubramanian, A. (2017). Soil erosion–causes and effects. *Centre forAdvanced Studies in Earth Science, University of Mysore, Mysore*.

[6] Banerjee, S. and Agarwal, R. (2015). Transient reacting flow simulation of spouted fluidized bed for coal-direct chemical looping combustion with different fe-based oxygen carriers. *Applied energy*, 160:552–560.

[7] Beetstra, R., van der Hoef, M. A., and Kuipers, J. (2007). Drag force of intermediate reynolds number flow past mono-and bidisperse arrays of spheres. *AIChE journal*, 53(2):489–501.

[8] Blais, B., Lassaigne, M., Goniva, C., Fradette, L., and Bertrand, F. (2016). Development of an unresolved cfd–dem model for the flow of viscous suspensions and its application to solid–liquid mixing. *Journal of Computational Physics*, 318:201–221.

[9] Bouvet, A., Ghorbel, E., and Bennacer, R. (2010). The mini-conical slump flow test: Analysis and numerical study. *Cement and concrete research*, 40(10):1517–1523.

[10] Boyce, C. M., Holland, D. J., Scott, S. A., and Dennis, J. (2015). Limitations on fluid grid sizing for using volume-averaged fluid equations in discrete element models of fluidized beds. *Industrial & Engineering Chemistry Research*, 54(43):10684–10697.

[11] Boyce, C. M., Holland, D. J., Scott, S. A., and Dennis, J. S. (2013). Adapting data processing to compare model and experiment accurately: A discrete element model and magnetic resonance measurements of a 3d cylindrical fluidized bed. *Industrial & engineering chemistry research*, 52(50):18085–18094.

[12] Brower, L. E. and Ferraris, C. F. (2003). Comparison of concrete rheometers. *Concrete International*, 25(8):41–47.

[13] Chen, J., Chu, K., Zou, R., Yu, A., and Vince, A. (2012). Prediction of the performance of dense medium cyclones in coal preparation. *Minerals Engineering*, 31:59–70.

[14] Chen, S.-G., Zhang, C.-H., Jin, F., Cao, P., Sun, Q.-C., and Zhou, C.-J. (2019). Lattice boltzmann-discrete element modeling simulation of scc flowing process for rock-filled concrete. *Materials*, 12(19):3128.

[15] Chidiac, S. and Habibbeigi, F. (2005). Modeling the rheological behaviour of fresh concrete: an elasto-viscoplastic finite element approach. *Computers and Concrete*, 2(2):97–110.

[16] Chidiac, S. and Mahmoodzadeh, F. (2009). Plastic viscosity of fresh concrete–a critical review of predictions methods. *Cement and Concrete Composites*, 31(8):535–544.

[17] Chu, K., Wang, B., Yu, A., and Vince, A. (2009). CFD-DEM modelling of multiphase flow in dense medium cyclones. *Powder Technology*, 193(3):235–247.

[18] Coussot, P., Proust, S., and Ancey, C. (1996). Rheological interpretation of deposits of yield stress fluids. *Journal of Non-Newtonian Fluid Mechanics*, 66(1):55–70.

[19] Cremonesi, M., Ferrara, L., Frangi, A., and Perego, U. (2010). Simulation of the flow of fresh cement suspensions by a lagrangian finite element approach. *Journal of Non-Newtonian Fluid Mechanics*, 165(23-24):1555–1563.

[20] Cui, W., Ji, T., Li, M., and Wu, X. (2017). Simulating the workability of fresh self-compacting concrete with random polyhedron aggregate based on dem. *Materials and Structures*, 50(1):92.

[21] Cundall, P. A. and Strack, O. D. (1979). A discrete numerical model for granular assemblies. *geotechnique*, 29(1):47–65.

[22] de Larrard, F., Hu, C., Sedran, T., Szitkar, J., Joly, M., Claux, F., and Derkx, F. (1997). A new rheometer for soft-to-fluid fresh concrete. *Materials Journal*, 94(3):234–243.

[23] de Larrard, F. and Roussel, N. (2011). Flow simulation of fresh concrete under a slipform machine. *Road Materials and Pavement Design*, 12(3):547–566.

[24] Deb, S. and Tafti, D. K. (2013). A novel two-grid formulation for fluid–particle systems using the discrete element method. *Powder technology*, 246:601–616.

[25] Deeb, R., Karihaloo, B. L., and Kulasegaram, S. (2014a). Reorientation of short steel fibres during the flow of self-compacting concrete mix and determination of the fibre orientation factor. *Cement and Concrete Research*, 56:112–120.

[26] Deeb, R., Kulasegaram, S., and Karihaloo, B. (2014b). 3d modelling of the flow of self-compacting concrete with or without steel fibres. part i: slump flow test. *Computational Particle Mechanics*, 1(4):373–389.

[27] Deeb, R., Kulasegaram, S., and Karihaloo, B. L. (2014c). 3d modelling of the flow of self-compacting concrete with or without steel fibres. part ii: L-box test and the assessment of fibre reorientation during the flow. *Computational Particle Mechanics*, 1(4):391–408.

[28] Dhaheer, M. A., Kulasegaram, S., and Karihaloo, B. (2016). Simulation of self-compacting concrete flow in the j-ring test using smoothed particle hydrodynamics (sph). *Cement and Concrete Research*, 89:27–34.

[29] Di Felice, R. (1994). The voidage function for fluid-particle interaction systems. *International Journal of Multiphase Flow*, 20(1):153–159.

[30] Domone, P. (1998). The slump flow test for high-workability concrete 1. *Cement and Concrete Research*, 28(2):177–182.

[31] Dufour, F. and Pijaudier-Cabot, G. (2005). Numerical modelling of concrete flow: homogeneous approach. *International journal for numerical and analytical methods in geomechanics*, 29(4):395–416.

[32] El Cheikh, K., Rémond, S., Khalil, N., and Aouad, G. (2017). Numerical and experimental studies of aggregate blocking in mortar extrusion. *Construction and Building Materials*, 145:452–463.

[33] Ergun, S. and Orning, A. A. (1949). Fluid flow through randomly packed columns and fluidized beds. *Industrial & Engineering Chemistry*, 41(6):1179–1184.

[34] Esping, O. (2007). Early age properties of self-compacting concrete. *Effects of fine aggregate and limestone filler Ph. D. Sweden: Chalmers University of Technology*.

[35] Farris, R. (1968). Prediction of the viscosity of multimodal suspensions from unimodal viscosity data. *Transactions of the Society of Rheology*, 12(2):281–301.

[36] Ferrara, L., Cremonesi, M., Tregger, N., Frangi, A., and Shah, S. P. (2012). On the identification of rheological properties of cement suspensions: Rheometry, computational fluid dynamics modeling and field test measurements. *Cement and Concrete Research*, 42(8):1134–1146.

[37] Ferraris, C. F. and DeLarrard, F. (1998). Testing and modeling of fresh concrete rheology. Technical report.

[38] Furuichi, M. and Nishiura, D. (2014). Robust coupled fluid-particle simulation scheme in stokes-flow regime: Toward the geodynamic simulation including granular media. *Geochemistry, Geophysics, Geosystems*, 15(7):2865–2882.

[39] Group, T. S.-C. C. E. P. (2005). *The European Guidelines for Self-Compacting Concrete*. BIBM, CEMBUREAU, ERMCO, EFCA, EFNARC.

[40] Hoornahad, H. and Koenders, E. A. (2012). Simulation of the slump test based on the discrete element method (dem). In *Advanced Materials Research*, volume 446, pages 3766–3773. Trans Tech Publ.

[41] Hosseinpoor, M., Khayat, K. H., and Yahia, A. (2017a). Numerical simulation of self-consolidating concrete flow as a heterogeneous material in l-box set-up: coupled effect of reinforcing bars and aggregate content on flow characteristics. *Materials and Structures*, 50(2):1–15.

[42] Hosseinpoor, M., Khayat, K. H., and Yahia, A. (2017b). Numerical simulation of self-consolidating concrete flow as a heterogeneous material in l-box set-up: Effect of rheological parameters on flow performance. *Cement and Concrete Composites*, 83:290–307.

[43] Hu, C., De Larrard, F., and Gjørv, O. E. (1995). Rheological testing and modelling of fresh high performance concrete. *Materials and Structures*, 28(1):1.

[44] Hu, Z., Zhang, Y., and Yang, Z. (2019). Suffusion-induced deformation and microstructural change of granular soils: a coupled CFD-DEM study. *Acta Geotechnica*, 14(3):795–814.

[45] Jing, L., Kwok, C., Leung, Y. F., and Sobral, Y. (2016). Extended cfd–dem for free-surface flow with multi-size granules. *International Journal for Numerical and Analytical Methods in Geomechanics*, 40(1):62–79.

[46] Kafui, D., Johnson, S., Thornton, C., and Seville, J. (2011). Parallelization of a lagrangian–eulerian DEM/CFD code for application to fluidized beds. *Powder Technology*, 207(1-3):270–278.

[47] Kloss, C., Goniva, C., Hager, A., Amberger, S., and Pirker, S. (2012). Models, algorithms and validation for opensource dem and CFD–DEM. *Progress in Computational Fluid Dynamics, an International Journal*, 12(2-3):140–152.

[48] Koch, D. L. and Hill, R. J. (2001). Inertial effects in suspension and porous-media flows. *Annual Review of Fluid Mechanics*, 33(1):619–647.

[49] Koehler, E. P. and Fowler, D. W. (2004). Development of a portable rheometer for fresh portland cement concrete. Technical report.

[50] Kokado, T., Hosoda, T., Miyagawa, T., and Fujii, M. (1997). Study on a method of evaluating a yield value of fresh concrete with a slump flow value. *Doboku Gakkai Ronbunshu*, 1997(578):19–29.

[51] Kuruneru, S. T. W., Marechal, E., Deligant, M., Khelladi, S., Ravelet, F., Saha, S. C., Sauret, E., and Gu, Y. (2019). A comparative study of mixed resolved–unresolved cfd-dem and unresolved cfd-dem methods for the solution of particle-laden liquid flows. *Archives of Computational Methods in Engineering*, 26(4):1239–1254.

[52] Lashkarbolouk, H., Chamani, M. R., Halabian, A. M., and Pishehvar, A. R. (2013). Viscosity evaluation of scc based on flow simulation in the l-box test. *Magazine of concrete research*, 65(6):365–376.

[53] Lashkarbolouk, H., Halabian, A. M., and Chamani, M. R. (2014). Simulation of concrete flow in v-funnel test and the proper range of viscosity and yield stress for scc. *Materials and structures*, 47(10):1729–1743.

[54] Le, H. D., De Schutter, G., Kadri, E.-H., Aggoun, S., Vierendeels, J., Tichko, S., and Troch, P. (2013). Computational fluid dynamics calibration of tattersall mk-ii type rheometer for concrete. *Applied Rheology*, 23(3).

[55] Li, X. and Zhao, J. (2018). A unified cfd-dem approach for modeling of debris flow impacts on flexible barriers. *International Journal for Numerical and Analytical Methods in Geomechanics*, 42(14):1643–1670.

[56] Li, Z. (2015). Rheological model and rheometer of fresh concrete. *Journal of Structural and Construction Engineering, Transaction of Archcitectural Instistue of Japan*, 80(710):527–537.

[57] Link, J., Cuypers, L., Deen, N., and Kuipers, J. (2005). Flow regimes in a spout–fluid bed: A combined experimental and simulation study. *Chemical Engineering Science*, 60(13):3425–3442.

[58] Manninen, M., Taivassalo, V., and Kallio, S. (1996). On the mixture model for multiphase flow.

[59] Mao, J., Zhao, L., Di, Y., Liu, X., and Xu, W. (2020). A resolved cfd–dem approach for the simulation of landslides and impulse waves. *Computer Methods in Applied Mechanics and Engineering*, 359:112750.

[60] Martys, N. and Ferraris, C. F. (2002). Simulation of scc flow. In *Proc. 1st North American Conf. On the Design and Use of Self-Consolidating Concrete, Chicago, IL*, pages 27–30. Citeseer.

[61] Mechtcherine, V. and Shyshko, S. (2007). Virtual concrete laboratory—continuous numerical modelling of concrete from fresh to the hardened state. In *Advances in Construction Materials 2007*, pages 479–488. Springer.

[62] Murata, J. (1984). Flow and deformation of fresh concrete. *Materiaux et Construction*, 17(2):117–129.

[63] Murata, J. and Kukawa, H. (1992). Viscosity equation for fresh concrete. *Materials Journal*, 89(3):230–237.

[64] Neophytou, M. K., Pourgouri, S., Kanellopoulos, A. D., Petrou, M. F., Ioannou, I., Georgiou, G., and Alexandrou, A. (2010). Determination of the rheological parameters of self-compacting concrete matrix using slump flow test. *Applied Rheology*, 20:62402.

[65] Nguyen, V., Rémond, S., Gallias, J., Bigas, J., and Muller, P. (2006). Flow of herschel–bulkley fluids through the marsh cone. *Journal of non-newtonian fluid mechanics*, 139(1-2):128–134.

[66] Odar, F. and Hamilton, W. S. (1964). Forces on a sphere accelerating in a viscous fluid. *Journal of fluid Mechanics*, 18(2):302–314.

[67] Peng, Z., Doroodchi, E., Luo, C., and Moghtaderi, B. (2014). Influence of void fraction calculation on fidelity of cfd-dem simulation of gas-solid bubbling fluidized beds. *AIChE Journal*, 60(6):2000–2018.

[68] Pitt, M. et al. (2000). The marsh funnel and drilling fluid viscosity: a new equation for field use. *SPE Drilling & Completion*, 15(01):3–6.

[69] Pozzetti, G. and Peters, B. (2018). A multiscale dem-vof method for the simulation of three-phase flows. *International Journal of Multiphase Flow*, 99:186–204.

[70] Puri, U. and Uomoto, T. (1999). Numerical modeling—a new tool for understanding shotcrete. *Materials and Structures*, 32(4):266–272.

[71] Puri, U. and Uomoto, T. (2002). Characterization of distinct element modeling parameters for fresh concrete and its application in shotcrete simulations. *Journal of materials in civil engineering*, 14(2):137–144.

[72] Qiu, L. (2014). Three dimensional gpu-based sph modelling of self-compacting concrete flows. In *Proceedings of the third international symposium on Design, Performance and Use of Self-Consolidating Concrete*, pages 151–155.

[73] Reeks, M. and McKee, S. (1984). The dispersive effects of basset history forces on particle motion in a turbulent flow. *The Physics of fluids*, 27(7):1573–1582.

[74] Remond, S. and Pizette, P. (2014). A dem hard-core soft-shell model for the simulation of concrete flow. *Cement and concrete research*, 58:169–178.

[75] Roussel, N. and Coussot, P. (2005). "fifty-cent rheometer" for yield stress measurements: from slump to spreading flow. *Journal of rheology*, 49(3):705–718.

[76] Roussel, N. and Le Roy, R. (2005). The marsh cone: a test or a rheological apparatus? *Cement and Concrete Research*, 35(5):823–830.

[77] Roussel, N., Stefani, C., and Leroy, R. (2005). From mini-cone test to abrams cone test: measurement of cement-based materials yield stress using slump tests. *Cement and Concrete Research*, 35(5):817–822.

[78] Rubinow, S. I. and Keller, J. B. (1961). The transverse force on a spinning sphere moving in a viscous fluid. *Journal of Fluid Mechanics*, 11(3):447–459.

[79] Saffman, P. (1965). The lift on a small sphere in a slow shear flow. *Journal of fluid mechanics*, 22(2):385–400.

[80] Shepherd, G., Terradellas, E., Baklanov, A., Kang, U., Sprigg, W., Nickovic, S., Boloorani, A. D., Al-Dousari, A., Basart, S., Benedetti, A., et al. (2016). Global assessment of sand and dust storms.

[81] Shimura, K. and Matsuo, A. (2019). Using an extended CFD-DEM for the two-dimensional simulation of shock-induced layered coal-dust combustion in a narrow channel. *Proceedings of the Combustion Institute*, 37(3):3677–3684.

[82] Shyshko, S. and Mechtcherine, V. (2010). Simulating fresh concrete behaviour–establishing a link between the bingham model and parameters of a dem-based numerical model. *HetMat–Modelling of Heteroginous Materials. RILEM Proceedings PRO*, 76:211–219.

[83] Sun, R. and Xiao, H. (2015). Diffusion-based coarse graining in hybrid continuum–discrete solvers: theoretical formulation and a priori tests. *International Journal of Multiphase Flow*, 77:142–157.

[84] Sun, X. and Sakai, M. (2015). Three-dimensional simulation of gas–solid–liquid flows using the dem–vof method. *Chemical Engineering Science*, 134:531–548.

[85] Tattersall, G. H. (2014). *Workability and quality control of concrete*. CRC Press.

[86] Thanh, H. T., Li, J., and Zhang, Y. (2019). Numerical modelling of the flow of self-consolidating engineered cementitious composites using smoothed particle hydrodynamics. *Construction and Building Materials*, 211:109–119.

[87] the joint EFFC/DFI Concrete Task Group (2018). Guide to tremie concrete for deep foundations. Technical report, The joint EFFC/DFI Concrete Task Group.

[88] Thrane, L. N., Szabo, P., Geiker, M., Glavind, M., and Stang, H. (2004). Simulation of the test method "l-box" for self-compacting concrete. *Annual Transactions of the NORDIC rheology society*, 12(1):47–54.

[89] Tichko, S., Van De Maele, J., Vanmassenhove, N., De Schutter, G., Vierendeels, J., Verhoeven, R., and Troch, P. (2010). Numerical modelling of the filling of formworks with self-compacting concrete. *Advances in Fluid Mechanics*, 8:157.

[90] Tregger, N., Ferrara, L., and Shah, S. P. (2008). Identifying viscosity of cement paste from mini-slump-flow test. *ACI Materials Journal*, 105(6):558.

[91] Tsuji, Y., Kawaguchi, T., and Tanaka, T. (1993). Discrete particle simulation of two-dimensional fluidized bed. *Powder technology*, 77(1):79–87.

[92] Ubbink, O. (1997). Numerical prediction of two fluid systems with sharp interfaces.

[93] Van Wachem, B., Van der Schaaf, J., Schouten, J., Krishna, R., and Van den Bleek, C. (2001). Experimental validation of lagrangian–eulerian simulations of fluidized beds. *Powder Technology*, 116(2-3):155–165.

[94] Varga, M., Goniva, C., Adam, K., and Badisch, E. (2013). Combined experimental and numerical approach for wear prediction in feed pipes. *Tribology International*, 65:200–206.

[95] Vasilic, K., Meng, B., Kühne, H.-C., and Roussel, N. (2011). Flow of fresh concrete through steel bars: A porous medium analogy. *Cement and Concrete Research*, 41(5):496–503.

[96] Wachs, A. (2007). Numerical simulation of steady bingham flow through an eccentric annular cross-section by distributed lagrange multiplier/fictitious domain and augmented lagrangian methods. *Journal of non-newtonian fluid mechanics*, 142(1-3):183–198.

[97] Wang, C. and Cheng, P. (1996). A multiphase mixture model for multiphase, multicomponent transport in capillary porous media—i. model development. *International journal of heat and mass transfer*, 39(17):3607–3618.

[98] Wang, Z., Teng, Y., and Liu, M. (2019). A semi-resolved cfd–dem approach for particulate flows with kernel based approximation and hilbert curve based searching strategy. *Journal of Computational Physics*, 384:151–169.

[99] Wen, C. Y. (1966). Mechanics of fluidization. In *Chem. Eng. Prog., Symp. Ser.*, volume 62, pages 100–111.

[100] Wu, C., Zhan, J., Li, Y. S., Lam, K. S., and Berrouk, A. (2009). Accurate void fraction calculation for three-dimensional discrete particle model on unstructured mesh. *Chemical Engineering Science*, 64(6):1260–1266.

[101] Wu, L., Gong, M., and Wang, J. (2018). Development of a dem–vof model for the turbulent free-surface flows with particles and its application to stirred mixing system. *Industrial & Engineering Chemistry Research*, 57(5):1714–1725.

[102] Wu, W., Huang, X., Yuan, H., Xu, F., and Ma, J. (2017). A modified lattice boltzmann method for herschel-bulkley fluids. *Rheologica Acta*, 56(4):369–376.

[103] Xu, Z. and Li, Z. (2021). Numerical method for predicting flow and segregation behaviors of fresh concrete. *Cement and Concrete Composites*, 123:104150.

[104] Zeng, J., Li, H., and Zhang, D. (2016). Numerical simulation of proppant transport in hydraulic fracture with the upscaling CFD-DEM method. *Journal of Natural Gas Science and Engineering*, 33:264–277.

[105] Zhan, Y., Gong, J., Huang, Y., Shi, C., Zuo, Z., and Chen, Y. (2019). Numerical study on concrete pumping behavior via local flow simulation with discrete element method. *Materials*, 12(9):1415.

[106] Zhang, G., Gutierrez, M., and Li, M. (2017). Numerical simulation of transport and placement of multi-sized proppants in a hydraulic fracture in vertical wells. *Granular Matter*, 19(2):32.

[107] Zhao, J. and Shan, T. (2013). Coupled cfd–dem simulation of fluid–particle interaction in geomechanics. *Powder technology*, 239:248–258.

[108] Zhou, Z., Kuang, S., Chu, K., and Yu, A. (2010). Discrete particle simulation of particle–fluid flow: model formulations and their applicability. *Journal of Fluid Mechanics*, 661:482–510.

[109] Zhu, H. and Yu, A. (2002). Averaging method of granular materials. *Physical Review E*, 66(2):021302.